

FLORIDA STATE UNIVERSITY
COLLEGE OF ARTS AND SCIENCES

NUCLEAR STRUCTURE STUDIES OF ^{44}S AND ^{26}Si

By

JOHN J. PARKER IV

A Dissertation submitted to the
Department of Physics
in partial fulfillment of the
requirements for the degree of
Doctor of Philosophy

2017

Copyright © 2017 John J. Parker IV. All Rights Reserved.

ProQuest Number: 10262105

All rights reserved

INFORMATION TO ALL USERS

The quality of this reproduction is dependent upon the quality of the copy submitted.

In the unlikely event that the author did not send a complete manuscript and there are missing pages, these will be noted. Also, if material had to be removed, a note will indicate the deletion.



ProQuest 10262105

Published by ProQuest LLC (2017). Copyright of the Dissertation is held by the Author.

All rights reserved.

This work is protected against unauthorized copying under Title 17, United States Code
Microform Edition © ProQuest LLC.

ProQuest LLC.
789 East Eisenhower Parkway
P.O. Box 1346
Ann Arbor, MI 48106 – 1346

John J. Parker IV defended this dissertation on April 5, 2017.
The members of the supervisory committee were:

Ingo Wiedenhöver
Professor Directing Dissertation

Henry Fuelberg
University Representative

David Collins
Committee Member

Sam Tabor
Committee Member

Alexander Volya
Committee Member

The Graduate School has verified and approved the above-named committee members, and certifies that the dissertation has been approved in accordance with university requirements.

ACKNOWLEDGMENTS

There are many people I have to thank for supporting me over the course of my PhD work. First and foremost, I have to thank Dr. Ingo Wiedenhöver for always being available for help and guidance. I couldn't imagine a better advisor. I would also like to thank everyone in the γ gang, in particular Dr. Sam Tabor, Dr. Vandana Tripathi, and Dr. Dave Caussyn for always providing help and advice for the work done in the γ cave. Thanks to Dr. Volya and Kostas Kravvaris for patiently explaining different theoretical aspects. Thanks to all of the NRB staff, especially Dr. Lagy Baby, for all of their help in running experiments. Thanks to the staff at the NSCL for helping with the successful GRETINA experiment and to Dr. Hiro Iwasaki for many useful discussions. I would also like to thank Dr. Volya, Dr. Tabor, Dr. Collins, and Dr. Fuelberg for serving on my committee.

My graduate experience would not have been the same without all of my fellow graduate students who have helped me along the way and become my friends. Special thanks to Justin VonMoss for helping me in the γ cave when I first joined the group and to Daniel Santiago-Gonzalez for helping me with programming and data analysis using ROOT. Special thanks to Rutger Dungan, Jeff Klatsky, and Anthony Kuchera for all of the Panda Wednesday lunches we had during the course of our graduate careers.

I am also very thankful for the love and support I have received from my family throughout the years. Mom, Dad, Jenny, and Beth thank you for always being there for me. Thanks to my girlfriend, Maddie, for your love and encouragement over the last few years. I would not be here without the support I received from you all.

TABLE OF CONTENTS

List of Tables	vi
List of Figures	vii
Abstract	xiii
1 Introduction	1
2 Isomeric Character of the 4_1^+ State in ^{44}S	3
2.1 Introduction	3
2.1.1 Narrowing of the N=28 Shell Gap	3
2.1.2 Previous Studies on ^{44}S	4
2.2 Experimental Details	6
2.2.1 Particle Identification with the S800 Spectrometer	6
2.2.2 Gamma Ray Detection with GRETINA	8
2.2.3 Lifetime Measurements using DSAM or RDM	12
2.3 Analysis of “Target-Only” Data	14
2.3.1 Particle Identification of Reaction Residues	14
2.3.2 Gamma Ray Detection with GRETINA	15
2.4 Analysis of the RDM Data	22
2.4.1 Select Target-Induced Reactions with the S800	22
2.4.2 Establishing the Lifetime of the 4_1^+ State	25
2.5 Using the Geant4 Simulation to Determine the Lifetime	27
2.5.1 Comparing Simulation to the Data with χ^2 Test	27
2.5.2 Setting Up the Simulation Parameters	28
2.5.3 Setting up the Parameters of the Level Scheme	31
2.5.4 Long-Distance Runs	36
2.5.5 Determining the Lifetime with the Short-Distance Runs	43
2.5.6 Establishing the Methodology with ^{42}S	44
2.6 Discussion	46
2.6.1 The Shell Model	46
2.6.2 Rotational Motion	50
2.6.3 Theoretical Works	51
3 Establishing Resonances in $^{25}\text{Al}(p,\gamma)^{26}\text{Si}$ via the ($^3\text{He},n$) Reaction	55
3.1 Introduction	55
3.1.1 ^{26}Al in the Galaxy	55
3.1.2 Nuclear Physics Effects Influencing the Reaction Rate for $^{25}\text{Al}(p,\gamma)^{26}\text{Si}$	57
3.1.3 Previous Works	58
3.2 Experimental Techniques	61
3.2.1 The FSU Compton-Suppressed γ Array	61
3.2.2 The Neutron Wall and Electronics	63
3.2.3 Reaction Kinematics	65

3.3	Analysis	68
3.3.1	Calibration of the Neutron Time of Flight	68
3.3.2	Energy and Efficiency Calibration of the γ Rays	72
3.3.3	Doppler Shift of γ Rays	73
3.4	Results	78
3.4.1	Establishing the Level Scheme	79
3.5	Discussion	79
3.5.1	Determining Reaction Rate	85
3.5.2	Impact of Uncertainties on $^{25}\text{Al}(p,\gamma)$ Reaction Rate	87
3.5.3	Impact on Stellar Abundance of ^{26}Al	87
 Appendix		
A TOF Correction for the S800 Spectrometer		90
Bibliography		92
Biographical Sketch		98

LIST OF TABLES

2.1	Centroids for States input into Simulation. The lifetime, τ , is varied only for the 4_1^+ state. Consequently, the input centroid for the 4_1^+ and the 2_1^+ states depends on the lifetime because long-lived states decay downstream of where they are produced, creating a difference in the angle for the Doppler-correction.	33
2.2	Intensities measured by using the data and by using the simulation. As can be seen, these two methods agree well with one another.	35
3.1	List of levels in ^{26}Si in the Gamow window. The 1^+ , 0^+ , and 3^+ are positively identified, while the existence and impact of a 4^{th} resonance is questionable. (see text)	61
3.2	List of observed γ rays. Ref [1] comes from a fusion evaporation experiment and Ref [2] comes from a recent $(3\text{He},n)$. Both experiments were performed using Gammasphere.	82
3.3	Parameters used in determining the $^{25}\text{Al}(p,\gamma)^{26}\text{Si}$ reaction rate.	85

LIST OF FIGURES

2.1	Showing the 2^+ Systematics for Nuclei in the N=28 Region [3]. Notice that the N=28 shell gap appears intact at ^{48}Ca , but shows significant weakening for ^{44}S	4
2.2	The level scheme for ^{44}S observed by Santiago-Gonzalez et al.[4]. Shell model calculations suggest that the observed 4^+ is not apart of the ground state band and is a hindered transition.	5
2.3	A schematic of the S800 focal plane box [5]. See text for details.	7
2.4	Manner in which γ rays are most likely to interact with matter as a function of energy [6]. The Compton effect dominates at energies relevant to our nuclear structure studies.	9
2.5	The Recoil Distance Method [7]. A degrader is placed downstream of the target location to slow the recoiling particles by about 10%. For each γ ray transition, two peaks will be observed. One peak corresponds to decays that occur before the degrader and the other peak corresponds to decays that happen after the degrader. The lifetime of the state can be extracted by moving the location of the degrader, which will shift the relative intensities of the two peaks.	13
2.6	The particle identification with the S800. Panel a shows the energy loss versus time of flight. Panel b separates the recoils based on the focal plane position.	15
2.7	The relative efficiency of GRETINA as a function of energy. Note that this efficiency calibration is done relative to the area of the 121 keV peak in ^{152}Eu	16
2.8	The γ ray detection angle vs. the γ ray energy. The energy of the γ ray is independent of detection angle, showing that the Doppler correction is performing well.	17
2.9	The γ ray spectra for the GRETINA data set with a full Doppler correction (recoil direction and velocity taken into account) and a fixed Doppler Correction (beam direction and fixed velocity).	18
2.10	The adopted level scheme for ^{44}S . The main transitions establishing the 2_1^+ , 2_3^+ , and 4_1^+ excited states observed by Santiago-Gonzalez et al.[4] were confirmed.	19
2.11	The γ ray singles spectra as well as all γ rays in coincidence with the $2_1^+ \rightarrow 0_1^+$ transition. The coincident spectrum is scaled by a factor of 15.	21
2.12	The γ ray singles spectra as well as all γ rays in coincidence with the $2_3^+ \rightarrow 2_1^+$ transition (green) and all γ rays in coincidence with the $2_4^+ \rightarrow 2_3^+$ transition (red). The coincident spectra are scaled by a factor of 15.	21

2.13	The γ ray singles spectra as well as all γ rays in coincidence with the $4_1^+ \rightarrow 2_1^+$ transition. The coincident spectrum is scaled by a factor of 15.	22
2.14	Schematic diagram showing energy loss in target and degrader. A reaction that occurs in the degrader (Path 1) will result in a lower energy reaction than a reaction that occurs in the target (Path 2).	23
2.15	The effect discussed in Figure 2.14 is clearly seen in the long distance data. The momentum spread is plotted against γ ray energy for γ rays in coincidence with ^{44}S recoils at the long (25mm) target-degrader distance. The degrader-induced reactions (labeled d) are clearly shifted along the DTA axis with respect to the target-induced reactions (labeled t).	24
2.16	γ ray spectra observed in coincidence with ^{44}S , recorded with the target-degrader distance set to 3mm (Panel a), set to 6mm (Panel b), and set to 25mm (Panel c). For most γ transitions, two peaks are observed. For the 3mm and 6mm runs, these are labeled as “s” for slow transitions that decay past the degrader, and “f” for fast transitions that decay before the degrader. For the 25mm run, these transitions are labeled “t” for target-induced reactions and “d” for degrader-induced reactions. Notice that in the peaks corresponding to the $4_1^+ \rightarrow 2_1^+$ transition (1140 keV), most of the intensity is found in the “slow” peak for the 3mm and 6mm distance, while the intensity shifts to the “fast” peak at 25mm. This shift in intensity is indicative of a lifetime effect. In contrast, the peak corresponding to the $2_3^+ \rightarrow 2_1^+$ transition (949 keV) has all of its intensity in the ‘fast’ peak at 3mm and 6mm, indicative of a very fast transition. This lifetime is quantified in section 2.4.	26
2.17	The simulated velocity in comparison to the measured velocity for scattered ^{46}Ar beam before the target (Panel a), after the target (Panel b), and after the degrader (Panel c).	29
2.18	Comparing the simulated to measured DTA for the target-only run (Panel a) and for the long distance run (Panel b). The simulated DTA spectra is calculated from the final momentum of the reaction residues leaving the degrader, while the DTA from the data is measured in the S800.	30
2.19	The angle of the reaction residues (ATA) plotted against the momentum of the reaction residues (DTA) for residues detected in the 25mm data run. The S800 acceptance depends both on the momentum and on the angle of the residues leaving the target. A cut was applied to the simulated events to match this energy-angle relationship.	31
2.20	Comparing the efficiency of the simulated source run to the actual source run for both add back turned on and off.	32
2.21	Determining the intensity of the 2_1^+ , 2_3^+ , and 4_1^+ using the simulation. In Panel a, the intensity of the 2_1^+ state is fixed while the ratio of the intensities of the 2_3^+ to 4_1^+ is allowed to vary. In Panel b, the ratio of the intensities of the 2_3^+ to 4_1^+ is fixed and the intensity of the 2_1^+ is allowed to vary.	34

2.22	Comparing data to simulation for the adopted lifetime of the 4^+ and for a short lifetime. The target-only spectra is not very sensitive to the lifetime effect.	35
2.23	χ^2 dependence on τ . The lifetime of the 4_1^+ state is allowed to vary, while the lifetimes of the 2_1^+ and the 2_3^+ states are fixed. The $4_1^+ \rightarrow 2_1^+$ transition and the $2_1^+ \rightarrow 0_1^+$ transition both have better fits for long lifetimes, while the $2_3^+ \rightarrow 2_1^+$ transition shows no lifetime dependence. However, the target-only spectra is not very sensitive to the lifetime.	36
2.24	Demonstration of different intensities on degrader-induced reactions versus target-induced reactions. Panel a shows simulated spectra with different input degrader intensities and Panel b shows the measured ratio as a function of expected ratio. . .	38
2.25	γ ray spectrum recorded for the target-degrader distance 25 mm, in coincidence with ^{44}S reaction residues (Panel a). For each γ transition, two peaks are observed, one for target-induced reactions (labeled “t”), and one for degrader-induced reactions (labeled “d”). The simulated spectra were used to determine the ratio of reactions induced by the degrader. The χ^2 dependence on target-to-degrader reaction ratio is shown in Panel b.	40
2.26	Scaling from full S800 acceptance to half S800 acceptance (see text).	41
2.27	γ ray spectra observed in coincidence with ^{44}S , recorded with the target-degrader distance set to 3mm (Panel a) and set to 6mm (Panel b). The spectra are compared to a Monte-Carlo simulation for the adopted lifetime of the 4^+ state (76ps) and, for comparison and vertical offset, a short lifetime of 3.5ps. The 949 keV peak shows characteristics of a prompt emission, while the 1140 keV peak shows characteristics of a long lifetime. The spectra were fit using a Monte-Carlo simulation (see text). The χ^2 dependence on lifetime is shown in Panel c.	42
2.28	γ ray spectra observed in coincidence with ^{44}S , recorded with the target-degrader distance set to 3mm (Panel a) and set to 6mm (Panel b). Here the assumed 4_1^+ ratio was 0.8 causing the determined simulated lifetime to be shorter. A systematic error of $\pm 20\text{ps}$ was adopted.	45
2.29	γ ray spectrum recorded for the target-degrader distance 25 mm, in coincidence with ^{42}S reaction residues (Panel a). For each γ -transition, two peaks are observed, one for target-induced reactions (labeled “t”), and one for degrader-induced reactions (labeled “d”). The simulated spectra were used to determine the ratio of reactions induced by the degrader. The χ^2 dependence on target-to-degrader reaction ratio is shown in Panel b.	47
2.30	γ ray spectra observed in coincidence with ^{42}S , recorded with the target-degrader distance set to 3 mm (Panel a) and set to 6 mm (Panel b). The relative change in intensities in the fast and slow peaks from 3 mm to 6 mm is an effect of the state’s lifetime. The spectra were fit using a Monte-Carlo simulation (see text). The χ^2 dependence on lifetime is shown in Panel c.	48

2.31	The ordering of nuclear levels for ^{44}S . The levels are filled in with the protons and neutrons. The neutrons completely fill the $f_{7/2}$ level. Figure taken from the dissertation by Daniel Santiago-Gonzalez[8].	49
2.32	Rotational motion can be separated into rotations about a space fixed axis and rotations about a body fixed axis. The projection of the angular momentum onto the body fixed axis is referred to as K and is conserved for axially symmetric nuclei[9] . . .	51
3.1	Spatial Distribution of ^{26}Al [10]. Due to this observed spatial distribution, most of the ^{26}Al is believed to be produced in Wolf-Rayet stars and the supernova that result from their death [10]. However, it is thought that nova could be a secondary source for ^{26}Al , contributing up to $0.4M_{\odot}$ [11].	56
3.2	^{26}Al can be produced in the ground state, which β decays to ^{26}Mg with a half-life of 700,000 years, emitting a 1.809 MeV γ ray. Additionally, ^{26}Al can be produced in the isomeric 0^+ state which β decays to the ground state of ^{26}Mg in 6s. The branching of the two pathways that produce these states must be understood in order to understand the observed distribution of ^{26}Al in the galaxy.	57
3.3	The location of the resonances inside the Gamow window. Three resonances seem to be firmly established, while a 4^{th} resonance is less certain.	58
3.4	A schematic of a Compton-suppressed clover detector. The different paths are discussed in the text.	62
3.5	A schematic of the electronic set up used in this experiment. The TACs are used to measure the tof between the neutron wall signal and the RF-reference of the linac. All of the 'up' signals go to one TAC and all of the 'down' signals go to a second TAC. The information about which neutron bar fired is recovered by sending all 24 neutron output signals from the CFD into the Pixie-16 system. Note that only 4 of the 12 neutron bars are shown.	64
3.6	Schematic of the reaction and the detectors. The neutron energy and angle, α , are measured such that the energy and angle, δ , of the undetected ^{26}Si can be reconstructed.	65
3.7	Dependence of neutron energy on angle for population of ground state and an excited state. This experiment only covers an angular range of about 30° , so this kinematic correction does not make a large difference.	67
3.8	Panel a shows the raw tac signals coming from the top of the bars and the bottom of the bars. Panel b shows how averaging the up and the down signals greatly improves the timing resolution. The two prominent peaks seen in the spectra come from the prompt γ rays and are referred to as the γ -flash. To the left of each of the large peaks, there are regions of flight times which indicate the arrival of the neutrons.	69

3.9	The two γ flashes arrive 82ns apart and can be used to calibrate the tof, shown in Panel a. There are two identical structures of γ rays followed by neutrons that can be lined up with one another (Panel b).	70
3.10	The tof spectra zoomed in on the neutrons. Panel a shows the calibrated tof and panel b shows the TOF with path length corrections applied. The path length corrections work by realizing that neutrons of the same energy will have different flight times for different path lengths, but they will have the same velocity. Panel b is essentially the velocity of the neutrons parameterized as a tof.	71
3.11	The reconstructed Q-value. The data in both panels is the same, but Panel b uses a variable bin width while panel a uses a fixed bin width.	71
3.12	The neutron tof spectrum (Panel a) and reconstructed excitation energy (Panel b) in coincidence with γ rays coming from the $0_4^+ \rightarrow 2_2^+$ transition. These peaks have a full width half max of 3.3 ns and 400 keV, respectively.	72
3.13	The relative efficiency of the γ array as a function of energy. Note that this efficiency calibration is done relative to the area of the 121 keV peak in ^{152}Eu	73
3.14	Determination of angle for crystals within a clover detector with respect to the beam axis. Panel a assumes that the red and blue crystals are located at 90° . Panel b assumes that the red crystal is at 96° and the blue crystal is at 84° . This correction is important in maximizing the resolution for very fast transitions such as the 1400 keV γ ray shown in the spectra. However, the Doppler correction hurts the resolution for states that decay after the ^{26}Si recoil has come to a complete stop, such as for the 1538 keV γ ray.	75
3.15	Reconstructed angle between recoiling ^{26}Si and detector as a function of neutron time of flight (Panel a). The phi angle was not measured for each HPGe, so Panel b shows the small effect that changing the assumed phi for a given crystal by a small amount has on the γ ray spectra.	76
3.16	The effect of the Doppler correction shown for the γ -array at FSU. The fixed Doppler correction assumes that the recoiling particle is moving along the beam direction with a constant velocity. The full Doppler correction uses the reconstructed recoil direction and velocity.	77
3.17	The corrected tof (Panel a) and the reconstructed Q-value (Panel b).	78
3.18	The excitation energy plotted against the γ ray energy. The dashed line indicates the proton threshold. The excitation energy provides direct information about which level was occupied in ^{26}Si , while the γ ray energy allows for an indirect but precise determination of the level energy.	80
3.19	The adopted level scheme for ^{26}Si . Newly observed transitions are shown in blue and transitions that were unobserved in this work are shown in red.	81

3.20	γ rays in coincidence with neutrons depopulating states of around 5.9 MeV. Two new transitions were observed depopulating the 0_4^+ state, shown in blue. The arrows indicate single-escape peaks.	81
3.21	γ rays in coincidence with neutrons depopulating states of around 4.8 MeV. Five new transitions are identified in this figure, shown in blue.	83
3.22	γ rays in coincidence with neutrons depopulating states above 5 MeV. Two previously unobserved ground state transitions were observed depopulating the 2_5^+ and the 1_1^+ levels.	83
3.23	The contribution to the total reaction rate from the individual resonances in the Gamow Window.	86
3.24	The percent that the 0^+ rate contributes to the total reaction rate. Using the newer value of 5.888 MeV increases the contribution of the 0^+ state at nova temperatures.	88
3.25	Impact of uncertainty in Γ_γ of the 3^+ state on the total reaction rate. The uncertainties in Γ_γ are taken from the recent publication by Bennett et al[12].	89
A.1	The particle identification shown before (Panel a) and after (Panel b) a timing correction was done.	90
A.2	The timing of the plastic scintillator as a function of its energy before (Panel a) and after (Panel b) the timing was corrected for.	91

ABSTRACT

Experimental results on the nuclear structure of ^{44}S and ^{26}Si will be reported in this thesis. ^{44}S is studied because of its interest in understanding how nuclei behave far from stability. ^{26}Si is studied because of the impact of understanding its nuclear structure can have on the astrophysical $^{25}\text{Al}(p,\gamma)$ reaction rate. These are two very differently motivated studies and will be described separately in Chapters 2 and 3, respectively.

Chapter 2 focuses on the exotic $N=28$ nucleus, ^{44}S . Previous experiments observed a 4^+ state in ^{44}S and suggested that this state may exhibit a hindered E2-decay rate, inconsistent with being a member of the collective ground state band. We populate this state via a two-proton knockout reaction from a beam of exotic ^{46}Ar projectiles delivered from the coupled cyclotron facility and measure its lifetime using the recoil distance method with the GRETINA γ ray spectrometer. The result, $76(14)_{stat}(20)_{syst}$ ps, implies a hindered transition of $B(E2; 4^+ \rightarrow 2_1^+) = 0.61(19)$ single-particle or Weisskopf units strength and supports the interpretation of the 4^+ state as a $K = 4$ isomer, the first example of a high- K isomer in a nucleus of such low mass.

Chapter 3 focuses on resonances above the proton threshold in ^{26}Si . Previous experiments have solidified the placement of 3 resonances thought to contribute to the $^{25}\text{Al}(p,\gamma)^{26}\text{Si}$ reaction. A fourth resonance has been suggested by various experiments, but more recent experiments have suggested that this level has been misidentified. We populate excited states in ^{26}Si via the $^{24}\text{Mg}(^3\text{He},n)$ reaction at 10 MeV at the John Fox Lab at FSU. Neutron time-of-flight spectroscopy is used to identify which resonance is populated in ^{26}Si and the γ -array at FSU is used to determine how these levels de-excite. The γ ray sensitivity in this experiment is the highest sensitivity reached to date, but a 4^{th} resonance above the proton threshold was not identified, giving further indication that this state may have been misidentified by past experiments.

CHAPTER 1

INTRODUCTION

Nuclear structure studies today seek to expand our knowledge of how protons and neutrons arrange themselves inside the nucleus of an atom. The shell model provides the best description which says that, similar to how electrons fill atomic orbitals in atoms, neutrons and protons fill shells inside the nucleus of an atom. The first three shell closures at $N=2$, 8 , and 20 can be formed by a central potential with no reference to the intrinsic spin of the nucleons. All shells above $N=20$ ($N=28$, 50 , 82 , and 126) need a term that couples the intrinsic spin of the nucleons to the orbital angular momentum. The addition of this spin-orbit term to the nuclear potential by Maria Goeppert-Mayer[13] and separately by Haxel, Jensen, and Suess[14] in 1949 was an incredible achievement that garnered the 1963 Nobel Prize in physics for Goeppert-Mayer and Jensen.

Recently, experimental work has been done to extend the reach of experimental nuclear physics to nuclei far from stability. Radioactive ion beam facilities, such as RESOLUT at FSU, are used to study isotopes off of the line of β stability. At the National Superconducting Cyclotron Laboratory (NSCL), rare isotope beams are created by fragmentation and in-flight separation of isotopes. The future of this line of research is the facility for rare isotope beams (FRIB), which is currently being developed at the NSCL. FRIB is expected to be able to reach 80% of all expected isotopes below uranium[15].

Going hand-in-hand with radioactive beam development, is the development of detectors to perform sensitive studies on these nuclei. The most detailed spectroscopic studies make use of high-purity germanium (HPGe) detectors. HPGe detectors give the best intrinsic energy resolution for studying γ ray transitions. For the spectroscopy of fast nuclei traveling at a significant percentage of the speed of light, Doppler corrections become important for reconstructing nuclear excitations with high resolution. These Doppler corrections, in turn, depend on the ability to precisely determine the interaction point of the γ ray with the detector. In an effort to optimize nuclear structure research on exotic nuclei, the γ ray energy tracking array (GRETA) is being developed. This array will consist of highly-segmented HPGe crystals that retain the superior intrinsic energy resolution

of HPGe detectors and add a position resolution of 2mm in three dimensions. This experiment represents one of the first studies with GRETINA, which was built as a quarter of GRETA and used to develop the experimental methods needed for it. Even as such, GRETINA already constitutes the most powerful γ ray spectrometer for exotic nuclei.

These advances in beam and detector development are being used to advance our understanding of nuclear structure across the chart of the nuclides. Recently, a tremendous amount of research has been done to explore how these shell closures behave in nuclei far from the equilibrium that protons and neutrons have. Chapter 2 of this work focuses on an experiment performed at the NSCL using GRETINA and recently reported in Physical Review Letters [16]. This work focuses on the N=28 nucleus, ^{44}S , and reports the existence of a low-lying 4^+ state that can be characterized as a high-K isomer. High-K isomers are well known in heavy nuclei far away from closed shells, so the observation of a high-K isomer this low in the chart of the nuclides is quite interesting.

The details of how neutrons and protons arrange themselves may seem of general interest only in the investigation of the nuclear many body problem. However, understanding nuclear structure allows us to answer fundamental questions about the universe such as where do the chemical elements come from. For instance, the observed abundance of ^{12}C is explained by a resonance in ^{12}C at about 7.7 MeV[17]. If this resonance did not exist, the triple-alpha reaction that bypasses mass 8 would be much too slow and there would not be enough ^{12}C for life as we know it to occur. In fact, the synthesis of elements all across the nuclear landscape depends critically on the resonances in nuclei and the shell structure. In Chapter 3 of this work, we examine the case of ^{26}Al . ^{26}Al is a useful barometer for nucleosynthesis in stars because it beta decays after 700,000 years and emits a 1.8 MeV γ ray. This 1.8 MeV γ ray has been detected from sources throughout the galaxy, which indicates that nucleosynthesis is on-going. Understanding the observed abundance of ^{26}Al comes down to understanding the reactions that lead to its production. The most critical of these is the $^{25}\text{Al}(p,\gamma)^{26}\text{Si}$ reaction. In chapter 3, we study this reaction by populating the resonances in ^{26}Si to indirectly determine the reaction rate.

CHAPTER 2

ISOMERIC CHARACTER OF THE 4_1^+ STATE IN ^{44}S

2.1 Introduction

This chapter is focused on the N=28 isotones, in particular the nuclide ^{44}S . Previous experiments [18] have found that the conventional closed shell configuration, naively expected for an N=28 isotone, has broken down by ^{44}S , as ^{44}S exhibits a low-lying 2^+ state and a relatively fast collective E2 γ transition. In addition, the work by Grevy et al.[19] and Force et al.[20] identified a low-lying isomeric 0^+ state that suggested shape-coexistence in ^{44}S . More recently, the work by Santiago-Gonzalez et al.[4] identified a low lying 4^+ state that shell model calculations suggest is not part of the rotational band. This current work seeks to quantify the nature of the 4^+ state observed by Santiago-Gonzalez et al.[4] by measuring the lifetime of the state.

The rest of this introduction will discuss the N=28 isotones in general and will discuss the previous experimental works on ^{44}S in detail. Section 2.2 will discuss the experimental techniques used in this work, with particular attention paid to the method of measuring the lifetime of the 4^+ state, namely the recoil distance method. In sections 2.3 and 2.4, we will discuss the data and establish the level scheme and qualitatively establish the lifetime of the 4^+ state by discussing the spectra obtained in the recoil distance method data. In section 2.5, we will quantify the lifetime of the 4^+ state by using a Geant4 based Monte-Carlo simulation. Finally, in section 2.6, we will discuss the results in light of recent theoretical works based on shell model calculations and based on beyond-mean-field calculations.

2.1.1 Narrowing of the N=28 Shell Gap

The N=28 isotone furthest from stability and experimentally observed is ^{40}Mg . However, the N=28 shell shows signs of breaking before this limit is reached. In Figure 2.1, the systematics of 2^+ state energies and reduced transition probability ($B(E2)$), values for the isotopes near N=28 are shown [3]. In the Calcium isotopic chain, a large increase in the 2^+ energy is evident at neutron numbers 20 and 28. Meanwhile, the $B(E2)$ value is at a minimum at these two neutron numbers.

This high 2^+ energy and low $B(E2)$ is the signature of a closed shell. For the more neutron-rich nuclei this signature is less pronounced. The 2^+ energy and $B(E2)$ for ^{44}S are intermediate between the values that one would expect for a closed shell and for a shell-breaking through deformation. In ^{42}Si , the 2^+ energy and $B(E2)$ show a complete breakdown of the shell closure. The transition between spherical and deformed shapes in ^{44}S is what makes this nuclide so interesting to study.

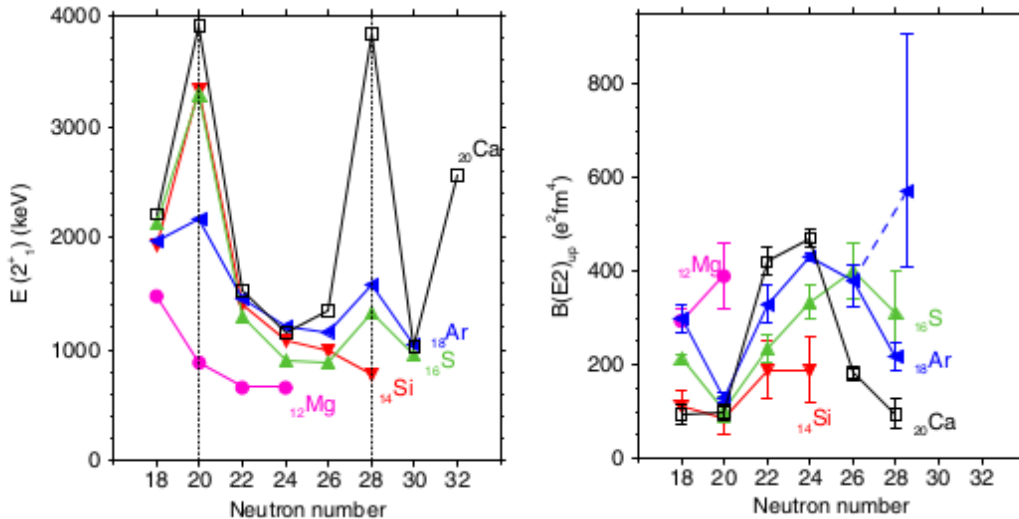


Figure 2.1: Showing the 2^+ Systematics for Nuclei in the $N=28$ Region [3]. Notice that the $N=28$ shell gap appears intact at ^{48}Ca , but shows significant weakening for ^{44}S .

2.1.2 Previous Studies on ^{44}S

The 2^+_1 excited state in ^{44}S was first measured by Glasmacher et al.[18] in 1997 using intermediate-energy Coulomb excitation. Glasmacher determined the energy to be 1297 (18) keV and the $B(E2:0^+_1 \rightarrow 2^+_1)$ to be 314(88) $e^2\text{fm}^4$. These values indicated that ^{44}S is in-between a closed shell and deformed configuration. This experiment of Glasmacher suggested that the 0^+ ground state and 2^+ 1st excited state are created by the promotion of two neutrons across the $N=28$ shell gap, creating two holes in the $f_{7/2}$ orbital, thus allowing for a deformed shape. An experiment by Grevy[19] and Force[20] detected an isomeric 0^+_2 state formed by a closing of the shell at $N=28$. This 2nd 0^+ state was firmly placed at a higher energy than the 2^+ excited state by the detection of conversion electrons as it decayed directly to the ground state and by the detection of delayed γ rays coming from the decay of the $0^+_2 \rightarrow 2^+_1$. Force applied a simple 2-state mixing model to argue for prolate-spherical shape coexistence within ^{44}S [20].

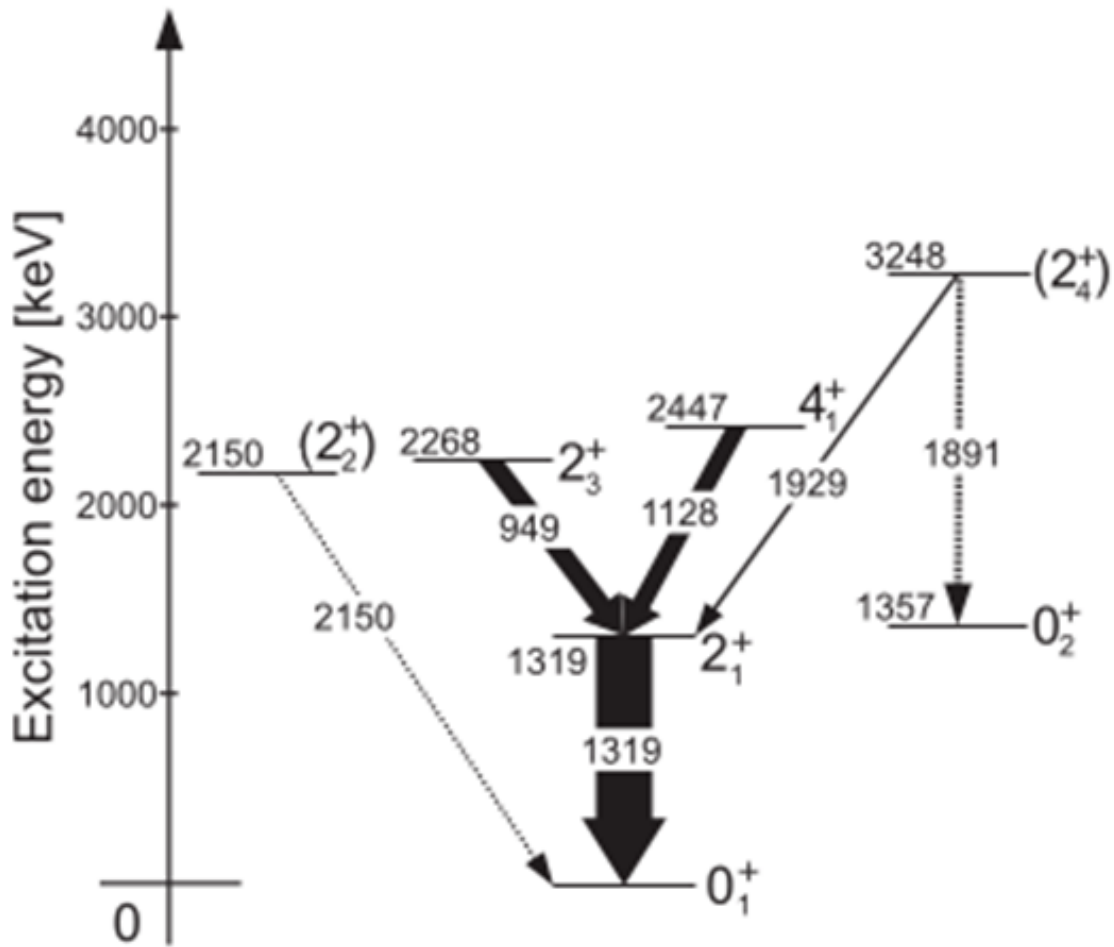


Figure 2.2: The level scheme for ^{44}S observed by Santiago-Gonzalez et al.[4]. Shell model calculations suggest that the observed 4^+ is not apart of the ground state band and is a hindered transition.

An experiment by Santiago-Gonzalez[4] suggested that a third neutron configuration could play a prominent role in the structure of ^{44}S . They observed a possibly isomeric 4^+ state that shell model calculations suggest would be formed by the promotion of a single neutron across the shell gap[4]. The level scheme proposed by Santiago-Gonzalez is shown in Figure 2.2. This 4^+ state would decay to the 2^+ state by a hindered E2 transition, meaning that the signature of this state would be a relatively long lifetime of about 60ps. The shell model study presented by Santiago-Gonzalez suggested that this 4^+ state is the beginning of a $K=4$ band, not the rotational 4^+ that one might naively expect. Interestingly enough, according to shell model calculations, the rotational

4^+ excited state should be at a similar energy to this isomeric 4^+ excited state, but the shell model calculations of [4] show very little mixing between the two states. The properties of this 4^+ state can be quantified using the lifetime of this state. The present work reports on the measurement of the lifetime of the 4_1^+ state using the recoil distance method (RDM).

2.2 Experimental Details

This experiment was performed at the National Superconducting Cyclotron Laboratory (NSCL) at Michigan State using the Gamma-ray energy tracking in-beam nuclear array, GRETINA, and the S800 Spectrometer. ^{44}S was produced in two steps. First, fragmentation of ^{48}Ca was used to produce ^{46}Ar which was selected by the A1900 separator. The ^{46}Ar beam had an energy of 99 MeV/u with a momentum spread of 1%, a purity of greater than 90%, and an intensity of 5.6×10^4 pps. The ^{46}Ar beam was then directed on a 92.4 mg/cm^2 (0.5mm) thick ^9Be target inside of GRETINA. The ^{44}S was produced via a two-proton knockout reaction and the isotopes of interest were selected by the S800.

The experiment was split into two parts. First a 'target-only' run was performed for 14 hours in order to reproduce the experiment of Santiago-Gonzalez et al[4]. and to firmly establish the level scheme. The analysis of this data will be discussed in Section 2.3. Second, an 841 mg/cm^2 (1mm) Niobium degrader was placed downstream of the target and a recoil distance method (RDM) measurement was performed. Target-degrader distances of 3mm, 6mm, and 25mm were used to measure the lifetime of ^{44}S . The analysis of the RDM measurement will be discussed in Sections 2.4 and 2.5.

2.2.1 Particle Identification with the S800 Spectrometer

The reaction residues created at the target are bent by a large magnet that separates the residues in terms of their momentum to charge ratio. These residues are detected and characterized in the focal plane box of the S800 Spectrometer. The S800 is a large magnetic spectrometer, a detailed description of which can be found in [5] and [21]. Here, the main features will be summarized to make the particle identification discussion easier to follow. A schematic of the S800 focal plane detector box is shown in Figure 2.3. Two Cathode Readout Drift Chambers (CRDCs) are placed a meter apart at the focal plane box of the S800. These detectors are sensitive to the positions of

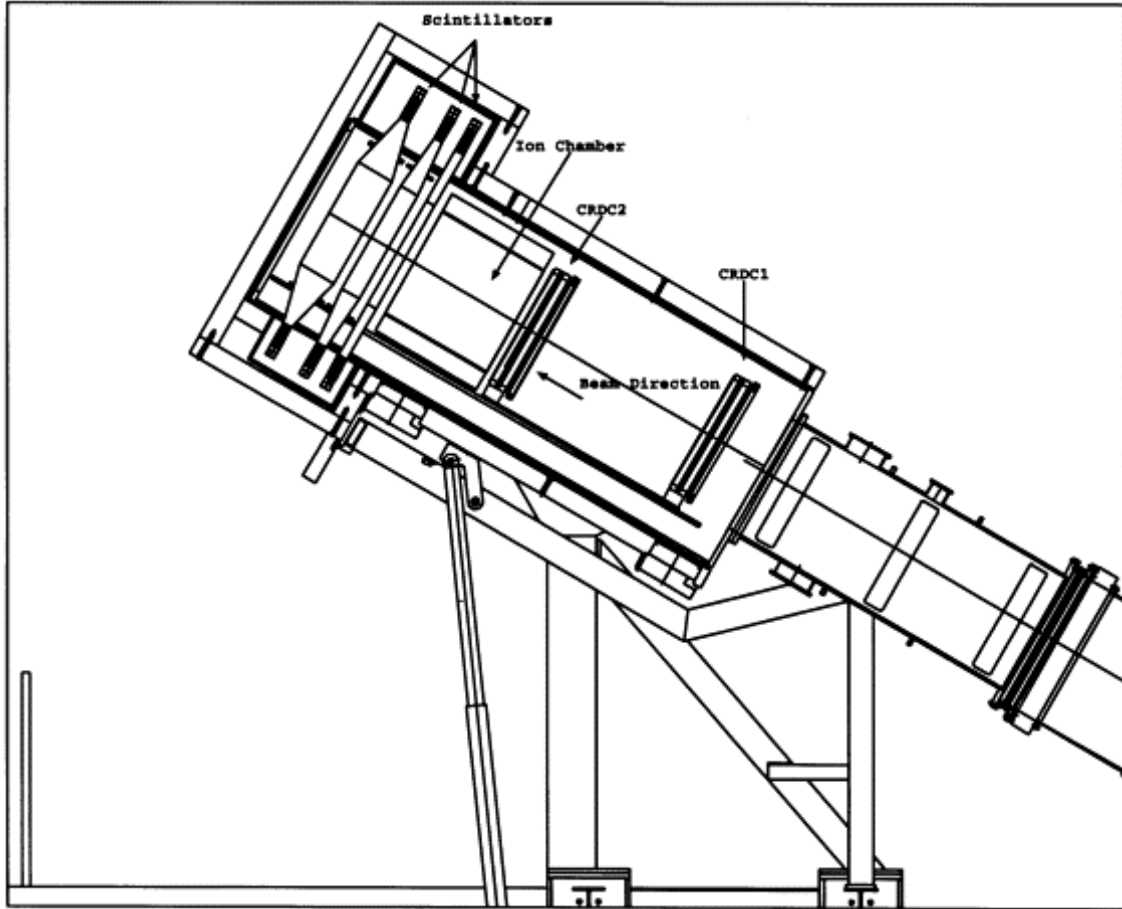


Figure 2.3: A schematic of the S800 focal plane box [5]. See text for details.

the reaction residues in the dispersive (vertical) and non-dispersive (horizontal) dimensions and are used to trace the trajectory of the residues back to the target position. Since a particle traveling straight down the axis of the S800 will reach the back on a shorter path than a particle traveling at an angle, the angle reconstructed from the CRDCs are used for time-of-flight corrections with respect to path length. Immediately after the second CRDC is an ion chamber that measures energy loss in order to determine the atomic number (Z) of the ion. After the ion chamber, there are plastic scintillators which have a fast timing response and are used both as a trigger and for time-of-flight measurements with respect to the RF of the cyclotron. Each scintillator reads out at the top and bottom so that a mean time can be used. However, in this experiment, only one output of one scintillator was operational, which limited the time-resolution slightly. When all is

working well, the S800 provides a focal plane acceptance of 5% and an energy resolution of 1 part in 10000.

2.2.2 Gamma Ray Detection with GRETINA

The γ ray energy tracking in-beam nuclear array (GRETINA) consists of 28 high-purity germanium (HPGe) detectors each split into 36 segments. The 28 detectors are housed in 7 cryostats. In this experiment, the detectors were arranged to cover laboratory angles between 22° and 85° . The angles around 70° minimize the effect of the Doppler shift and are most useful in determining the level scheme of ^{44}S , although all detectors were used for that purpose. The angles below 45° maximize the difference in Doppler shift analyzed in the RDM method and are used to determine the lifetime. To fully understand the significance of GRETINA, I will introduce some basic ideas of γ ray spectroscopy.

A Brief Introduction to Gamma ray Spectroscopy. Gamma-ray spectroscopy is the work horse of nuclear structure studies. γ ray spectroscopy is typically either done with scintillator detectors or high-purity germanium (HPGe) detectors. Scintillation detectors include materials such as sodium iodide (NaI), bismuth germanate (BGO), lanthanum bromide (LaBr), or cesium iodide (CsI). These detectors are easier to make larger than HPGe detectors and hence give a much better counting efficiency, while HPGe detectors have much greater energy resolution. Because of their excellent energy resolution, HPGe detectors are the primary tool for detailed nuclear spectroscopy experiments.

In order to understand γ -ray spectroscopy, we need to understand how γ rays interact with matter. γ rays interact with materials in three primary ways, depending on the energy of the incident γ ray. Low energy γ rays interact via the photoelectric effect, intermediate energy γ rays interact via Compton scattering, and high-energy γ rays interact via pair production. The energy ranges that these effects dominate is shown in Figure 2.4. The photoelectric effect dominates at γ ray energies of a few hundred keV or less. In this process all of the γ ray's energy is transferred onto an electron. Between a few hundred keV and a few MeV, Compton scattering dominates. Compton scattering refers to an event in which only part of the γ ray's energy is deposited onto an electron. Generally, higher energy γ rays will undergo multiple Compton scatter events before being fully absorbed by the photoelectric effect. If all of the Compton scatter events occur in the

same crystal, then the full energy of the γ ray will be collected. However, sometimes a secondary γ ray will scatter outside of the crystal and only part of the γ ray's energy will be collected. These incomplete events add background to any γ ray spectrum and need to be reduced as much as possible. Finally, high-energy γ rays can interact through pair production, in which the γ ray turns into an electron-positron pair, which then annihilate, releasing two 511 keV γ rays. If the two 511 keV γ rays are detected by the crystal, then the full energy of the γ ray will be determined. However, in some cases, one or both of the 511 keV γ rays escape the crystal, resulting in peaks that are 511 keV or 1022 keV below the proper γ ray energy. These are referred to as single- or double-escape peaks. Notice that the minimum energy for pair production is 1022 keV, but the effect increases for higher energies.

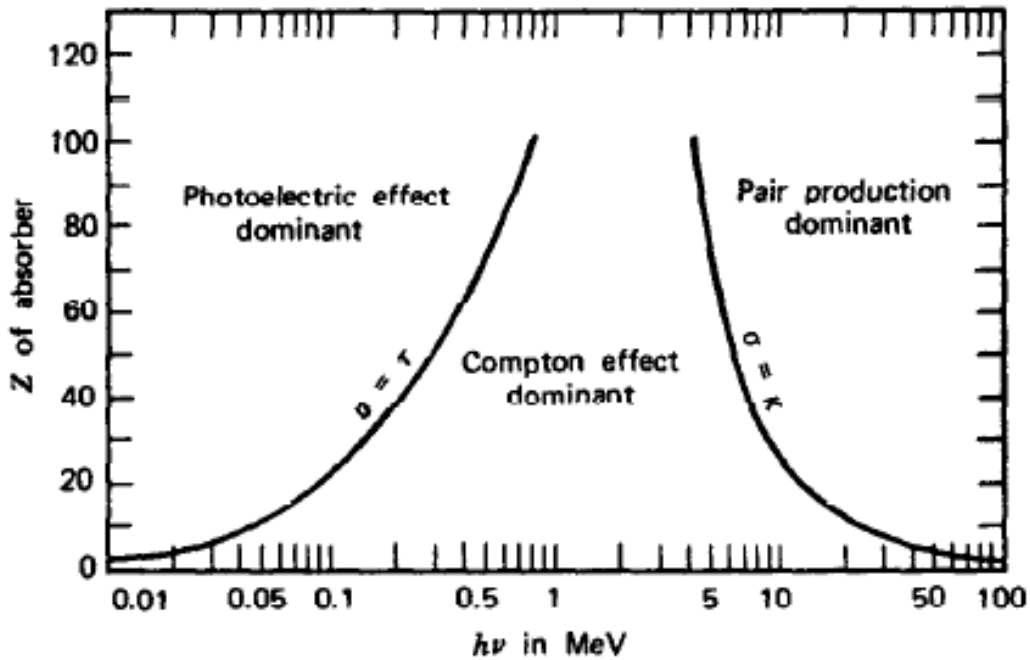


Figure 2.4: Manner in which γ rays are most likely to interact with matter as a function of energy [6]. The Compton effect dominates at energies relevant to our nuclear structure studies.

Compton Suppression via Tracking with GRETINA. Any γ ray spectrometer aims to be able to reduce the Compton background in its spectrum. The Compton background arises from events in which the γ ray scatters off of an electron in the HPGe crystal and then leaves the detector,

not depositing its full energy. The traditional way of suppressing the Compton background is to surround the HPGe detectors with a heavy scintillator material and to suppress all events in which the HPGe and the scintillator fired in coincidence. This method is employed in the γ array at FSU and will be discussed in the next chapter.

GRETINA represents a new generation of γ ray detector that suppresses the Compton background via add-back and tracking. The first step to reduce the Compton background is to group all of the interaction points into clusters and to add the energy of the interaction points together to give the total energy of the cluster. This step is referred to as “add-back”. The clustering of the interaction points is performed via an algorithm described in [22]. The angle between each interaction point and the target location is determined. All γ rays that fall within 20° of each other are put into the same cluster. The cluster can be larger than 20° because each interaction point is treated as the center of the cluster. By itself, the clustering algorithm increases the peak-to-total ratio and decreases the Compton background.

This attribution of a group of deposited energy-portions to the scattering of one individual photon already leads to a significant improvement of the peak-to-total of the reconstructed γ -ray spectra. In addition, the details of individual energies deposited and their locations can be used to further improve the quality of the reconstructed spectra. It should be noted that GRETINA, like all available γ -ray detectors, does not provide sufficient time-resolution to determine the scattering sequence of γ -interactions within the detector, which are separated by less than 300 ps, while the time-resolution of γ -detection is not better than 10 ns. Nevertheless, the individual portions of deposited energy can be compared to a hypothesis of a photon scattering through multiple Compton- and one Photo-effect interactions, and whether the detected portions and locations are consistent with the Compton-scattering formula, which is realized through a ”tracking” algorithm. The tracking algorithm makes use of the energy-angle relationship that Compton scattered γ rays must follow. A γ ray that Compton scatters off of an electron has a change in energy given by the following formula:

$$E_{\gamma,scattered} = \frac{E_{\gamma}}{1 + \frac{E_{\gamma}}{m_e c^2} (1 - \cos(\theta))} \quad (2.1)$$

The mass of the electron, m_e , is constant, so the scattered energy only depends on the incident energy and the angle at which it is scattered. Suppose now, for example, that a GRETINA event

has three interaction points clustered together. The ordering is not known, so there are six possible ways these events could be arranged. The GRETINA tracking algorithm tries all six. For the first permutation, the angle between the first and second interaction point is determined. The expected scattering energy is then calculated and compared to the actual energy of the 2nd interaction point. If these energies are close, then it is likely the correct sequence. The tracking algorithm then does the same thing for the 2nd and 3rd interaction points, determining if the energy makes sense with what would be expected. It then moves on to the second permutation. In the end, the path of the γ ray is determined by looking at all permutations of the interactions and determining which permutation can be most convincingly interpreted with the Compton scattering formula. From the quality of the scattering fit, the algorithm returns a value between zero and one that corresponds to the probability that all of the γ ray's energy was deposited in the detector. The user can then set a threshold that rejects all events below a certain probability.

Doppler Shift with GRETINA. All γ rays that are emitted from a moving source will have their energy shifted relative to what would be detected from a stationary source. One of the important aspects in high-resolution γ ray spectroscopy is to accurately correct for this Doppler shift. The amount that a γ ray is Doppler shifted depends on the velocity of the source and on the angle between the source and the detected γ ray, shown in equation 2.2. The ability to accurately apply a Doppler correction then comes down to the ability to measure the velocity (speed and direction) of the recoil and the interaction point of the γ ray in the HPGe detector, which determines θ .

$$E_{lab} = \frac{\sqrt{1 - \beta^2}}{1 - \beta \cos(\theta)} E_{com} \quad (2.2)$$

To obtain the best energy resolution with GRETINA, two things need to be done. The interaction point of the γ ray with GRETINA needs to be determined with high precision and the velocity (speed and direction) of the recoil needs to be determined with the S800. To determine the interaction point in GRETINA, the interaction points were clustered as described in the previous section and the interaction point with the largest energy was chosen as the first interaction point. Note that the tracking algorithm described earlier was not used to determine the interaction point. This is consistent with a recent paper by Weisshaar et al.[23] which concluded that using the largest

energy interaction as the first interaction point is currently a better choice than using the tracking algorithm.

At this point I would like to emphasize a point about GRETINA. The superior position resolution obtained by GRETINA is a significant improvement over the previous generation of detectors that allows for the success of the recoil distance method in this experiment. The previous experiment by Santiago-Gonzalez et al.[4] used a very similar set-up to the current experiment, with the main difference being that Santiago-Gonzalez et al. used SeGA instead of GRETINA to detect γ rays. SeGA is a segmented HPGe array that can achieve a position resolution of 1cm. Using GRETINA, we are able to achieve a position resolution of 2mm that results in an energy resolution about twice as sharp as the experiment using SeGA.

2.2.3 Lifetime Measurements using DSAM or RDM

High-resolution γ ray spectroscopy with HpGe detectors has made it possible to determine the lifetime of excited states by measuring the Doppler-shifted energy of a γ ray and correlating it with the velocity of the recoiling nucleus. The recoiling nuclei change their velocity as they pass through material on a time scale of sub-pico seconds. Thereby, correlating the recoil velocity with γ ray emission allows for measuring level-life times down to the level of 1 ps. The traditional way to measure the lifetime of an excited state would be to use the Doppler Shift Attenuation Method, or DSAM. In DSAM, the recoiling nuclei are completely stopped in the target or in some material just past the target. This way, if the state of interest has a lifetime comparable to its flight time, some of the nuclei would decay in flight and some would decay after being completely stopped. Doppler correcting for a stationary source would then produce a sharp peak corresponding to γ rays emitted from a stopped source and a tail corresponding to γ rays emitted in-flight with a continuously decreasing velocity. The lifetime of an excited state can be determined using this method. However, measuring the lifetime of an excited state in ^{44}S , or in any other exotic nuclei, presents a challenge because the reaction produces a little ^{44}S compared to all of the other reaction products. In this experiment only about 2% of the recoils detected in the S800 correspond to ^{44}S . To actually study ^{44}S , we have to select the ^{44}S nuclei that we produce and only study γ rays that were detected by GRETINA in coincidence with a ^{44}S nucleus. Clearly, we cannot completely stop the nuclei inside of GRETINA and identify which nucleus is which, so we have to modify the lifetime measurement as presented above.

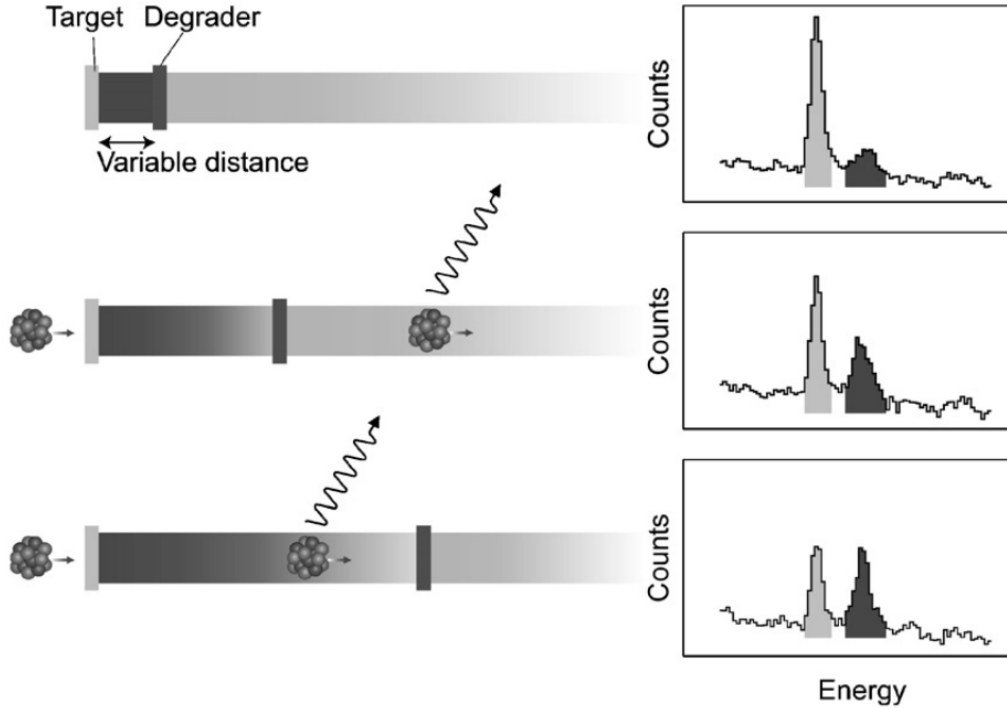


Figure 2.5: The Recoil Distance Method [7]. A degrader is placed downstream of the target location to slow the recoiling particles by about 10%. For each γ ray transition, two peaks will be observed. One peak corresponds to decays that occur before the degrader and the other peak corresponds to decays that happen after the degrader. The lifetime of the state can be extracted by moving the location of the degrader, which will shift the relative intensities of the two peaks.

To measure the lifetime of ^{44}S , the recoil-distance method with the so-called Plunger setup developed by the Cologne-NSCL collaboration was used[24]. A schematic of the recoil-distance method is shown in Figure 2.5. The recoil-distance method works by placing a second material, referred to as a degrader, some millimeters behind the target. In this experiment, the degrader was 841 mg/cm^2 (1mm) Niobium. Instead of stopping the nuclei entirely, the degrader is thick enough to reduce the velocity by 10-15%. The method is based on the ^{44}S nucleus being produced in the target. The short-lived states decay immediately and are Doppler-shifted correctly to a sharp peak. The longer lived states decay somewhere downstream of the target. If the degrader is in an appropriate position, some of the ^{44}S will decay past the degrader. If this happens, the ^{44}S nucleus will be traveling with a velocity around 10% less than expected when it emits its γ ray, so the γ

ray will be Doppler-corrected to an incorrect energy. Any long-lived excited state should then have two peaks: One peak corresponding to decays that happen before the degrader, and one peak that corresponds to decays that happen after the degrader. By moving the position of the degrader, the decay curve of an excited state in ^{44}S can be extracted.

However, in the real experiment, other effects appear. Besides slowing the reaction products down, the degrader also behaves as a target. The result of this is that for every excited state, whether it be a fast or slow transition, there are two peaks in the γ ray spectra. One peak corresponds to excited states that were produced in the target and decayed before the degrader. The other peak corresponds to excited states that were produced in the target and decayed after the degrader AND excited states that were produced in the degrader. The goal is to account for the portion of the degrader peak that comes from excited states that were produced in the degrader. To accomplish this, one run with the degrader at a long distance was performed, where all of the excited states produced in the target would decay before reaching the degrader. Now, the two peaks in the γ ray spectra correspond to reactions in the target and reactions in the degrader with no lifetime dependence. This information is used to subtract the reactions in the degrader at shorter distances.

2.3 Analysis of “Target-Only” Data

The first part of the experiment was performed to establish the main transitions suggested by Santiago-Gonzalez et al[4]. This analysis has two key components. First, the reaction residues have to be identified in the S800, such that only γ rays that are coincident with ^{44}S recoils will be analyzed. Second, the γ rays detected in GRETINA have to be Doppler shifted correctly. This involves correctly determining the location of the interaction inside of GRETINA and reconstructing the path of the γ ray with the S800.

2.3.1 Particle Identification of Reaction Residues

The parameter used for particle identification is shown in Figure 2.6. Panel a shows the energy loss in the ion chamber plotted against the time of flight. The time of flight depends on a timing measurement made from a plastic scintillator at the end of the S800 focal plane. This time showed a discontinuity for large energies and had to be corrected. This correction is described in Appendix

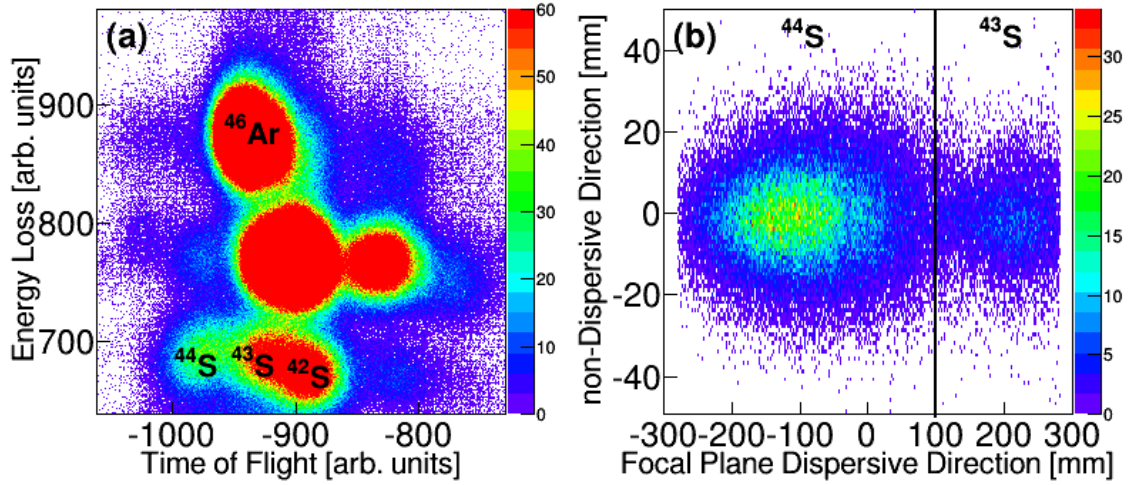


Figure 2.6: The particle identification with the S800. Panel a shows the energy loss versus time of flight. Panel b separates the recoils based on the focal plane position.

a. The different Sulfur isotopes seen in this experiment are labeled. As can be seen in Panel a, there is some overlap in the tof separation. This can be further cleaned up by looking at the focal plane position for the specific isotopes. The focal plane position separates recoils in terms of momentum and therefore in mass. Panel b of Figure 2.6 shows the focal plane position for recoils that fall within the ^{44}S gate of panel a. Using the energy loss, time of flight, and focal plane position, we can cleanly separate ^{44}S from ^{43}S .

2.3.2 Gamma Ray Detection with GRETINA

Energy and Efficiency Calibration. GRETINA already has an internal calibration applied and no further energy calibration was needed, although the calibration was checked using a ^{152}Eu source. A ^{152}Eu source was used to perform the relative efficiency calibration. The efficiency is parameterized as shown in equation 2.3. The plot of $\log_{10}(\text{Eff})$ vs. Energy is shown in Figure 2.7. Note that this calibration is a relative calibration and does not give the absolute efficiency of the array. Also note, that the efficiency actually decreases below 100 keV, a feature not shown in the fit. One of the advantages of GRETINA is that it has an absolute efficiency of about 7.5% at 1 MeV, a significant improvement over previous arrays.

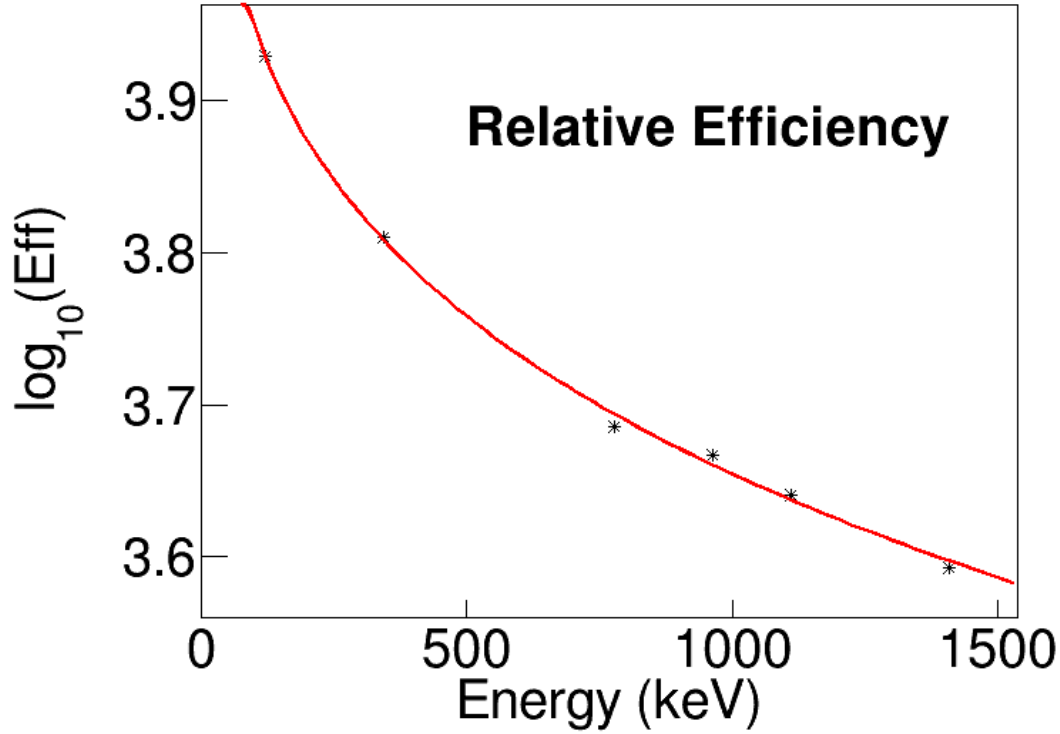


Figure 2.7: The relative efficiency of GRETINA as a function of energy. Note that this efficiency calibration is done relative to the area of the 121 keV peak in ^{152}Eu .

$$\log_{10}(\text{Eff}) = A + B\log_{10}(E) + C\log_{10}(E)^2 + \frac{D}{E^2} \quad (2.3)$$

Doppler Shift Correction with GRETINA. The velocity of the reaction residues was determined using the S800 spectrograph. The residues entering the S800 are bent by a magnet and are therefore separated by their momentum-to-charge ratio. For residues entering the S800 with the same charge, this spatial separation is effectively a separation in momentum. The S800 has two position-sensitive CRDCs that determine the location and angle of the particle in the focal plane. This distribution is then traced back to the target location using an inverse map. The momentum distribution at the target location is referred to as the DTA. The direction of the residues is determined directly from these reconstructed angles and the velocity is determined from the DTA. A check to see if the velocity used for Doppler reconstruction is correct is to plot the γ

ray energy against the detection angle as shown in Figure 2.8. If the Doppler correction is done correctly, the γ ray energy should be independent of detection angle. This is shown very clearly in the fast transitions at 949 and 1319 keV.

The Doppler correction was applied in two different ways for comparison. First, the reaction residue is assumed to be moving along the beam axis with a fixed velocity. Second, the reconstructed direction and velocity of the reaction residue is used. Figure 2.9 shows the Doppler reconstruction for γ rays in coincidence with ^{44}S reaction residues with both of these assumptions applied. As can be seen, using the reconstructed direction gives a modest improvement.

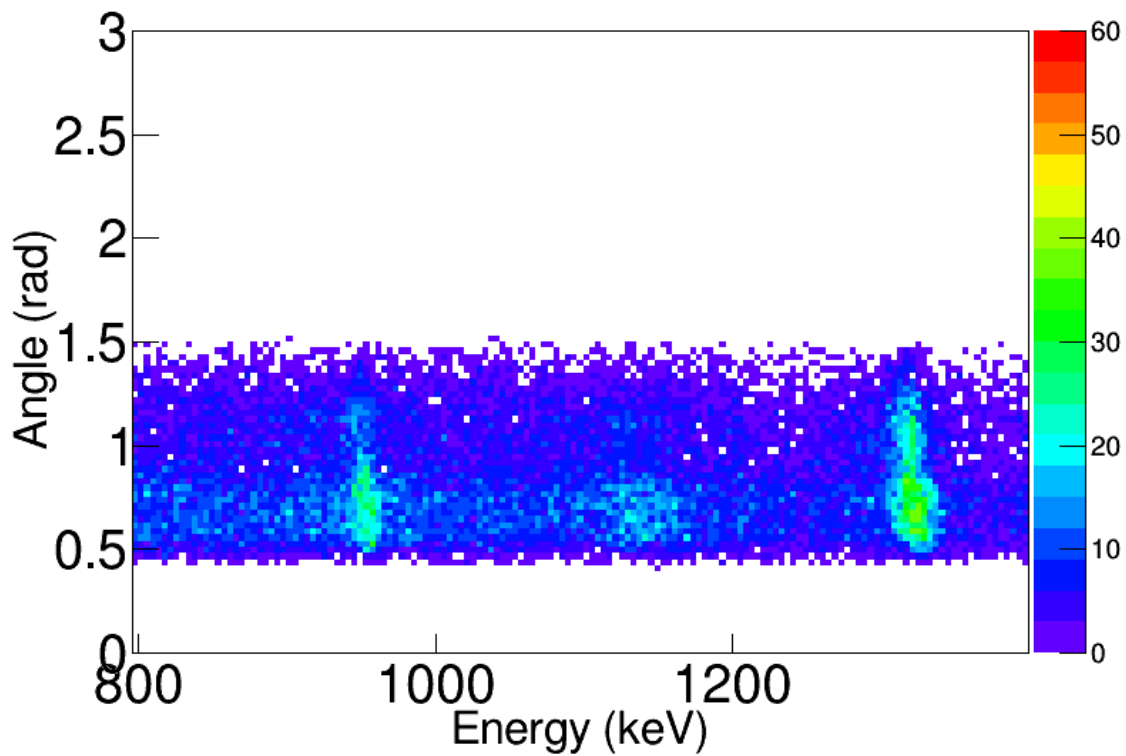


Figure 2.8: The γ ray detection angle vs. the γ ray energy. The energy of the γ ray is independent of detection angle, showing that the Doppler correction is performing well.

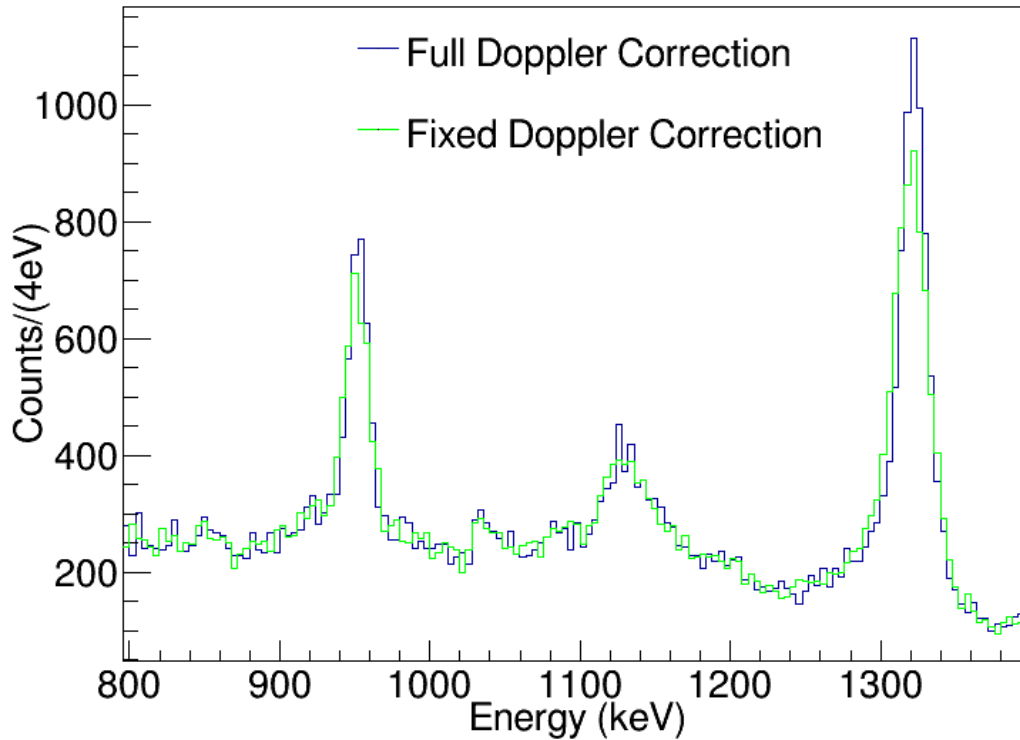


Figure 2.9: The γ ray spectra for the GRETINA data set with a full Doppler correction (recoil direction and velocity taken into account) and a fixed Doppler Correction (beam direction and fixed velocity).

Establishing the Level Scheme. In order to establish the level scheme, we performed a run with only the ^9Be target and no degrader. In 14 hours of running, this data set was able to reproduce the experiment performed by Santiago-Gonzalez et al.[4] and to establish the level scheme. This analysis makes use of γ - γ coincidence events. A coincidence means that two or more γ rays were detected in the same event which signifies their emission in a cascade from the same excited nucleus. The coincidence spectra shown in this section are simply all of the γ rays detected at the same time as a particular peak of interest.

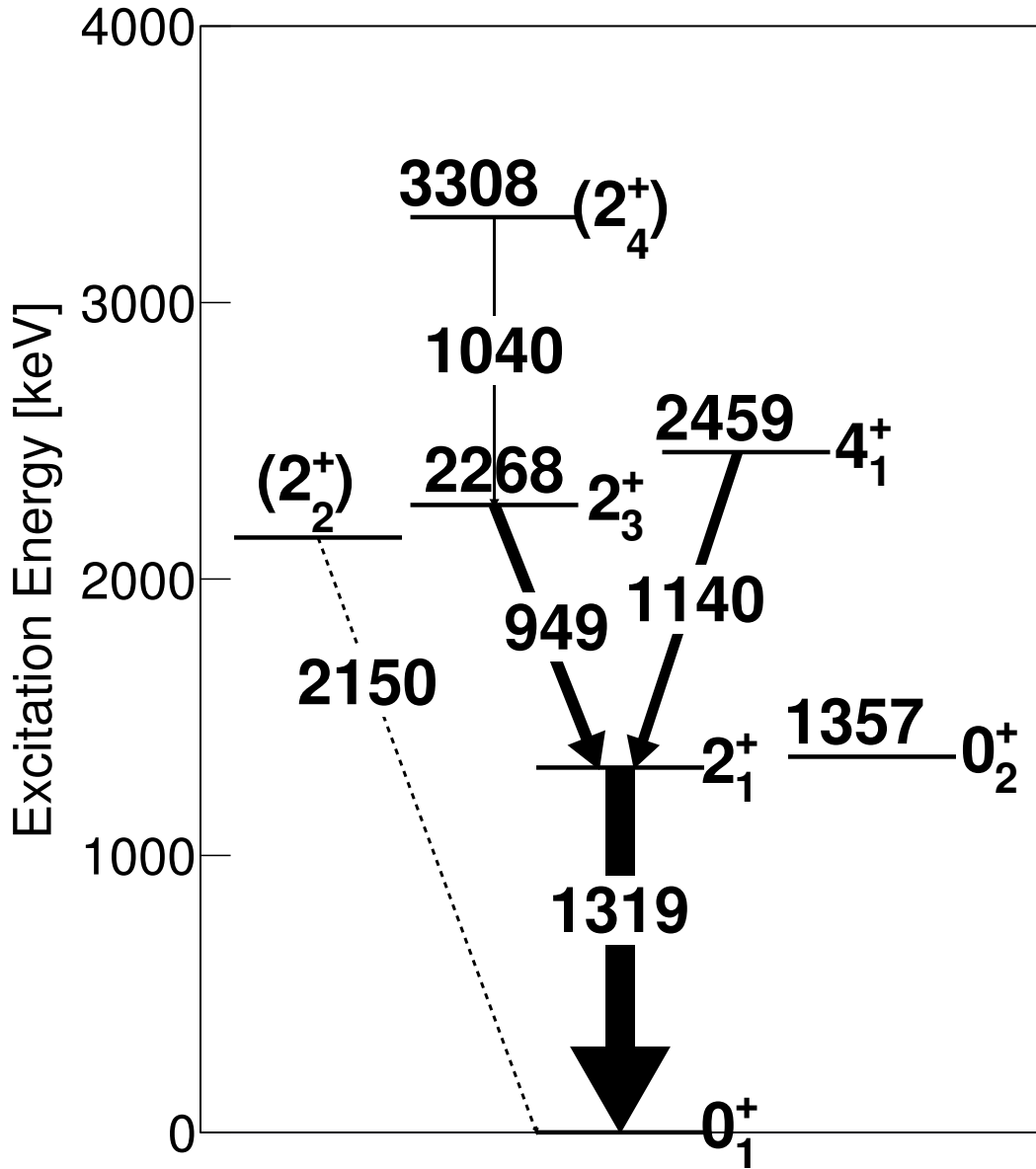


Figure 2.10: The adopted level scheme for ^{44}S . The main transitions establishing the 2_1^+ , 2_3^+ , and 4_1^+ excited states observed by Santiago-Gonzalez et al.[4] were confirmed.

The adopted level scheme is shown in Figure 2.10. Our analysis confirms the main transition placements by Santiago-Gonzalez et al. [4] establishing the 2_1^+ , 2_3^+ , and 4_1^+ excited states. Figure 2.11 shows all of the γ rays in coincidence with the 1319 keV peak. In this figure, the coincident spectra are scaled by a factor of 15 in order to appear on the same scale as the γ -singles spectrum. In

this figure it is clear that both the 949 keV transition and the 1140 keV transition are in coincidence with the 1319 keV transition. These placements are confirmed by separately gating on the 949 keV and on the 1140 keV transitions and observing that the 1319 keV peak is in coincidence with both peaks, shown in Figure 2.12 and in Figure 2.13.

A 1040 keV transition populating the 2_3^+ level has been observed by Riley et al. [25] and Caceres et al. [26]. This transition was confirmed in this work. The γ rays seen in coincidence with the 949 keV peak and with the 1040 keV peak are shown in Figure 2.12. From these two spectra, the 949 keV peak appears to be in coincidence with the 1040 keV peak, confirming the observation by [25] and [26].

A level at 3.248 MeV, proposed by Santiago-Gonzalez et al. [4], could not be confirmed in this $\gamma\gamma$ analysis. Santiago-Gonzalez et al. [4] observed γ rays at 1891 keV and at 1929 keV. The γ ray at 1929 keV showed a possible coincidence with the 1319 keV transition while the 1891 keV transition showed no coincidences. Now, the 0_2^+ level was determined to be 36 keV above the 2_1^+ level by Force et al. [20], very close to the difference in γ ray energy between the 1929 keV and 1891 keV γ rays. Because of this, Santiago-Gonzalez et al. [4] proposed that the 1929 keV and 1891 keV γ rays de-excite the same state, with the 1891 keV transition populating the 0_2^+ level, which is not observed due to its long lifetime. However, this placement was questioned by Riley et al.[25], who populated excited states in ^{44}S via a different reaction mechanism. They performed a one proton knockout reaction from ^{45}Cl as opposed to a two proton knockout reaction as in Santiago-Gonzalez et al. Riley et al.[25] observed the same two γ rays but at a different relative intensities than Santiago-Gonzalez et al. Because of the different relative intensities, Riley et al.[25] hypothesized that these two γ rays must be de-exciting different levels. The current work could not place the 1929 keV transition in coincidence with the 1319 keV transition. The γ rays in coincidence with the 1319 keV transition are shown in Figure 2.11. There is no clear signal at 1929 keV that suggests a coincidence with the 1319 keV peak. Moreover, the γ rays in coincidence with the 1929 keV peak (not shown) do not show a peak at 1319 keV.

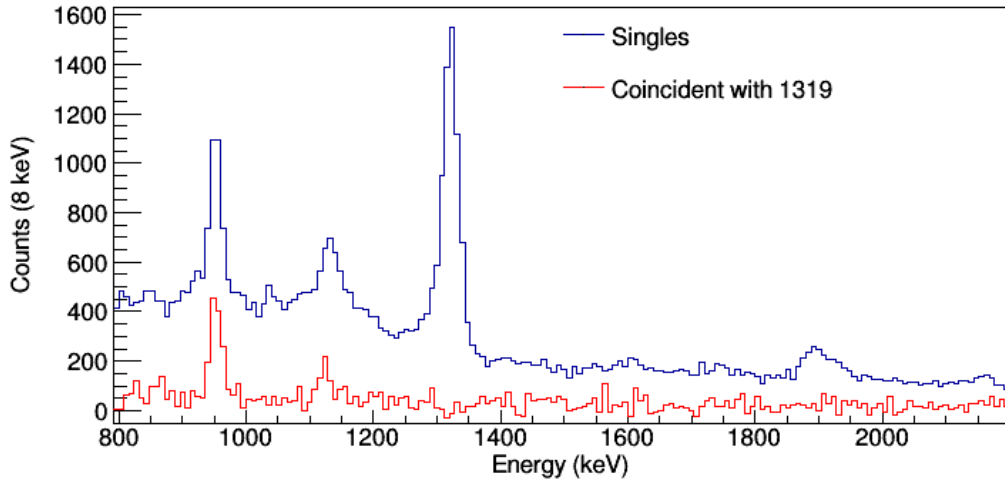


Figure 2.11: The γ ray singles spectra as well as all γ rays in coincidence with the $2_1^+ \rightarrow 0_1^+$ transition. The coincident spectrum is scaled by a factor of 15.

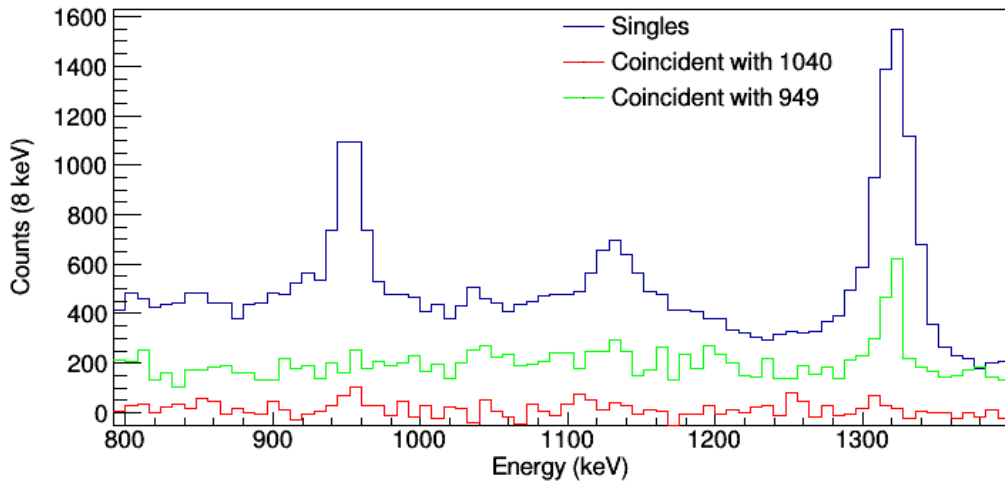


Figure 2.12: The γ ray singles spectra as well as all γ rays in coincidence with the $2_3^+ \rightarrow 2_1^+$ transition (green) and all γ rays in coincidence with the $2_4^+ \rightarrow 2_3^+$ transition (red). The coincident spectra are scaled by a factor of 15.

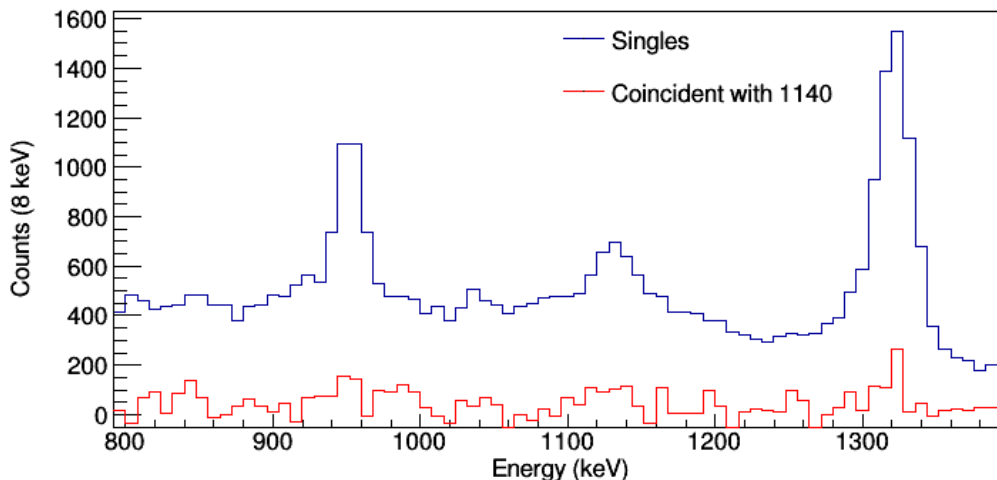


Figure 2.13: The γ ray singles spectra as well as all γ rays in coincidence with the $4_1^+ \rightarrow 2_1^+$ transition. The coincident spectrum is scaled by a factor of 15.

2.4 Analysis of the RDM Data

The lifetimes of excited states were investigated through the recoil-distance method, where the distance between the ^9Be target and the ^{92}Nb degrader was adjusted to 3 mm, 6 mm and 25 mm, which correspond to 24, 48 and 200 ps flight time, respectively, and the events from each distance setting were recorded separately. In this section we discuss the features of the target-degrader data and qualitatively establish the lifetime effect in the 1140 keV transition. This lifetime will be quantitatively determined with the help of a simulation discussed in the next section.

2.4.1 Select Target-Induced Reactions with the S800

It turns out that a significant number of the reactions that produced ^{44}S occurred on the degrader. In this section, we will discuss the kinematic parameters of these reactions such that the target-induced reactions can be selected, making this measurement more sensitive to a lifetime effect. In the target-only data set, the CRDCs have so far been used to separate ^{44}S from ^{43}S , and to reconstruct the residue velocity and direction. Additionally, they can be used in the RDM measurement to selectively reduce the amount of degrader-induced reactions. To understand this reduction, we first have to consider some of the reaction kinematics.

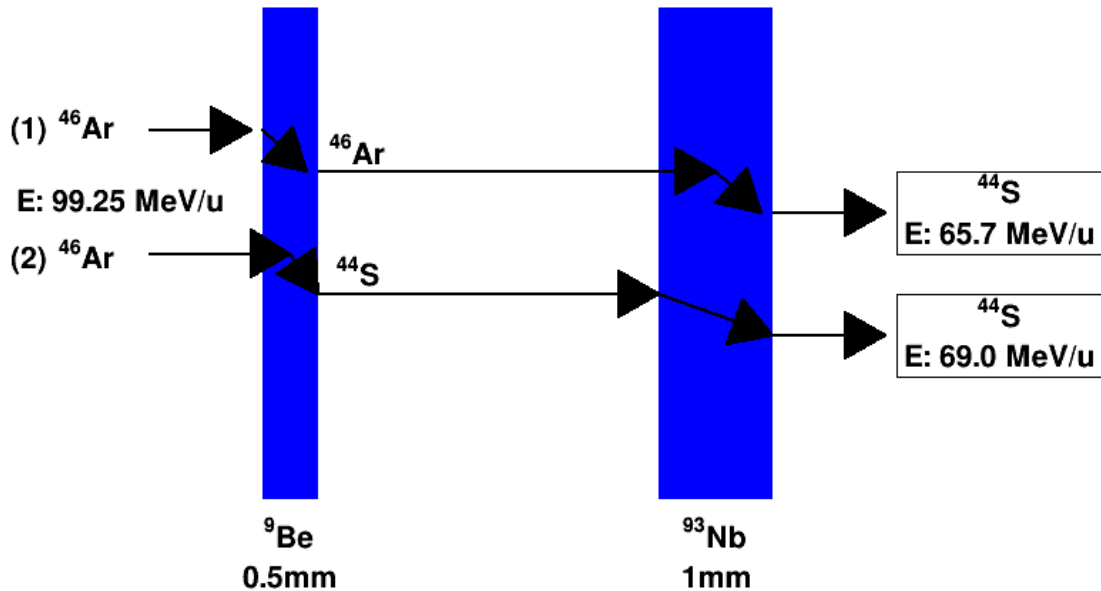


Figure 2.14: Schematic diagram showing energy loss in target and degrader. A reaction that occurs in the degrader (Path 1) will result in a lower energy reaction than a reaction that occurs in the target (Path 2).

The beam traveling through the target and degrader will lose energy due to interaction with matter. The exact location of the knockout reaction will affect the final energy of the recoil which affects the γ ray Doppler shift, whether the recoil is accepted by the S800, and where it is detected in the S800 focal plane. This concept is shown in Figure 2.14. Figure 2.14 illustrates the difference in final energy that is expected for a reaction that occurs half way through the degrader (1) versus a reaction that occurs half way through the target (2). The reaction that occurs in the degrader will result in a lower energy reaction than a reaction that occurs in the target because ^{46}Ar has two more protons than ^{44}S (and energy loss is proportional to charge).

The S800 can detect this difference in energy by detecting the position of the recoil in the dispersive plane using the CRDCs as discussed above. The DTA information can be used to separate target-induced reactions from degrader-induced reactions. As illustrated in Figure 2.14,

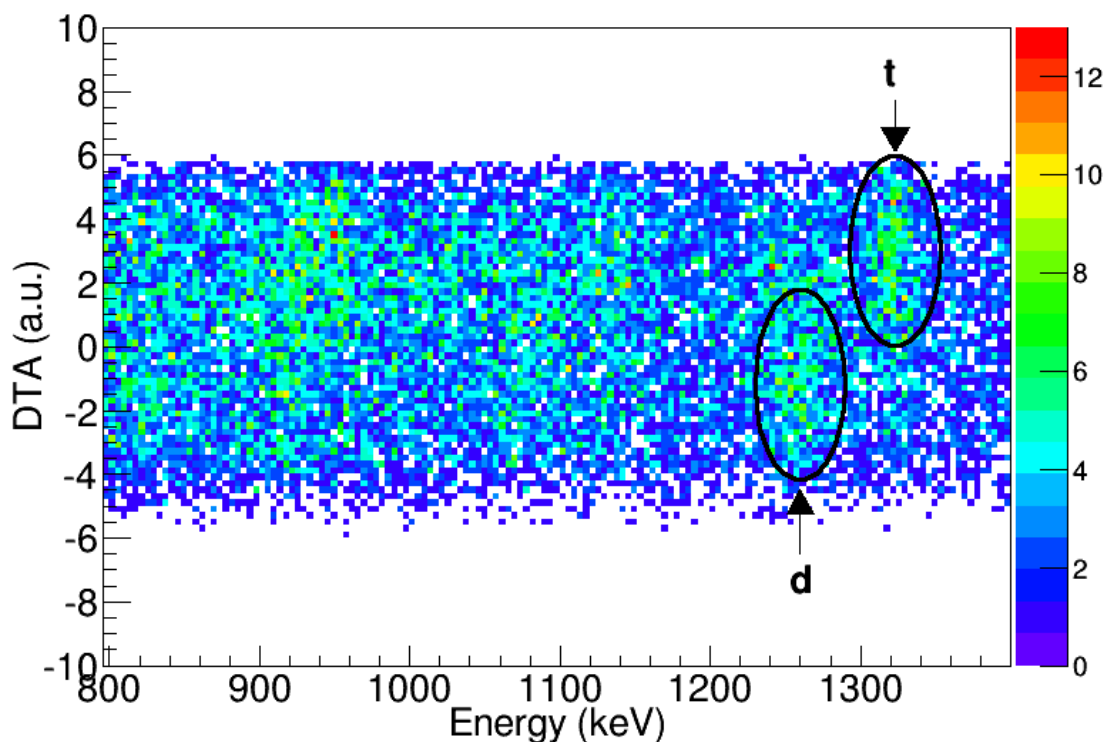


Figure 2.15: The effect discussed in Figure 2.14 is clearly seen in the long distance data. The momentum spread is plotted against γ ray energy for γ rays in coincidence with ^{44}S recoils at the long (25mm) target-degrader distance. The degrader-induced reactions (labeled d) are clearly shifted along the DTA axis with respect to the target-induced reactions (labeled t).

target-induced reactions have a larger momentum than degrader-induced reactions. This can be clearly seen in the data by looking at the DTA plotted against the γ ray energy shown in Figure 2.15. Figure 2.15 plots the DTA on the y-axis and the γ ray energy on the x-axis for the long distance (25mm) data. All γ rays are Doppler corrected assuming they are emitted from the target position, so the peak that appears at the correct energy comes from reactions that occur on the target, labeled 't' in the figure. The peak labeled 'd', comes from degrader-induced reactions. One can clearly see that the degrader peak is shifted with respect to the target peak on the DTA axis. By selecting the upper half of the DTA spectra, one can preferentially select target-induced reaction events.

2.4.2 Establishing the Lifetime of the 4_1^+ State

Figure 2.16 shows the γ ray spectra observed in coincidence with ^{44}S , recorded with the target-degrader distances set to 3mm (Panel a), 6mm (Panel b), and 25mm (Panel c). The events were selected for the higher-momentum side of the S800 focal plane, which suppresses degrader-induced reactions. Additionally, the events were selected for laboratory γ -angles below 45° and were Doppler corrected assuming emission from the target position.

The long-distance run (25mm) is used to determine the amount of reactions induced on the degrader. Because of the long target-degrader distance, all γ rays from reactions in the target are expected to be emitted before the reaction residue nucleus reaches the degrader. Therefore, peaks observed at the correct γ ray energies stem from reactions in the target, labeled ‘t’ in Panel c of Fig.2.16, and peaks at shifted energies stem from reactions induced by the degrader, labeled ‘d’. Those lines are displaced in energy by an over-corrected velocity and an under-corrected γ -detection angle.

Similarly, the short-distance runs are used to determine the lifetime. Panels a and b of Figure 2.16 show the data for the 3mm and 6mm distance. Now, the γ rays that appear at the correct γ ray transition energies are labeled ‘f’ for fast transitions, and the γ rays that appear at shifted energies are labeled ‘s’ for slow transitions. Of course, all ‘slow’ peaks will include contributions from degrader-induced reactions.

There are several interesting features of these spectra. The 949 keV γ ray, associated with the $2_3^+ \rightarrow 2_1^+$ transition, has only one peak evident at the 3mm and 6mm distances, while a degrader peak does emerge at the 25mm distance. This is an effect of the very fast lifetime of the 2_3^+ state. With a lifetime of about 0.5ps, the 2_3^+ state essentially decays where it is created, so it does not have time to slow down after it is created. Therefore, reactions that occur at the beginning of the degrader have essentially the same velocity as reactions that occur at the back of the target. In this case, the difference in velocity does not give a clean separation of target-induced and degrader-induced reactions. The only thing that will separate these peaks is the angular difference coming from the physical separation in the target and the degrader. The difference in angle between target-induced and degrader-induced reactions is large enough to separate these peaks at the 25mm distance, but not at the 3mm and 6mm distances.

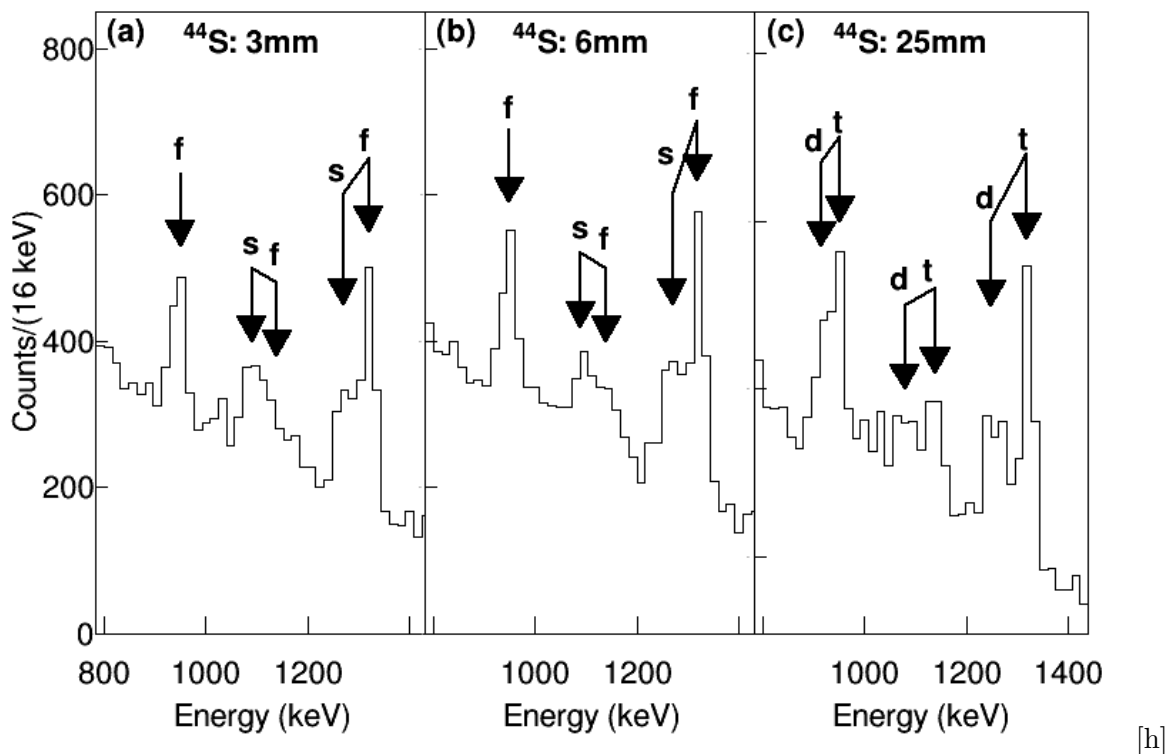


Figure 2.16: γ ray spectra observed in coincidence with ^{44}S , recorded with the target-degrader distance set to 3mm (Panel a), set to 6mm (Panel b), and set to 25mm (Panel c). For most γ transitions, two peaks are observed. For the 3mm and 6mm runs, these are labeled as “s” for slow transitions that decay past the degrader, and “f” for fast transitions that decay before the degrader. For the 25mm run, these transitions are labeled “t” for target-induced reactions and “d” for degrader-induced reactions. Notice that in the peaks corresponding to the $4_1^+ \rightarrow 2_1^+$ transition (1140 keV), most of the intensity is found in the “slow” peak for the 3mm and 6mm distance, while the intensity shifts to the “fast” peak at 25mm. This shift in intensity is indicative of a lifetime effect. In contrast, the peak corresponding to the $2_3^+ \rightarrow 2_1^+$ transition (949 keV) has all of its intensity in the ‘fast’ peak at 3mm and 6mm, indicative of a very fast transition. This lifetime is quantified in section 2.4.

If we turn our attention to the 1140 keV peak, associated with the $4_1^+ \rightarrow 2_1^+$ transition, we see a different picture entirely. For the 3mm data, there is very little evidence of a peak at the correct γ ray energy. All of the peak seems to be shifted into the slow component. This is very clearly a lifetime effect. All of the target-induced reactions that populate the 4^+ state live long enough to be slowed down by the degrader at the 3mm distance. At the 6mm distance, a 'fast' peak starts to emerge, and by 25mm, there is a clear peak at the correct energy. Clearly, the shifting intensity from the slow to the fast peak is indicative of a lifetime on the order of 10s of pico-seconds.

The transition at 1319 keV peak, associated with the $2_1^+ \rightarrow 0_1^+$ transition, has a clear peak at both the correct and shifted energies for all distances. The 2_1^+ state has a known lifetime of 3.0ps[18] which is slightly longer than the assumed lifetime of 0.5ps for the 2_3^+ state. This lifetime is short enough that we do not expect to see a significant amount of target-induced recoils live long enough to show a lifetime effect on their own. However, the 2_1^+ state will show a lifetime effect indirectly through the feeding from the 4_1^+ state. The decay of the direct population of the 2_1^+ should show an intermediate line shape between the 2_3^+ and the 4_1^+ . The prominence of the slow peak at all distances is an indication of a lifetime effect coming indirectly from the population via the 4_1^+ level. This lifetime effect will be quantified with the use of a simulation in the next section.

2.5 Using the Geant4 Simulation to Determine the Lifetime

In order to quantify the lifetime of the 4^+ state that we observe, we compare the experimental spectra to the results of a Monte-Carlo simulation [7], which models the population of excited states, the emission of γ ray cascades and the location of emission events as a function of the level lifetimes. The simulation also includes the energy loss in target and degrader materials and the emission kinematics in the generation of laboratory-system γ rays. Finally, it simulates the interactions of these γ rays with GRETINA's Germanium crystals and selects the events according to the acceptance of the S800 spectrograph. For comparison with the experimental spectra, the simulated γ -detections are then Doppler corrected in the same way as the measured events.

2.5.1 Comparing Simulation to the Data with χ^2 Test

The simulated spectra are compared to the data using a χ^2 test, so we will discuss that here before discussing the details of the simulation. The χ^2 is a measure of the goodness of fit, given

by equation 2.4[27]. In this equation, a_j and a'_j are the observed and simulated values. The denominator of this equation is the square of the statistical error. Assuming a Poisson distribution, the statistical error is equivalent to \sqrt{N} , so the square of the statistical error is just the number of counts in the bin, a_j .

$$\chi^2(\tau) = \sum \frac{(a_j - a'_j)^2}{a_j} \quad (2.4)$$

In this paper, the χ^2 is plotted as a function of various parameters, discussed specifically below. The individual data points are created by applying equation 2.4 to each bin around the peak of interest and summing over these bins. In comparing the simulation to the data, an exponential background was added to the simulation by requiring that the simulated background fit the background of the data above the 1319 keV peak and below the 949 keV peak. The same exponential background was used to fit the 3mm and 6mm runs. Additionally, the simulated spectra are normalized to the area of the 949 keV peak.

The χ^2 distribution has a quadratic dependence on the parameter that is varied and the minimum and uncertainty can be taken out of a quadratic fit to this data[27]. The uncertainty, σ , comes from the second derivative of the quadratic fit, as described in equation 2.5.

$$\sigma^2 = 2 \left(\frac{\delta^2 \chi^2}{\delta a_j^2} \right)^{-1} \quad (2.5)$$

2.5.2 Setting Up the Simulation Parameters

The central component of the simulation is the correct representation of the reaction kinematics. The reconstruction of the kinematics in the data was discussed in the preceding section. The simulation is set-up in the following manner. The energy loss of the beam traveling through the target and degrader was determined with dedicated unreacted particle runs. Three data runs were performed where the S800 was set up to look at the scattered beam. One run was done with no target or degrader, one was done with just the target, and one run was done with a target and a degrader. The target and degrader material and thickness was input into the simulation and a parameter was adjusted to match the beam energy after the target and after the degrader. The comparison between the measured beam energy in the S800 and the simulated beam energy is shown in Figure 2.17.

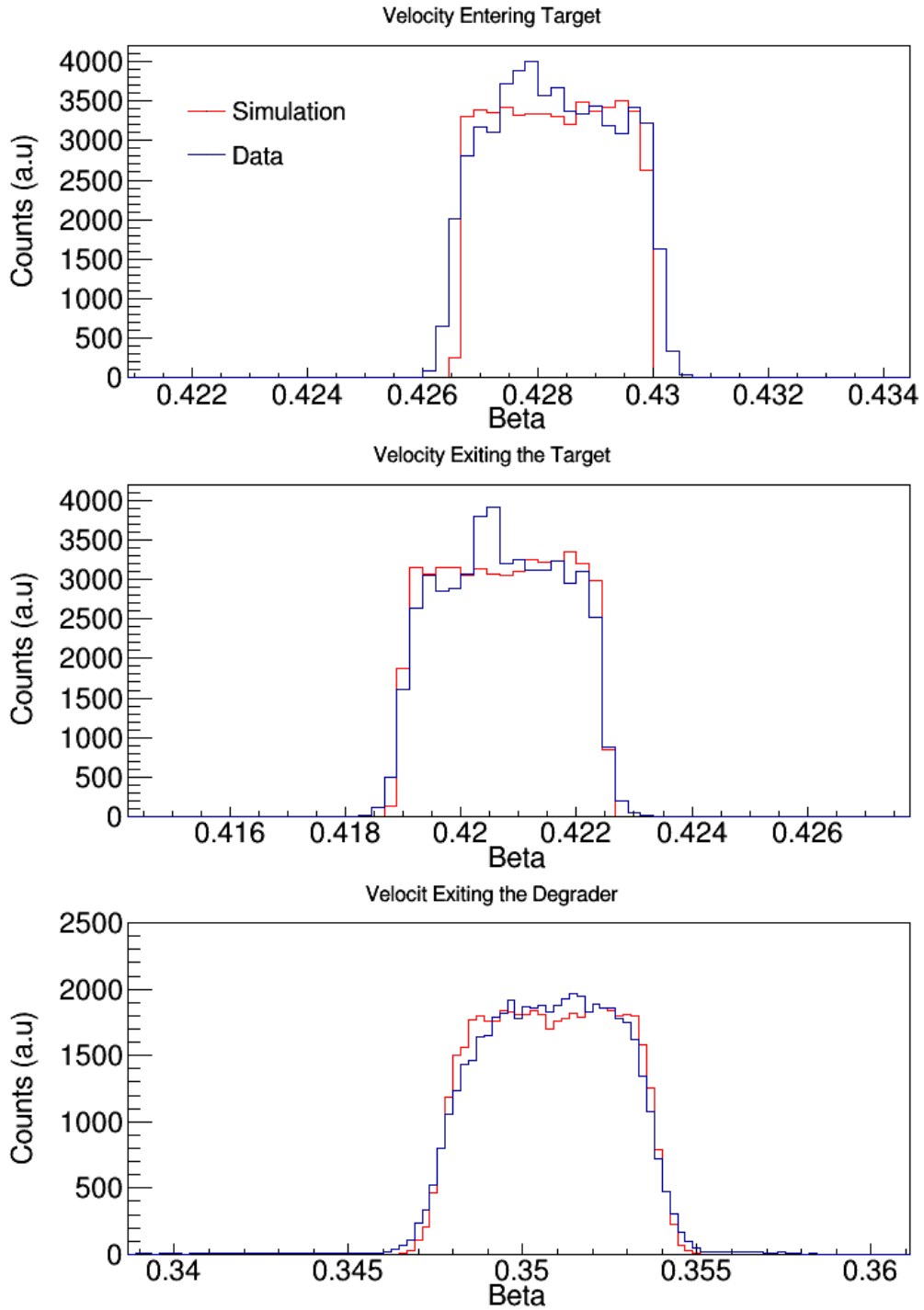


Figure 2.17: The simulated velocity in comparison to the measured velocity for scattered ^{46}Ar beam before the target (Panel a), after the target (Panel b), and after the degrader (Panel c).

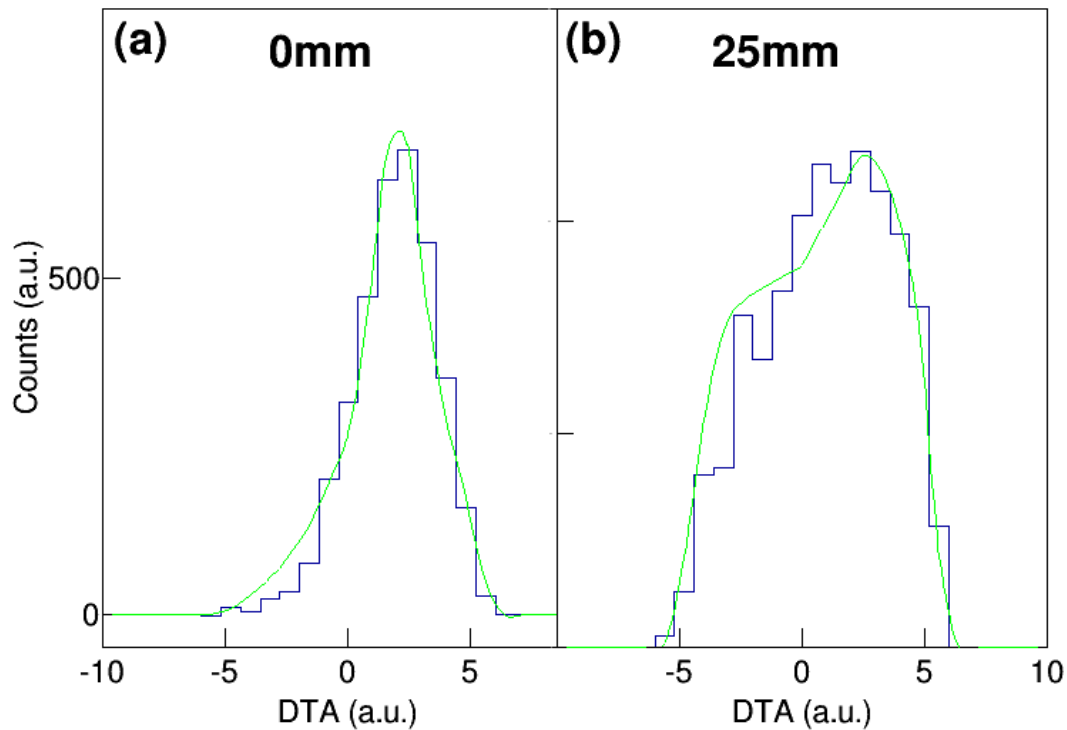


Figure 2.18: Comparing the simulated to measured DTA for the target-only run (Panel a) and for the long distance run (Panel b). The simulated DTA spectra is calculated from the final momentum of the reaction residues leaving the degrader, while the DTA from the data is measured in the S800.

Beyond the energy loss of the beam moving through the target, some energy loss occurs during the reaction itself. The best way of looking at the beam energy is to look at the DTA measured by the S800. The simulated DTA spectra are calculated from the final momentum of the reaction residues leaving the degrader, while the DTA from the data is measured in the S800 as discussed above. The simulated spectra is compared to the measured DTA spectra to determine the energy loss and width due to the reaction. These parameters are fixed from data of the target-only run and used in the target-degrader runs. The comparison for the target-only run is shown in panel a of Figure 2.18 and the long distance comparison is shown in Panel b.

The DTA is used to model the selection of the reaction residues in the S800. It turns out that the acceptance of the S800 not only depends on the momentum of the residues, but also on the

angle of the residues leaving the target. A reaction residue of a given momentum that leaves the target at a low angle may fall within the S800 acceptance while a particle with the same momentum but a larger angle may not be accepted. This acceptance occurs naturally in the data, as shown in Figure 2.19, but the simulation allows for all energy-angle combinations. To match the simulated acceptance to the data, a cut was drawn around the measured acceptance and applied to the simulated events.

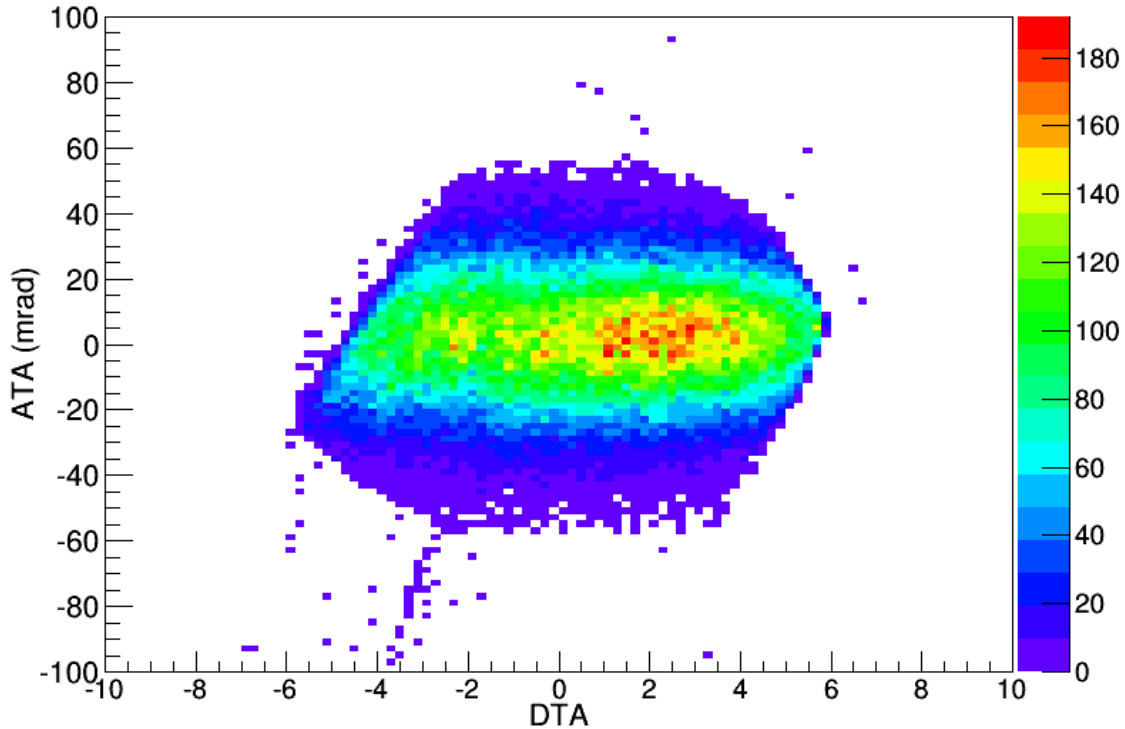


Figure 2.19: The angle of the reaction residues (ATA) plotted against the momentum of the reaction residues (DTA) for residues detected in the 25mm data run. The S800 acceptance depends both on the momentum and on the angle of the residues leaving the target. A cut was applied to the simulated events to match this energy-angle relationship.

2.5.3 Setting up the Parameters of the Level Scheme

Before we turn our attention to the target-degrader runs, we use the target-only runs to correctly reproduce the target-induced reactions. First, we can check the efficiency of the simulated GRETINA versus the efficiency of the real GRETINA. A simulated source run with ^{152}Eu was

performed and the extracted efficiencies are compared to the efficiencies obtained with the real data. Figure 2.20 shows the comparison between the relative efficiencies obtained from the simulation and from the data. It compares the efficiency both with add-back on and off. The add-back performed in the simulation is based on the same routine performed in the data analysis, described earlier. As can be seen in the figure, the relative efficiencies for the data and the simulation agree well with one another. Additionally, by using add-back, the efficiency is significantly improved for all energies greater than 200 keV.

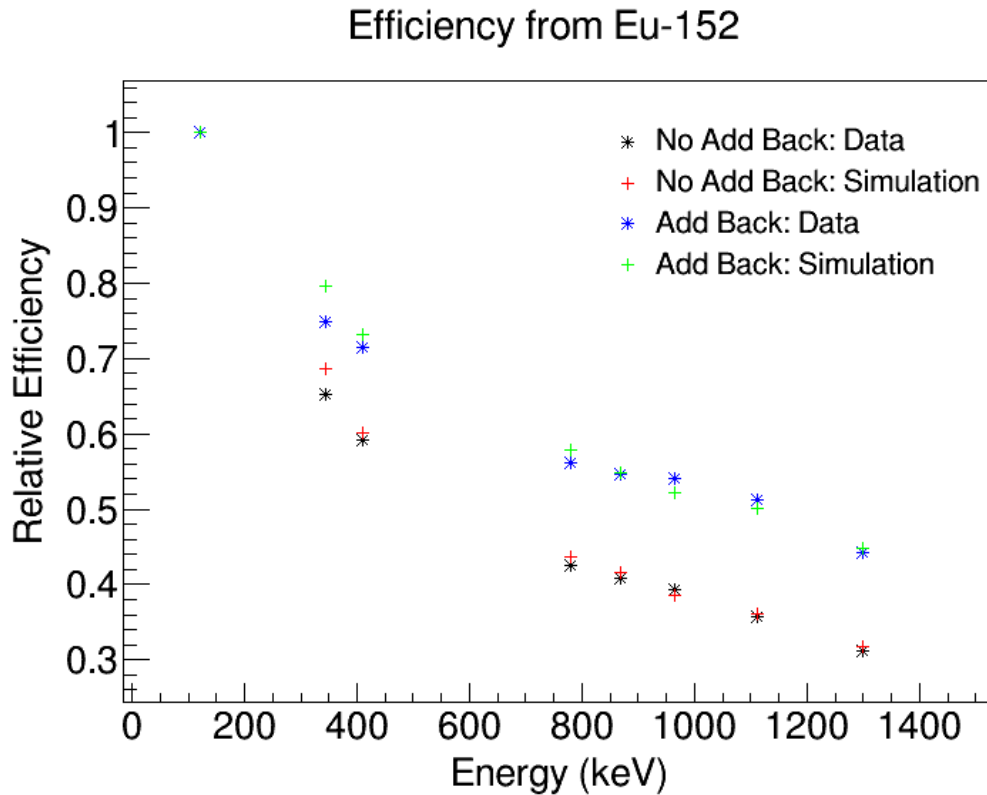


Figure 2.20: Comparing the efficiency of the simulated source run to the actual source run for both add back turned on and off.

The assumed level-scheme input into the simulation only included the 2_1^+ , 2_3^+ , and 4_1^+ levels. The energies of the levels are input into the simulation and adjusted such that the measured centroid from the simulation lines up with the measured centroid of the data to within 0.5 keV for each peak. The input centroids into the data are shown in Table 2.1. Notice that the transition energy extracted from the target-only data depends on the lifetime hypothesis of the 4^+ state. The input

Table 2.1: Centroids for States input into Simulation. The lifetime, τ , is varied only for the 4_1^+ state. Consequently, the input centroid for the 4_1^+ and the 2_1^+ states depends on the lifetime because long-lived states decay downstream of where they are produced, creating a difference in the angle for the Doppler-correction.

	2_3^+	951.3 keV	4_1^+	1133.1 keV	2_1^+	1320.6 keV
τ (ps)	Input (keV)	Measured(keV)	Input(keV)	Meas.(keV)	Input(keV)	Meas.(keV)
1.0	949.8	951.5	1132.0	1132.8	1320.9	1320.7
3.5	949.8	951.3	1133.1	1132.9	1320.9	1320.4
10	949.8	951.4	1134.6	1133.0	1321.3	1320.6
20	949.8	951.5	1136.8	1133.0	1321.8	1320.5
40	949.8	951.4	1140.1	1133.2	1322.3	1320.6
60	949.8	951.6	1142.4	1133.4	1322.8	1320.4
80	949.8	951.3	1145.5	1133.1	1322.8	1320.4
100	949.8	951.3	1148.0	1132.6	1322.8	1320.5
120	949.8	951.4	1150.0	1133.3	1322.8	1320.7

for the 2_3^+ level is constant for all lifetime hypotheses of the 4_1^+ state, but the inputs for the 4_1^+ and 2_1^+ states change as a function of the assumed 4_1^+ lifetime. This is due to the difference in Doppler shift between a state that decays immediately and one that decays downstream of where it is created. The difference in angle for states with different lifetimes is enough to change the detected γ ray energy. Once these inputs were fixed for the target-only run, they remained constant for the target-degrader runs.

The relative intensities of the level populations can be found in two ways. The first method is by using the efficiency curve shown in Figure 2.7. The area of each of the peaks is found and converted to a relative intensity. Since the 2_3^+ and the 4_1^+ feed the 2_1^+ , the intensities of the 2_3^+ and the 4_1^+ are subtracted from the 2_1^+ . These values are normalized to sum to 100 and are shown in Table 2.2.

The second way to determine the intensities relies on the simulation to adjust the level population. In this case, the relative ratio of the 2_3^+ to 4_1^+ was first found for a fixed 2_1^+ intensity. The intensity of direct populatin of the 2_1^+ state was fixed at 40% while the ratio of the 2_3^+ to 4_1^+ intensity was allowed to vary. The simulation is normalized to the $2_3^+ \rightarrow 2_1^+$ transition, so the χ^2 was found for the $4_1^+ \rightarrow 2_1^+$ transition. The χ^2 dependence on the ratio is shown in panel a of Figure 2.21. Once this value was fixed, the 2_1^+ intensity was varied. This χ^2 dependence on intensity is

shown in Panel b of Figure 2.21. The values used in the simulation are also tabulated in 2.2. As can be seen both methods of determining intensity are in good agreement with one another.

Using these energies and intensities just discussed, Figure 2.22 compares the simulation to the target-only data for an assumed lifetime of the 4_1^+ state of 3.5ps and 76ps. The χ^2 dependence for the target-only fits is shown in Figure 2.23. The lifetime of the 4_1^+ state is varied while the lifetimes of the 2_1^+ and 2_3^+ state are fixed at 3.0ps and 0.5ps respectively. As can be seen, both the $4_1^+ \rightarrow 2_1^+$ and the $2_1^+ \rightarrow 0_1^+$ transitions have better fits for longer lifetimes, while the $2_3^+ \rightarrow 2_1^+$ transition is independent of lifetime. Still, this target-only spectra does not provide convincing evidence of a delayed $4_1^+ \rightarrow 2_1^+$ transition. The energies and intensities determined here are set for the remainder of the analysis.

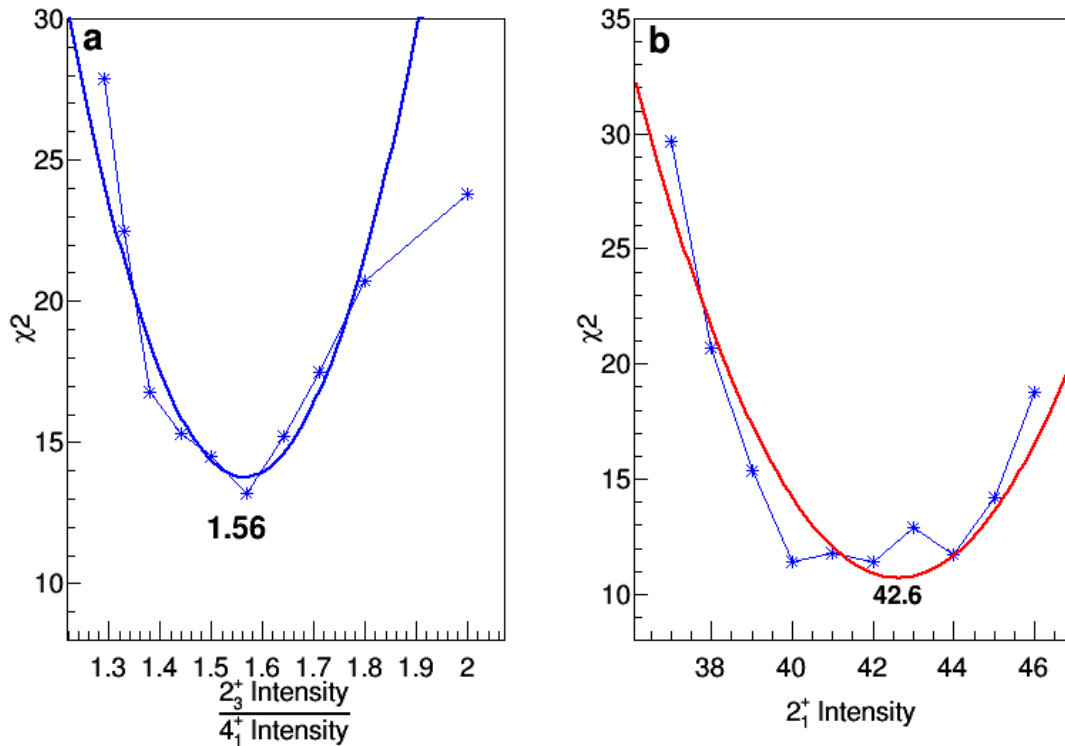


Figure 2.21: Determining the intensity of the 2_1^+ , 2_3^+ , and 4_1^+ using the simulation. In Panel a, the intensity of the 2_1^+ state is fixed while the ratio of the intensities of the 2_3^+ to 4_1^+ is allowed to vary. In Panel b, the ratio of the intensities of the 2_3^+ to 4_1^+ is fixed and the intensity of the 2_1^+ is allowed to vary.

Table 2.2: Intensities measured by using the data and by using the simulation. As can be seen, these two methods agree well with one another.

Level	Intensity (Data)	Intensity (Simulation)
2_1^+	40(2)	42.0(30)
2_3^+	36(2)	35.3(30)
4_1^+	24(2)	22.7(30)

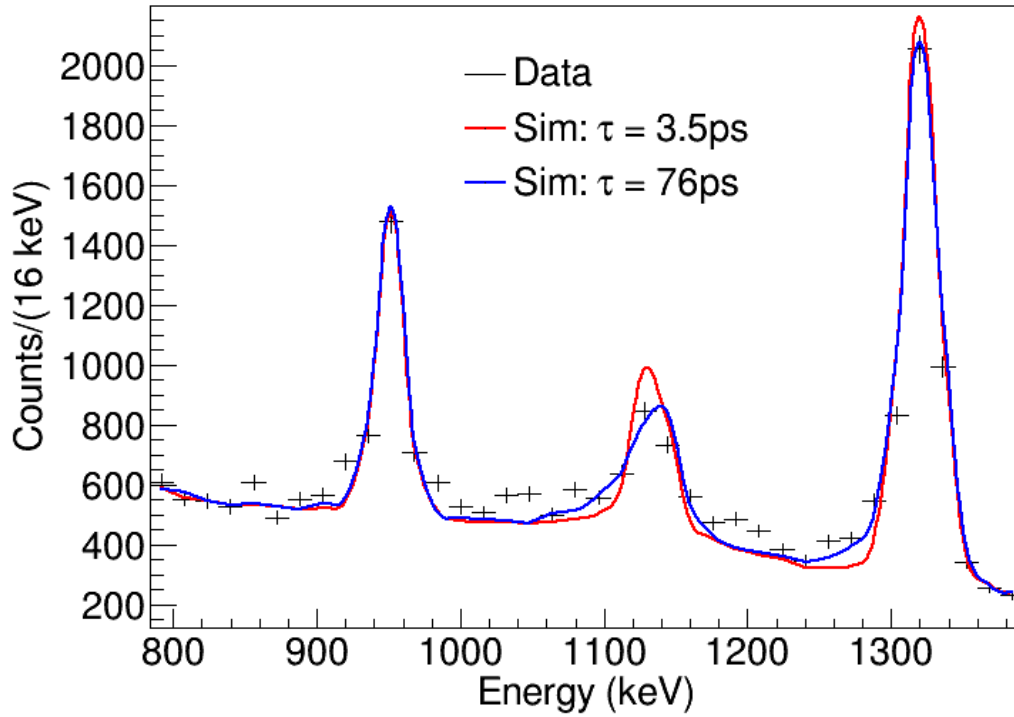


Figure 2.22: Comparing data to simulation for the adopted lifetime of the 4^+ and for a short lifetime. The target-only spectra is not very sensitive to the lifetime effect.

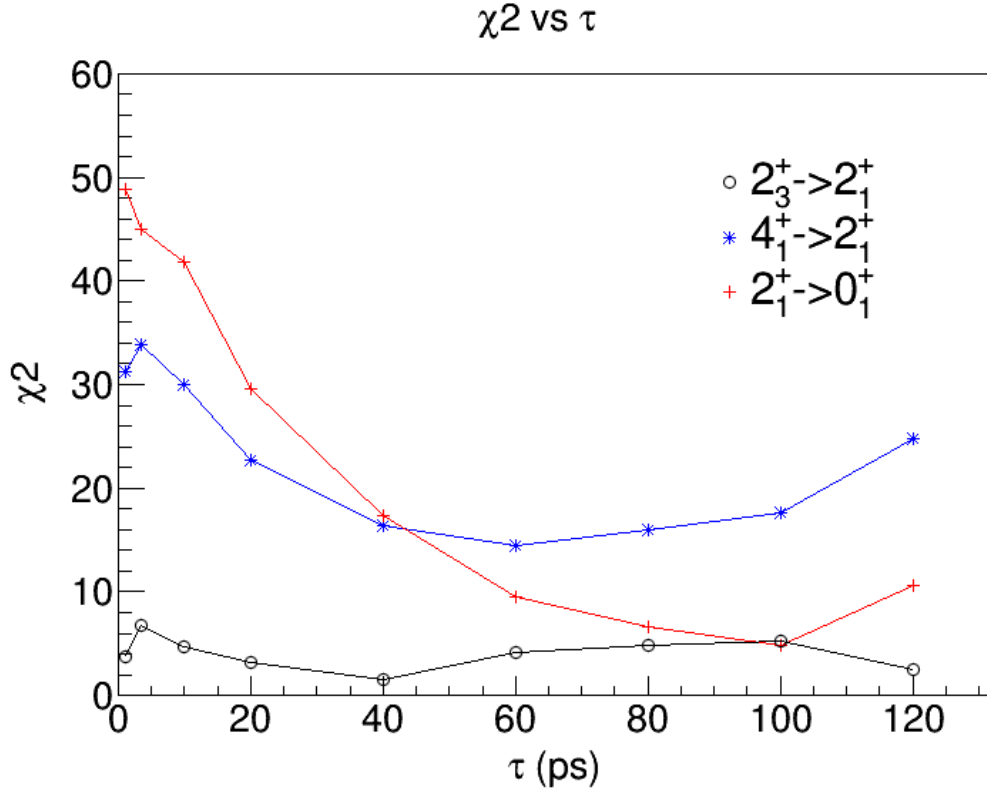


Figure 2.23: χ^2 dependence on τ . The lifetime of the 4_1^+ state is allowed to vary, while the lifetimes of the 2_1^+ and the 2_3^+ states are fixed. The $4_1^+ \rightarrow 2_1^+$ transition and the $2_1^+ \rightarrow 0_1^+$ transition both have better fits for long lifetimes, while the $2_3^+ \rightarrow 2_1^+$ transition shows no lifetime dependence. However, the target-only spectra is not very sensitive to the lifetime.

2.5.4 Long-Distance Runs

With the cross section on the target determined, the remaining parameter to be determined is the relative cross section for reactions induced on the degrader. Here, two factors enter our analysis: The total number of reactions induced on the degrader versus reactions induced on the target and the relative intensity of the three primary peaks. It is tempting to assume that the relative intensities of the states will be the same for degrader induced reactions versus target-induced reactions, but there is no reason why this has to be the case. The degrader is a much heavier elemental material than the target and that can lead to a different reaction mechanism that populates the states with different intensities. We take this possibility into account by allowing the

intensities of the states for degrader-induced reactions to vary and set these intensities using the long-distance data.

Different Intensities on Degraded-Induced Reactions. The feature allowing for different population of states on the degrader versus on the target was added to the simulation code by the author. To demonstrate that the simulation code is working correctly, a number of simulations was performed with just 2 γ rays in the spectrum. The target intensity was fixed for all runs, and the degrader intensity was varied from 10% to 90% for the lower energy transition. Figure 2.24 shows the simulated spectra for a few of these runs and the graph shows that the measured relative intensity is equivalent to the input intensity, a demonstration of the simulation's consistent results.

Only the $2_3^+ \rightarrow 2_1^+$, the $4_1^+ \rightarrow 2_1^+$, and the $2_1^+ \rightarrow 0_1^+$ transitions are included in the fit to the data. Each intensity of direct population is input into the simulation as a fraction out of 100 and the sum of the three intensities input into the simulation always equals 100. The target intensities are fixed, so the degrader intensities are determined by varying the input degrader intensities and by varying a global reaction ratio that gives the ratio of target-induced reactions to degrader-induced reactions: $R=T/D$. This can be parameterized in the following manner. The effective target-to-degrader ratio for a given state is equal to the global ratio times the ratio of the target intensity to the degrader intensity: $r_{eff} = R \cdot \frac{I_T}{I_D}$. To determine the effective ratio for a given transition, two of the transition ratios are fixed and the third is allowed to vary.

Determining Degraded Ratios with Long-Distance Run. With the formalism just discussed, the actual target-to-degrader ratio is determined in the following manner. In order to get the best statistics in the degrader peak, the full focal-plane acceptance of the S800 is used. Panel a of Figure 2.25 shows the long-distance data with the full focal-plane acceptance as well as a best fit simulation. These γ rays are Doppler corrected assuming emission from the target location. The target-to-degrader ratio for each of the three states is discussed below.

The ratio of the 1319 keV γ ray from the de-excitation of the 2_1^+ state depends on the ratio of the states feeding it, namely the 2_3^+ and the 4_1^+ . The degrader ratios of the 2_3^+ and the 4_1^+ only depend indirectly on the 2_3^+ ratio through the contribution of the Compton background, which does not have a large effect. The 2_3^+ ratio was fixed first assuming that the 4_1^+ ratio was 1.0 and the 2_1^+ ratio was 0.8. The 2_3^+ ratio was found by varying the assumed ratio between 0.6 and 1.2

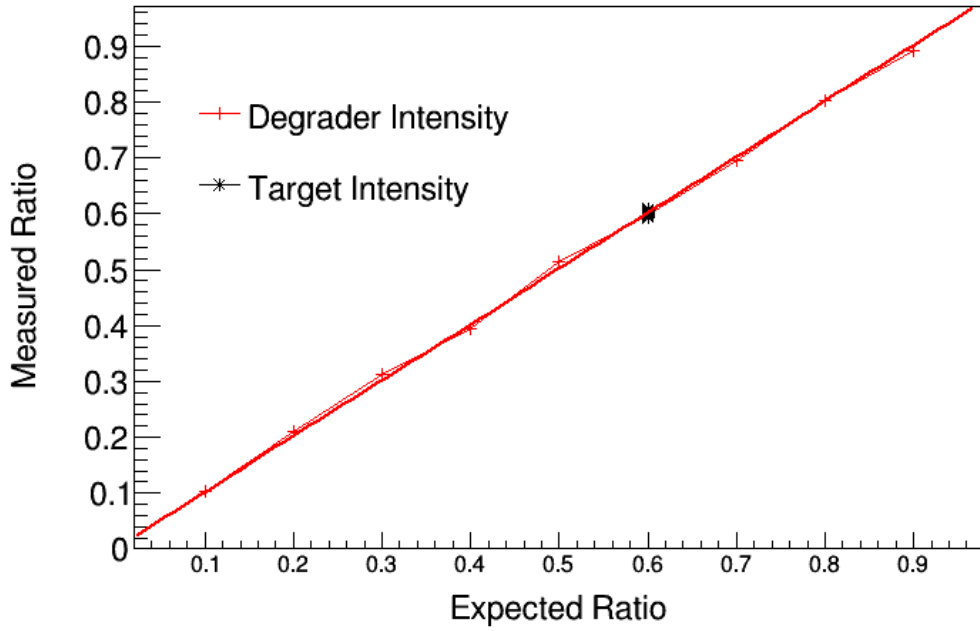
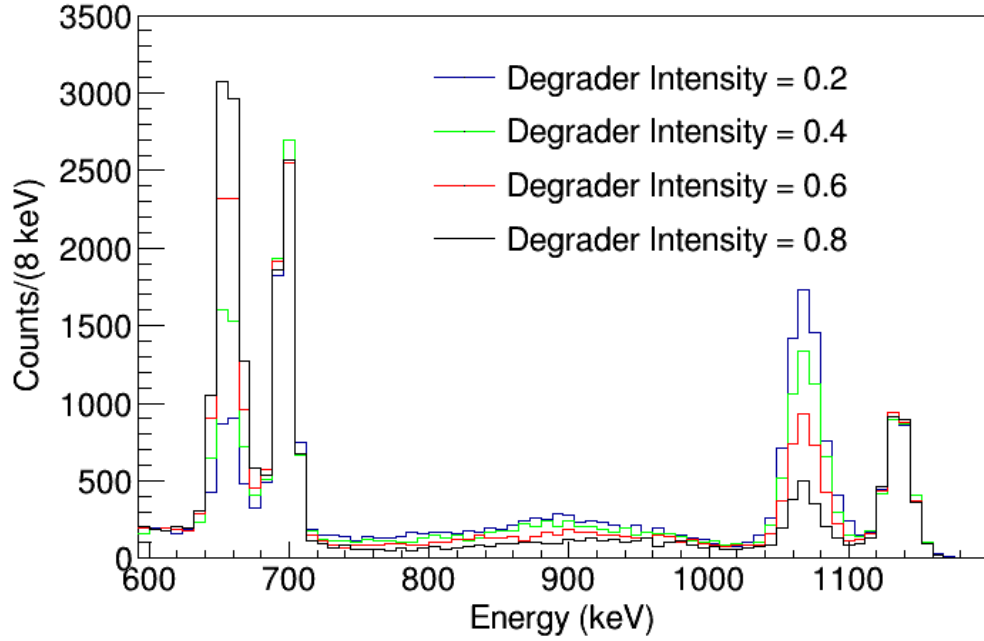


Figure 2.24: Demonstration of different intensities on degrader-induced reactions versus target-induced reactions. Panel a shows simulated spectra with different input degrader intensities and Panel b shows the measured ratio as a function of expected ratio.

and performing a χ^2 analysis. This χ^2 analysis is shown in Panel b of Figure 2.25. The ratio of the $2_3^+ \rightarrow 2_1^+$ transition was determined to be 0.85(10) and was fixed for the remainder of the analysis.

Because of the correlated line-shapes of transitions emitted in cascade, the ratio of the 4_1^+ and the 2_1^+ states were determined in a more complicated way. The ratio of the 4_1^+ state was allowed to vary between 0.6 and 1.4. For each of these assumed ratios, the 2_1^+ ratio was allowed to vary. Panel b of Figure 2.25 shows the 2_1^+ ratio assuming that the 4_1^+ ratio was 1.0. However, a similar χ^2 plot was created for all other assumed 4_1^+ ratios. For a 4_1^+ ratio of 1.4, the 2_1^+ ratio was found to be 0.96 and for a 4_1^+ ratio of 0.6, the 2_1^+ ratio was found to be 1.17. The adopted degrader ratio for the 2_1^+ state was found to be 1.05.

As just discussed, a number of simulations were run for each assumed 4_1^+ ratio, with the only difference being the assumed 2_1^+ ratio. The χ^2 values for the 4_1^+ ratio were taken from the same runs as the best fit 2_1^+ ratio. The best degrader ratio for the 4_1^+ state was determined to be 1.05(20) as shown in Panel b of Figure 2.25.

In the 25mm run, the full focal-plane is used to measure the degrader contribution because this provides the best statistics. However, for the short-distance runs, the higher-momentum half of the focal plane is used to selectively reduce the degrader components such that the target-based events are enhanced which provides a better sensitivity to the lifetime effect. Figure 2.26 shows a comparison between using the full focal-plane and half of the focal-plane in determining the ratio. The simulated spectra in both panels are created using the exact same inputs into the simulation, with an assumed target-to-degrader ratio of 1.0 for both the 4_1^+ and 2_1^+ transitions. Panel a shows both the data and simulation cut on the higher momentum side of the focal-plane, Panel b shows the data and simulation with no focal-plane cut, and Panel c shows the χ^2 analysis as a function of $2_1^+ \rightarrow 0_1^+$ ratio for both of these situations. As can be seen, the determined ratio is in good agreement in both cases.

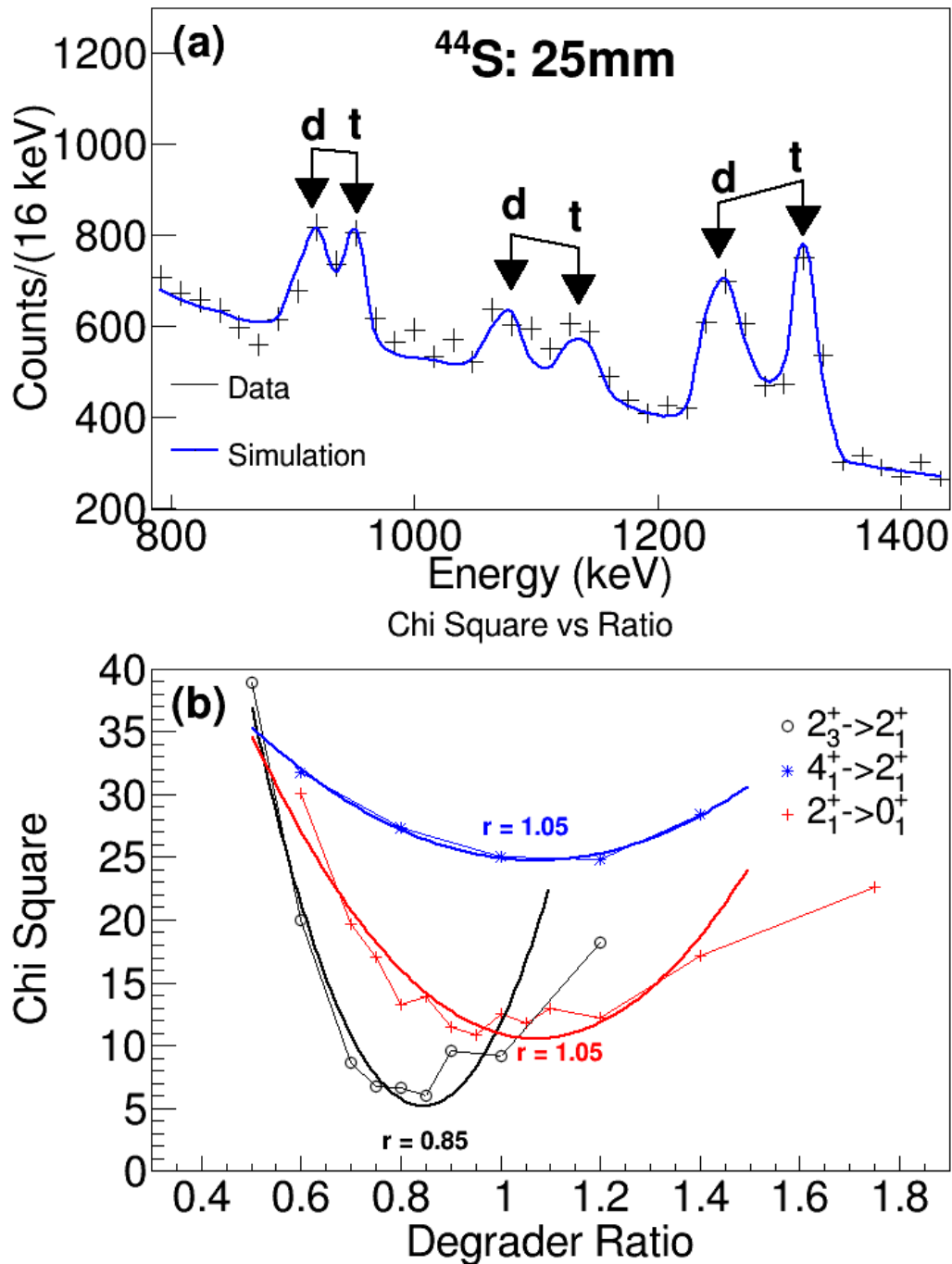


Figure 2.25: γ ray spectrum recorded for the target-degrader distance 25 mm, in coincidence with ^{44}S reaction residues (Panel a). For each γ transition, two peaks are observed, one for target-induced reactions (labeled “t”), and one for degrader-induced reactions (labeled “d”). The simulated spectra were used to determine the ratio of reactions induced by the degrader. The χ^2 dependence on target-to-degrader reaction ratio is shown in Panel b.

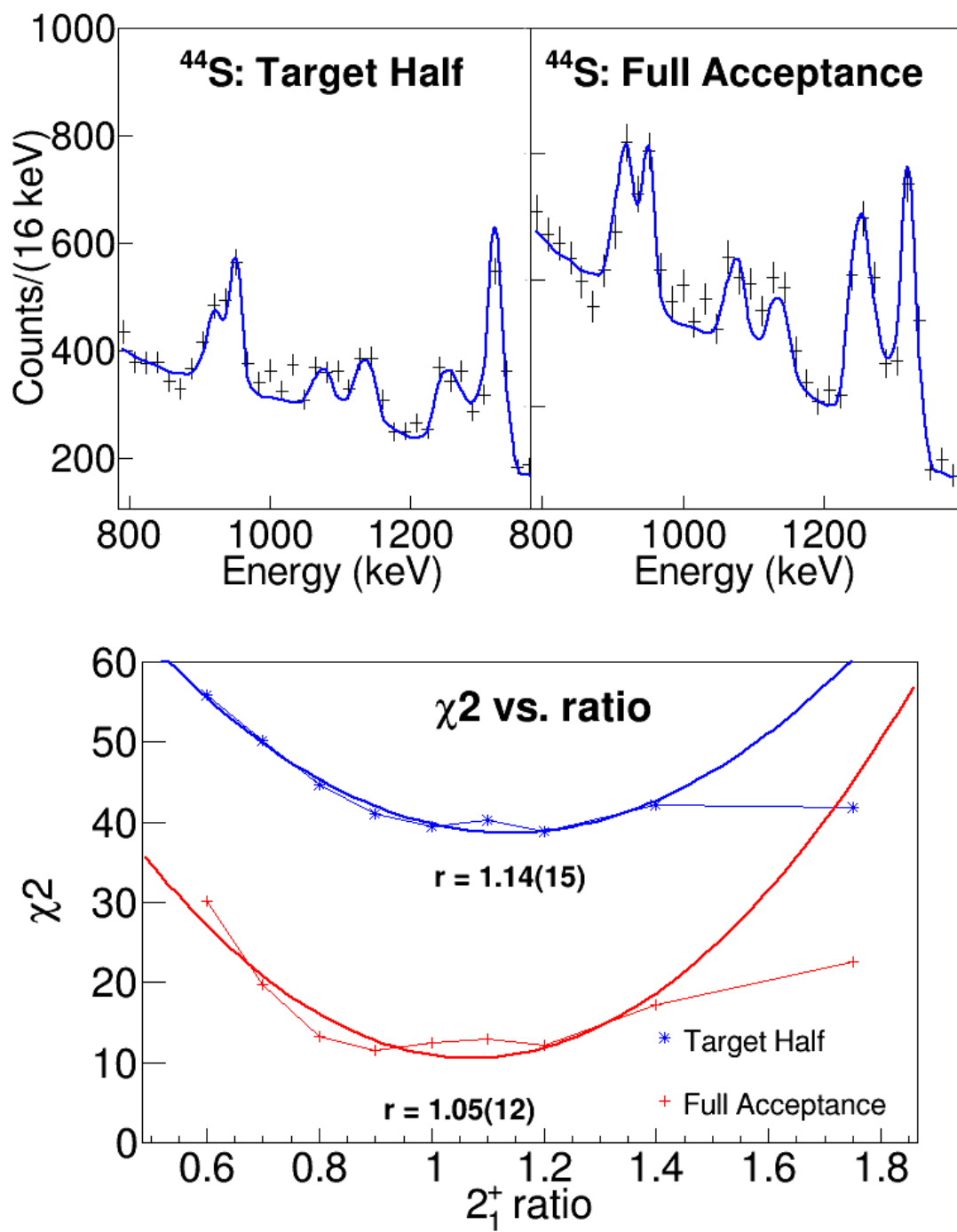


Figure 2.26: Scaling from full S800 acceptance to half S800 acceptance (see text).

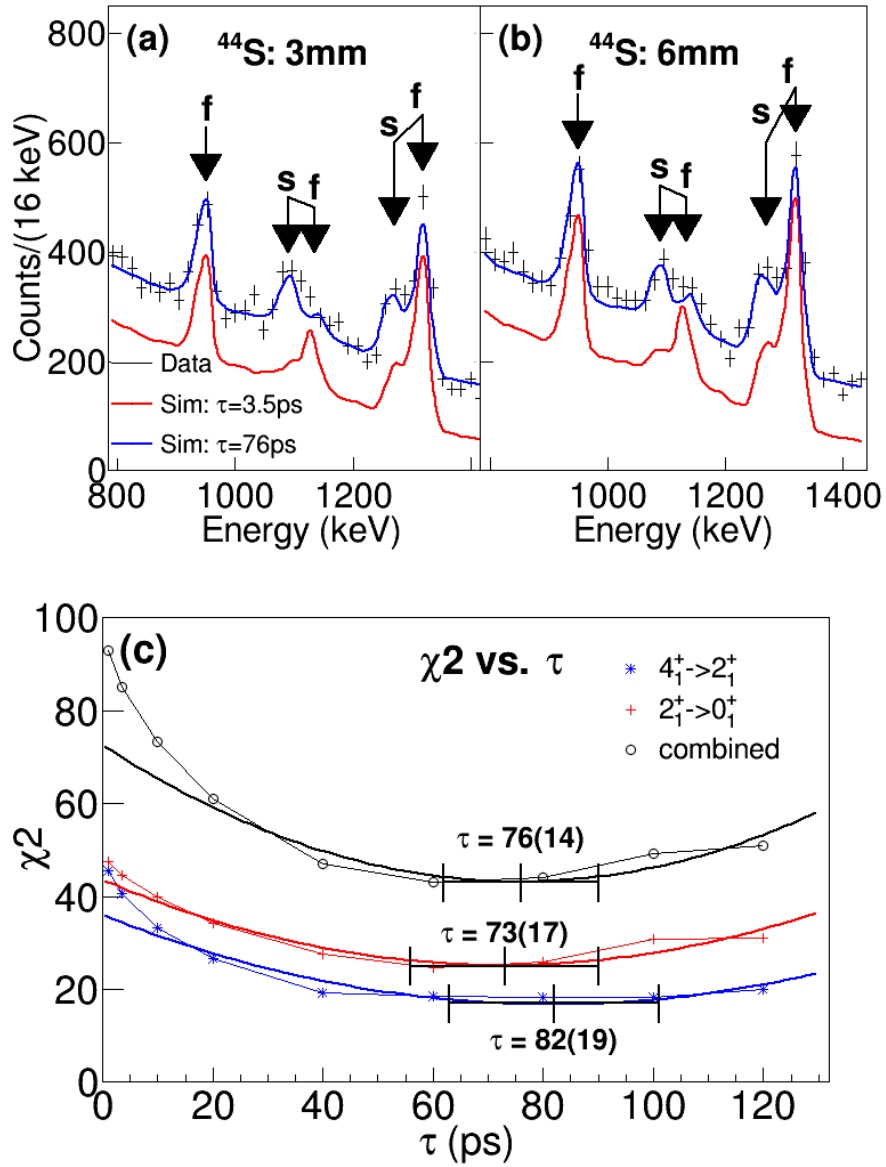


Figure 2.27: γ ray spectra observed in coincidence with ^{44}S , recorded with the target-degrader distance set to 3mm (Panel a) and set to 6mm (Panel b). The spectra are compared to a Monte-Carlo simulation for the adopted lifetime of the 4^+ state (76ps) and, for comparison and vertical offset, a short lifetime of 3.5ps. The 949 keV peak shows characteristics of a prompt emission, while the 1140 keV peak shows characteristics of a long lifetime. The spectra were fit using a Monte-Carlo simulation (see text). The χ^2 dependence on lifetime is shown in Panel c.

2.5.5 Determining the Lifetime with the Short-Distance Runs

With the degrader ratios determined as just discussed, the short-distance runs are used to determine the lifetime. The spectra for the 3 mm and 6 mm runs are shown in Panels a and b of Figure 2.27. Here, the upper half of the residue momenta detected in the S800 spectrograph is selected, creating an enhancement of the target-induced events and the RDM effects in the data.

A χ^2 analysis testing the 3 mm and 6 mm spectra against the respective Monte-Carlo simulations over a range of hypothetical lifetimes for the 4^+ is discussed, which provided a value of $76(14)_{\text{stat}}(20)_{\text{sys}}$ ps at a reduced $\chi^2 = 2.7$. This χ^2 analysis is shown in Panel c of Figure 2.27. Note that a lifetime effect is seen in the χ^2 dependence in both the 1140 keV peak and in the 1319 keV peak. The dependence of the 1319 keV peak on the lifetime enters indirectly through the feeding from the 4^+ .

The best fit to the data is shown in Panels a and b of Figure 2.27. In addition, a fit to the data assuming a 3.5 ps lifetime is shown for comparison. The simulation shows the main features of the data discussed earlier. The line-shape of the $2_3^+ \rightarrow 2_1^+$ transition at 949 keV is fit very well with an assumed lifetime of 0.5ps. Again there is no slow component seen in the $2_3^+ \rightarrow 2_1^+$ transition. The 1140 keV line, identified with the $4_1^+ \rightarrow 2_1^+$ transition, exhibits a lifetime effect, where the majority of the peak is found in the slow component in both the 3mm and 6mm distances. Notice that in the fast lifetime hypothesis, the majority of the $4_1^+ \rightarrow 2_1^+$ transition is at the correct γ ray energy, with a small shoulder corresponding to the degrader-induced reactions. As discussed before, the delayed character of the $4_1^+ \rightarrow 2_1^+$ transition also leads to a delayed emission of the 1319 keV $2_1^+ \rightarrow 0_1^+$ transition in cascade. The $2_1^+ \rightarrow 0_1^+$ transition by itself shows a line-shape similar to that seen in the 3.5ps hypothesis shown in the figure. The delayed lifetime of the 4_1^+ is necessary in the feeding to fully reproduce the observed line-shape of the $2_1^+ \rightarrow 0_1^+$ transition. This observed line-shape, reproduced by the simulation, is further confirmation for the placement of the 1140 keV transition as populating the 2_1^+ .

The systematic uncertainty in the lifetime is estimated by allowing a different relative yield for the 4_1^+ state in the degrader-induced reactions. Figure 2.28 shows the lifetime determination assuming a 4_1^+ target-to-degrader ratio of 0.8. With a ratio of 0.8 for the $4_1^+ \rightarrow 2_1^+$ transition, the lifetime was determined to be 56 ps. This suggests a systematic error due to the degrader ratio of ± 20 ps. This simulation, with an assumed lifetime of 56ps for the 4^+ , is shown in Figure

2.28. Additionally, the simulation with a short lifetime hypothesis is shown in comparison. The qualitative features of the simulation are the same as just discussed, with both the $4_1^+ \rightarrow 2_1^+$ and the $2_1^+ \rightarrow 0_1^+$ transitions showing the lifetime effect. Now the determined lifetime is shorter, because more reactions are assumed to happen on the degrader.

Reduced Transition Probability. The reduced transition probability ($B(E2)$) is given experimentally by equations 2.6 and 2.7[28]. Equation 2.6 is in terms of $e^2\text{fm}^4$ while equation 2.7 gives the single particle estimate in terms of W.u. Using these equations, the deduced lifetime for the 4^+ state corresponds to a reduced matrix element for the 1140 keV transition of $B(E2:4_1^+ \rightarrow 2_1^+) = 5.6(18) e^2\text{fm}^4$ or $0.61(19)$ W.u.

$$B(E2) = \frac{\tau}{1.223 * 10^9 E^5} \quad (2.6)$$

$$B_{s.p.}(E2) = 0.0594A^{4/3} \quad (2.7)$$

2.5.6 Establishing the Methodology with ^{42}S

Large quantities of ^{42}S was observed in this experiment. The lifetime of the first 2_1^+ state in ^{42}S has been established through Coulomb excitation [29] and it is used here as an independent verification of our analysis.

The lifetime of ^{42}S is determined in an analogous way to that of ^{44}S . The 25mm run was used to determine how many reactions occurred on the degrader. This data is displayed in Figure 2.29, along with a best fit from the simulation. Just as with ^{44}S , the events were selected for laboratory γ -angles below 45° and were Doppler corrected assuming emission from the target position. The ^{42}S data exists on the edge of the S800 acceptance, which suppresses the degrader-induced reactions.

The simulated spectra for this distance were used to extract the relative probability of reactions induced by the degrader over the total number of reactions. In the simulation, the variable parameter is the number of target-induced reactions divided by the number of degrader-induced reactions. This parameter was allowed to vary and a χ^2 analysis was performed. Panel b of Figure 2.29 shows the χ^2 fit to the data. The degrader ratio was determined to be $1.3(1)$. In other words, 43% of all reactions were induced by the degrader.

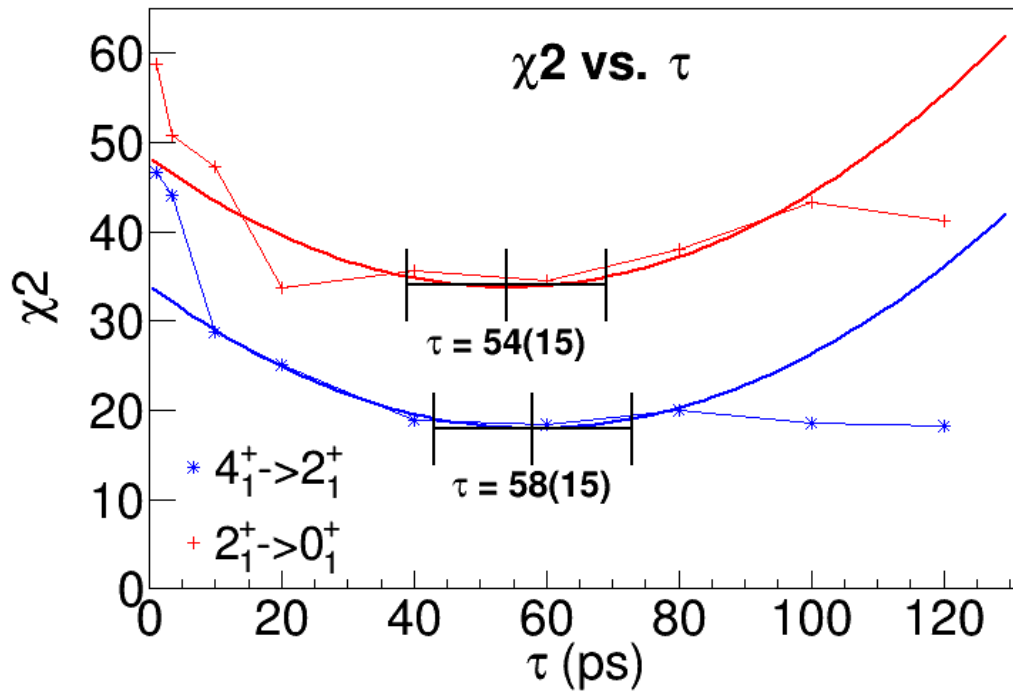
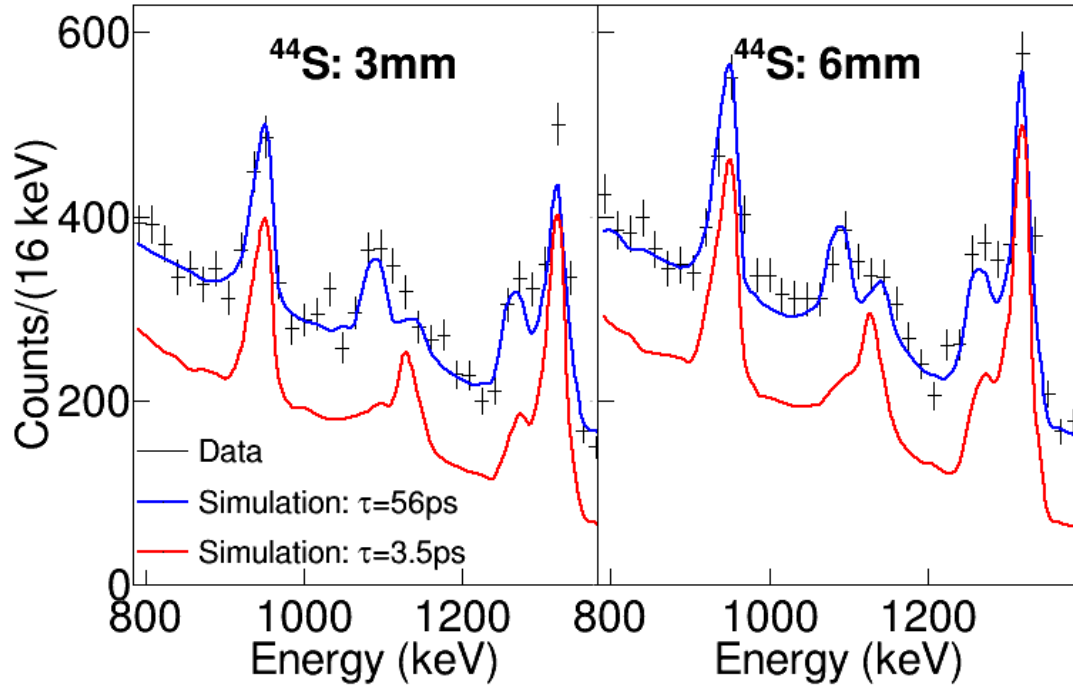


Figure 2.28: γ ray spectra observed in coincidence with ^{44}S , recorded with the target-degrader distance set to 3mm (Panel a) and set to 6mm (Panel b). Here the assumed 4_1^+ ratio was 0.8 causing the determined simulated lifetime to be shorter. A systematic error of $\pm 20\text{ps}$ was adopted.

In Fig.2.30, the ^{42}S data from the 3 mm and 6 mm runs is shown, again selected for laboratory γ ray angles below 45° and Doppler corrected for emission from the target position. The γ -peaks observed at the correct energies are marked as ‘f’ for “fast” reaction residues, while those shifted to lower energies are marked with an ‘s’ for “slow”. The intensity ratios between the “fast” and “slow” peaks and the change observed between the distances are an effect of the 2_1^+ states’ lifetime. The simulated spectrum of the peak region was compared to the experimental spectrum through a χ^2 analysis, from which a lifetime value of 20.6 ps with a statistical uncertainty of 1.5 ps was extracted, consistent with the Coulomb-excitation value 18.5(33) ps from Ref. [29]. This χ^2 analysis is shown in Panel c of Figure 2.30.

2.6 Discussion

The experimental observation of an isomeric 4_1^+ state can be discussed in terms of various theoretical frameworks. The first framework looks at the nucleus from a microscopic perspective, using detailed shell model calculations to discuss the n particle-n hole (np-nh) excitations. The second framework treats the nucleus from a more collective model, looking at the overall wavefunction and describing the geometry of the nucleus. Although these frameworks describe the nucleus in different terms, they should come to qualitative agreement. I will introduce some conceptual ideas before explicitly discussing their application in ^{44}S .

2.6.1 The Shell Model

It is an experimental fact of nuclear physics that nuclei with certain “magic” numbers of protons and neutrons exhibit special properties. Nuclei which have 2,8,20,28,50,82, or 126 neutrons or protons are more bound than the surrounding nuclei. These magic numbers arise naturally out of confining nucleons to move in a central potential. A typical ordering of nuclear levels is shown in Figure 2.31. The levels are identified by the principle quantum number, n, the orbital angular momentum, l, and the total angular momentum, $j=l\pm 1/2$. For instance, the level $1p_{3/2}$ has $n=1$, $l=p=1$, and $j=3/2$. A total of $2j+1$ particles can be in a particular orbit, distinguished by their orientation onto a particular axis, given by “m”. These magnetic projections are degenerate for a spherical symmetry.

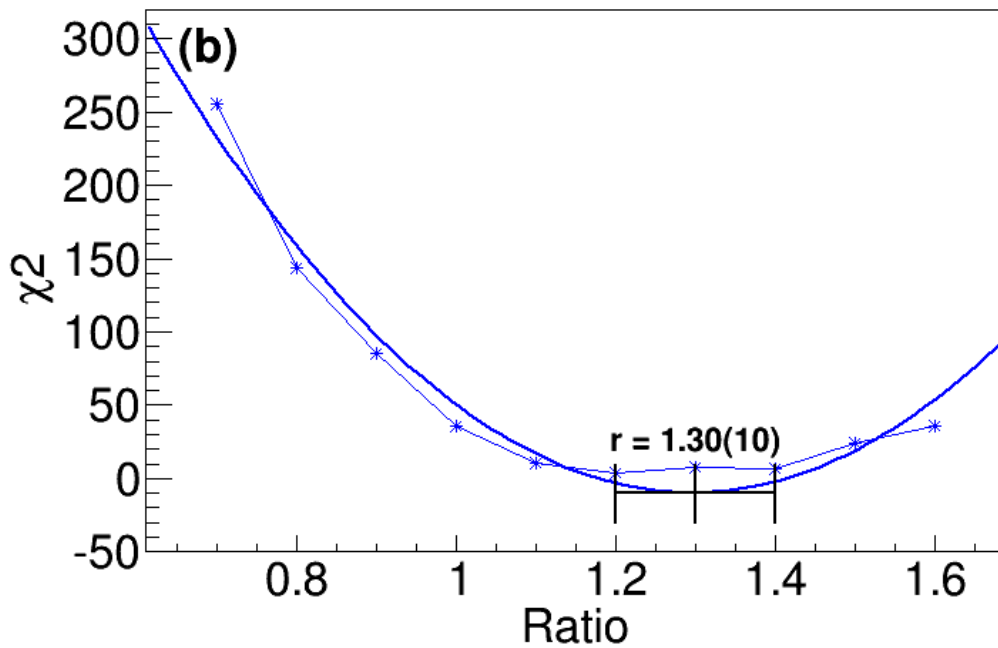
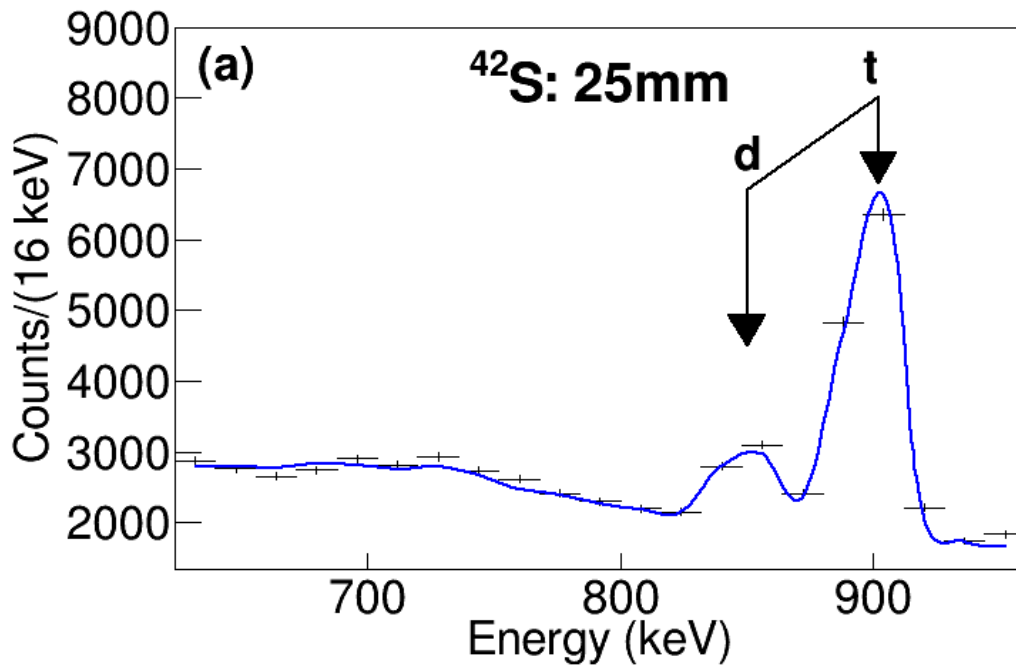


Figure 2.29: γ ray spectrum recorded for the target-degrader distance 25 mm, in coincidence with ^{42}S reaction residues (Panel a). For each γ -transition, two peaks are observed, one for target-induced reactions (labeled “t”), and one for degrader-induced reactions (labeled “d”). The simulated spectra were used to determine the ratio of reactions induced by the degrader. The χ^2 dependence on target-to-degrader reaction ratio is shown in Panel b.

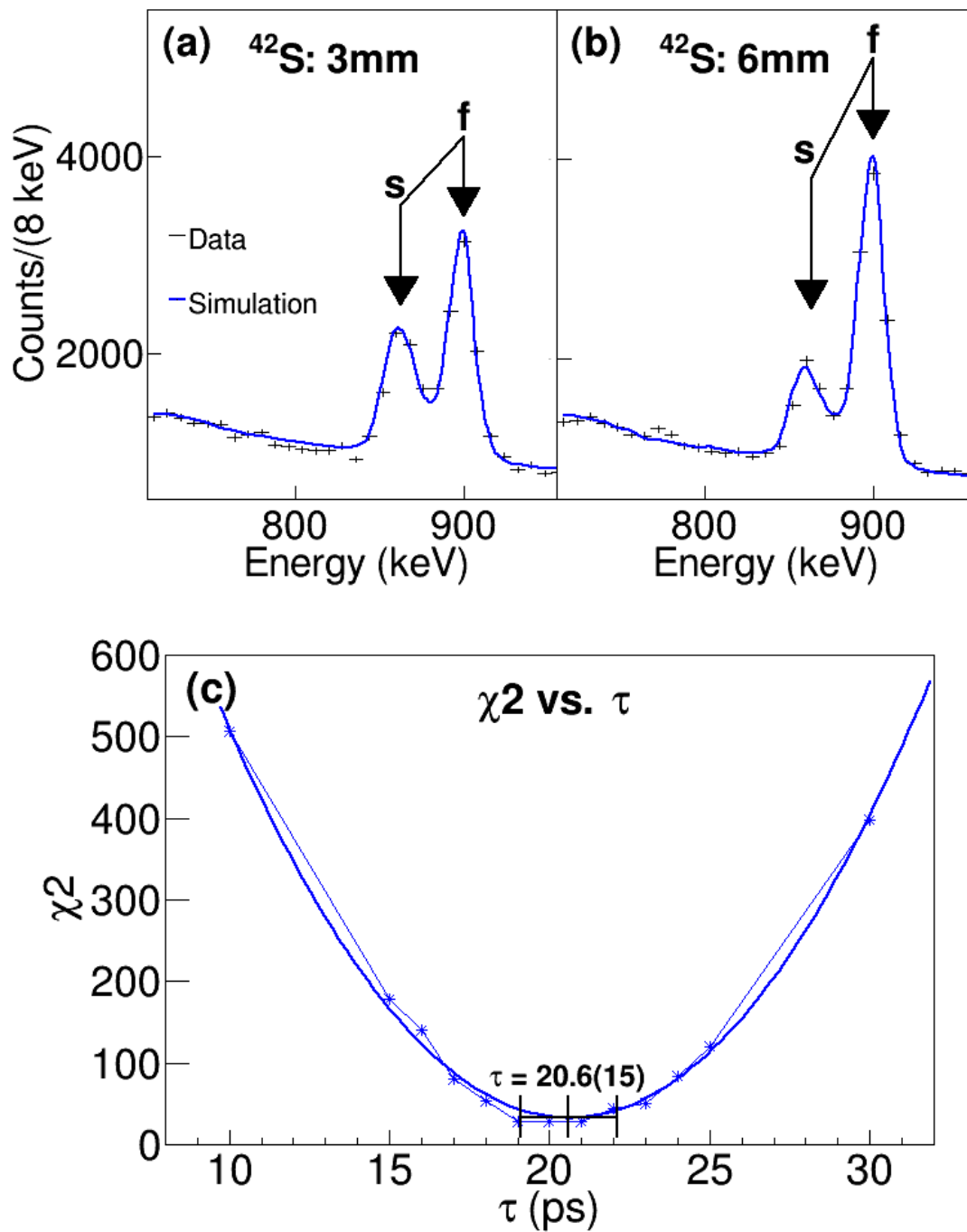


Figure 2.30: γ ray spectra observed in coincidence with ^{42}S , recorded with the target-degrader distance set to 3 mm (Panel a) and set to 6 mm (Panel b). The relative change in intensities in the fast and slow peaks from 3 mm to 6 mm is an effect of the state's lifetime. The spectra were fit using a Monte-Carlo simulation (see text). The χ^2 dependence on lifetime is shown in Panel c.

Modern shell-model calculations treat the nucleons moving in a central potential and include all of the possible two body correlations between valence particles. Two similar interactions are discussed in this work: the sd-pf-u interaction based on the work by Nowacki and Poves [30], and the sd-pf-mu interaction based on the work by Utsuno et al.[31]. Both of these interactions include the entire sd-pf shell. In other words, the ^{16}O core (8 protons and 8 neutrons) is fixed and the remaining nucleons are allowed to interact in the sd and pf shells. For ^{44}S , the protons are entirely in the sd shell and the neutrons are in the pf shell. These Hamiltonians allow three types of interactions: proton-proton, neutron-neutron, and neutron-proton. The differences in the two models depend mostly on the choice of effective interaction used. The sd-pf-u interaction parameterizes the interaction and determines the strength by a fit to experimental data[30]. The sd-pf-mu interaction, in contrast, assumes the form of the interaction must be a central potential plus a tensor component and it calculates all of the matrix elements[31].

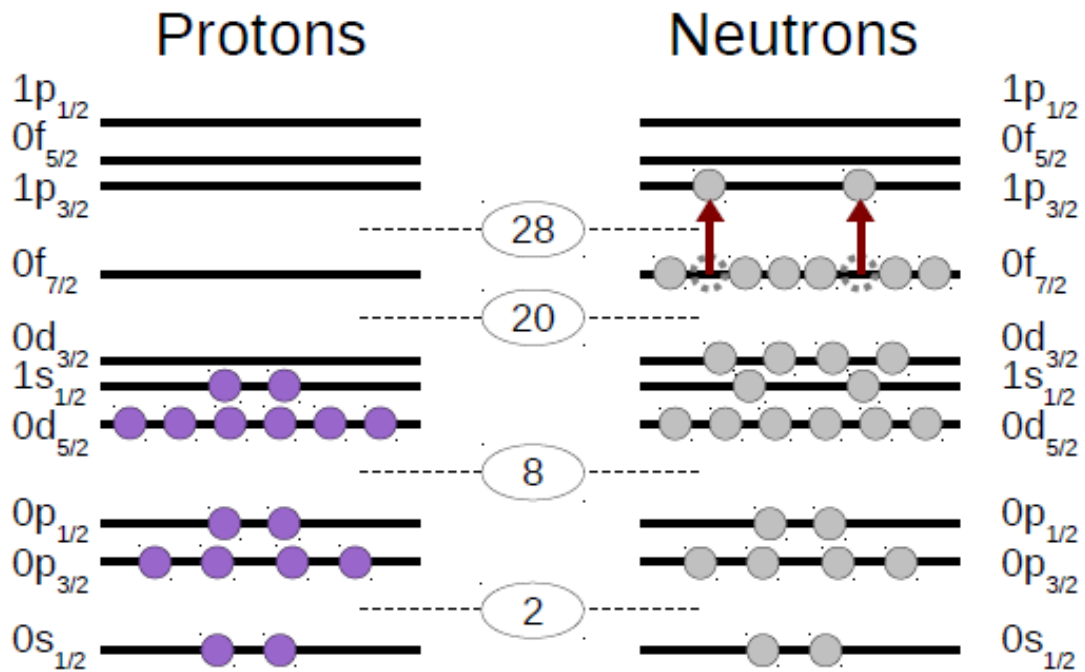


Figure 2.31: The ordering of nuclear levels for ^{44}S . The levels are filled in with the protons and neutrons. The neutrons completely fill the $f_{7/2}$ level. Figure taken from the dissertation by Daniel Santiago-Gonzalez[8].

These shell model calculations can be interpreted in terms of their basis states. The basis

states are many body wavefunctions which are anti-symmetrized products of the single particle wave functions[28]. In many cases, these wavefunctions are dominated by a few configurations. It is convenient to discuss these wavefunctions in terms of particle-hole excitations. For instance, a wavefunction may be comprised mostly of the many-body state that has two neutrons promoted to the $p_{3/2}$ level. In this case, we refer to this as a two-particle-two-hole (2p-2h) excitation.

2.6.2 Rotational Motion

Often times, the complex interactions in the shell model give rise to nuclei with deformed shapes. For certain nuclei, a simplification to the shell model can be made by assuming a deformed central potential and considering the symmetries of the wavefunction. Rotations can be described mathematically by separating the rotation into rotations about a body-fixed axis and rotations about a space fixed axis. In the intrinsic frame, rotating nuclei can be described by their shapes. A classical picture of nuclear deformations has the nuclear shape ranging from a prolate (American football) to an oblate (Frisbee) shape. In between these two shapes are deformations that have no axial symmetry (triaxial). The deformation coordinates are generally represented on a (β, γ) plane. β represents the extent of quadrupole deformation and γ represents the amount of axial asymmetry. A typical convention has prolate shapes corresponding to values of $\beta > 0^0$ and $\gamma = 0^0$, and oblate shapes corresponding to values of $\beta < 0^0$ and $\gamma = 60^0$ [32].

In the case of a deformed nucleus, the rotational symmetry breaks down in the intrinsic frame and the m substates are no longer degenerate. Under the assumption of axial symmetry, a new quantum number, K, appears. K is the projection of the angular momentum onto the symmetry axis. K is two fold degenerate, corresponding to rotations in either direction around the deformed nucleus. This quantum number is illustrated in Figure 2.32[9].

The full rotational spectra for a nucleus can be obtained by taking the vector sum of the intrinsic rotation with the space-fixed rotation. Adding these two rotations gives rotational bands built upon a particular K projection. For instance a K=0 band will have states with total spins of 0^+ , 2^+ , 4^+ , etc. built on top of it. Likewise, a K=4 band will have states with 4^+ , 5^+ , 6^+ , etc. built on top of it. Notice that states of the same angular momentum can belong to different K bands. This information is important in understanding K-isomerism. For a nucleus to decay from one state to another, the change in spin must be greater than or equal to the change in K[32]. If no transitions meet this condition, then the decay will be hindered, creating a K-isomer.

The rotational motion about the intrinsic frame is never completely separated from the rotational motion in the laboratory frame. These two rotations interact via the Coriolis interaction. If the frequency of rotation about the intrinsic frame is much larger than the rotation of the system in the laboratory frame, then this interaction can be ignored[32]. If they are comparable, then the Coriolis interaction will break the two-fold degeneracy in K because the Coriolis interaction depends on the direction of the rotating nucleon. This breaking of the degeneracy is equivalent to saying that time-reversal symmetry is broken in this system.

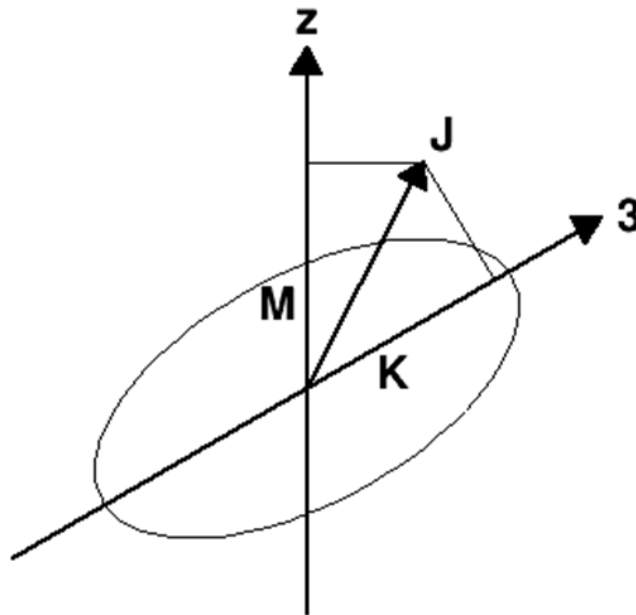


Figure 2.32: Rotational motion can be separated into rotations about a space fixed axis and rotations about a body fixed axis. The projection of the angular momentum onto the body fixed axis is referred to as K and is conserved for axially symmetric nuclei[9]

2.6.3 Theoretical Works

The deduced lifetime for the 4^+ state corresponds to a reduced matrix element for the 1140 keV transition of $B(E2:4_1^+ \rightarrow 2_1^+) = 5.6(18) e^2\text{fm}^4$ or $0.61(19) \text{ W.u.}$ For comparison, the ground state transition matrix element $B(E2:2_1^+ \rightarrow 0_1^+) = 63(18) e^2\text{fm}^4$ [18] corresponds to $7(2)$ single-particle or Weisskopf units (W.u.), which is indicative of moderate collectivity. In almost all even-even nuclei, the 4_1^+ state is a quadrupole excitation built on the lowest 2^+ . For ^{44}S , all theoretical studies predict such a collective rotational 4^+ state to exist and to decay with a much larger

$B(E2; 4_1^+ \rightarrow 2_1^+)$ transition matrix element of values varying between 9.1 [33] and 13.5 W.u. [34]. The deduced value of 0.61(19) W.u. for the decay of the observed 4^+ state is evidence that this state is not a member of the ground-state rotational band, confirming the hypothesis put forth by Santiago-Gonzalez et al.[4]. The hindered $B(E2)$ value also means that the 4^+ at 2459 keV shows very little mixing with the rotational 4^+ state-which is so far unobserved, but must exist-and which is predicted by theoretical studies to lie within 250 keV of the observed 4^+ .

Santiago-Gonzalez et al.[4] suggested the possible isomeric nature of this state in 2011. This suggestion was later affirmed by other shell model calculations such as those by Chevrier and Gaudefroy [35] and by Utsuno et al[31]. However, different theoretical approaches were taken that did not come to the same conclusions. A beyond-mean-field (bmf) calculation by Rodriguez and Egido [36] predicted a conventional rotational band in ^{44}S , where the lowest 4^+ was strongly connected to the 2_1^+ state. The state in Rodriguez and Egido's calculation that is most similar to the 4^+ state from the shell model calculations appears at 5.4 MeV[36]. Since then, the authors have updated their work to allow for the relaxation of time-reversal symmetry. A new work by Egido, Borrajo, and Rodriguez[34] is in good qualitative agreement with the shell model results and the experimental results. The current lifetime measurement helps distinguish between these nuclear models and provides a new benchmark for the models.

Although these theoretical calculations have converged onto qualitative agreement, they are still somewhat lacking in presenting a clear intuitive picture that explains the isomerism of this 4^+ state. The many-body states of the shell model wavefunctions can be projected onto particle-hole type states. The shell model calculations agree that the rotational band is built upon a 2p-2h neutron configuration, illustrated in Figure 2.31, while the observed 4^+ state is built upon a 1p-1h configuration. The fact that these states are built upon different configurations can lead to a hindered transition. Santiago-Gonzalez et al. [4] tried to take this description a step farther and discuss the 4^+ state in terms of K isomerism. If the 4^+ state is based upon a $K=4$ intrinsic wave function, then the transition to the 2_1^+ ($K=0$) state would be hindered by the K selection rules. This description was questioned by Chevrier and Gaudefroy[35] who used the existence of a $J=3^+$ state in the shell model calculations to suggest that if any K quantum number would be assigned to the state, it should be $K=3$. The shell model calculations do not explicitly give K quantum numbers, so this disagreement cannot be resolved within these calculations.

To investigate the symmetries of the intrinsic wavefunctions more deeply, a number of beyond-mean-field calculations have been performed. A recent theoretical work by Utsuno et al. [33] described the isomerism of the 4^+ state in terms of K-isomers. Utsuno et al. analyzed the shell-model wave functions in the intrinsic frame of reference by means of a variation after angular-momentum projection (AM-VAP) method and found that the 4_1^+ state is dominated by an almost pure (93%) $K = 4$ configuration, while showing a maximally triaxial shape with $\gamma = 28^\circ$ and moderate quadrupole deformation $\beta_2 = 0.23$ [33]. This almost pure $K=4$ configuration is counter-intuitive because this calculation explicitly breaks time-reversal symmetry and predicts the 4^+ to be triaxial, both cases in which the K quantum number is no longer good. However, Utsuno et al.[33] claim that the purity of K is approximately restored after diagonalizing the Hamiltonian in K space. Schematically, they described the $K=4$ configuration by fixing the ^{42}S core and taking into account two particle degrees of freedom. The $K=4$ configuration can be created by coupling one particle with spin $1/2$ with another particle of spin $7/2$. If these two particles aligned, a $K=4$ configuration is created. A $K=3$ configuration can be created by anti-aligning the spin of the $1/2$ with respect to the $7/2$. Specifically, this work predicts a decay matrix element of $0.1 e^2 \text{ fm}^4$ [33], smaller than the value obtained in our experiment, but in agreement with the isomeric nature of the state.

A separate beyond-mean-field calculation was carried out by Egido, Borrajo and Rodriguez [34]. As stated earlier, this work was an improvement on an earlier work by Rodriguez and Egido [36] which predicted a conventional, deformed level structure with the lowest observed 4^+ as part of a rotational band of prolate deformation. The older work by Rodriguez and Egido [36] was based on a symmetry conserving configuration mixing (SCCM) method that used the Gogny D1S interaction. This work conserved both spatial parity and time-reversal symmetry. However, it failed to predict the isomeric nature of the 4^+ state. The new work by Egido, Borrajo and Rodriguez has improved upon their theory by explicitly breaking time reversal symmetry [34]. They do this by coupling np - nh excitations to non-zero cranking frequencies. Additionally, they extend γ from $-60^\circ < \gamma < 120^\circ$ instead of the usual $0^\circ < \gamma < 60^\circ$. This extension of γ is necessary because of the breaking of time-reversal symmetry. The explicit breaking of time-reversal symmetry again means that K is specifically not a good quantum number. However, the authors state that instead of being aligned along the symmetry axis, the np - nh excitations can become aligned along the rotational axis. They

state that in this rotationally aligned scheme, the 4^+ state is predominately $K_x=4$. Similar to Utsuno et al.[31], Egido, Borrajo, and Rodriguez predict a decay matrix element of $1.4 e^2 \text{ fm}^4$ [34], again smaller than the experimental value, but in agreement with the isomeric nature of the state.

Both bmf calculations just discussed predict that the 4^+ state is near maximum triaxiality, but has an approximately pure $K=4$ wave function. This purity of the 4^+ wave function in the context of near maximum triaxiality is a property that remains surprising. Both studies also noted that the intrinsic-frame wave function of the isomeric 4^+ state violates time-reversal symmetry, stated to be nearly maximal in Ref. [33]. It is tempting to speculate whether this property, not present in conventional collective excitations with pure K -quantum numbers, points to a separate implicit symmetry of the mean field leading to an orthogonalization of isomeric and rotational 4^+ states.

Given the exotic structure of the isomeric 4^+ state, the search for the collective rotational 4^+ state gains additional significance. In this context it is interesting to note that Santiago-Gonzalez et al. [4], who were using the same reaction as the present work, were able to reproduce the population of the isomeric 4^+ at a cross section of $0.019(4)$ mb, through a calculation based on an eikonal approximation and shell-model wave functions. The same calculation also produced a cross section smaller than $1 \mu\text{b}$ towards the collective 4^+ state, explained by a lack of overlap with the ^{46}Ar ground state and being consistent with its non-observation. In pursuit of the collective 4^+ state, additional spectroscopic studies with other excitation mechanisms and modern high-resolution γ -spectroscopy methods are called for.

CHAPTER 3

ESTABLISHING RESONANCES IN $^{25}\text{Al}(\text{p},\gamma)^{26}\text{Si}$ VIA THE $(^3\text{He},\text{N})$ REACTION

3.1 Introduction

In this chapter, the resonances in ^{26}Si that contribute to the $^{25}\text{Al}(\text{p},\gamma)^{26}\text{Si}$ reaction are discussed. This reaction is critical to understanding the observed abundance of ^{26}Al in the galaxy. The rest of this introduction will discuss the importance of this reaction and the resonances that play a role in determining the reaction rate. Section 3.2 focuses on the experimental techniques, in particular the integration of the neutron wall with the γ array. Section 3.3 focuses on the calibration of the neutron wall and the Doppler correction of γ rays. Section 3.4 presents the results and Section 3.5 discusses the impact of this experiment on the reaction rate.

3.1.1 ^{26}Al in the Galaxy

^{26}Al offers physicists a way to look at the processes occurring inside of stars. The ground state of ^{26}Al β -decays to an excited state in ^{26}Mg , which immediately γ -decays to the ground state emitting a 1.8 MeV γ ray. The half-life of this β -decay is 717,000 years: long enough for ^{26}Al to be created in the stars and then ejected into the interstellar medium, where its decay can be detected by earth-based telescopes. This decay was first observed by the HEAO 3 γ ray spectroscopy experiment in 1982 [37], which provided the first direct observational evidence that nucleosynthesis is ongoing in the galaxy.

Recently, more detailed observations from the COMPTEL imaging telescope [38] and from the INTEGRAL gamma-ray observatory [10] have shown that about 3 solar masses of ^{26}Al exist in the galaxy. Due to the observed spatial distributions of ^{26}Al , shown in Figure 3.1, most of the ^{26}Al is believed to be produced in Wolf-Rayet stars and the supernova that result from their death [10]. However, it is thought that nova could be a secondary source for ^{26}Al , contributing up to $0.4M_{\odot}$ [11].

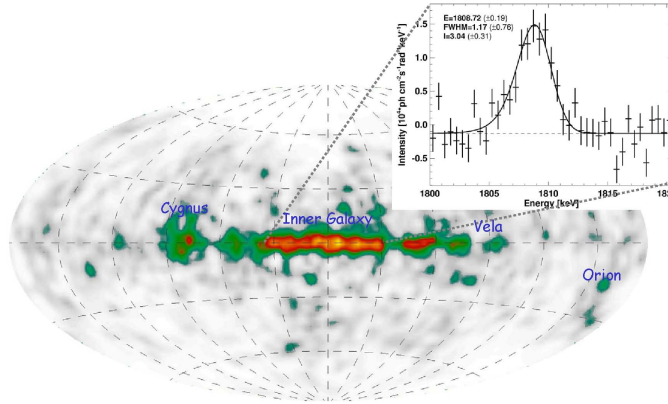


Figure 3.1: Spatial Distribution of ^{26}Al [10]. Due to this observed spatial distribution, most of the ^{26}Al is believed to be produced in Wolf-Rayet stars and the supernova that result from their death [10]. However, it is thought that nova could be a secondary source for ^{26}Al , contributing up to $0.4M_{\odot}$ [11].

A complicating factor in this ^{26}Al story is that ^{26}Al actually has a low-lying isomeric state that β -decays to ^{26}Mg in 6.3s. A partial level structure and decay scheme is shown in Figure 3.2. Notice that the isomeric state in ^{26}Al decays quickly and also decays directly to the ground state of ^{26}Mg , not emitting a 1.8 MeV γ ray. To accurately quantify how much ^{26}Al exists in the galaxy, we must understand how much of the ^{26}Al is produced in the ground state versus how much is produced in the isomeric state.

The production of ^{26}Al in novae can proceed along two main reaction paths. One path leads to the production of ^{26}Al in the ground state, while the other path leads to the production of ^{26}Al in the isomeric state. In order to understand the contribution to ^{26}Al from novae, it is necessary to understand the branching in these two paths. The paths branch at ^{25}Al , which can either β decay to ^{25}Mg or capture a proton and become ^{26}Si . The path through ^{26}Si leads to $^{26}\text{Al}^m$, while the path through ^{25}Mg leads mainly to the ground state of ^{26}Al . The $^{25}\text{Al}(\beta^+\nu_e)^{25}\text{Mg}$ decay occurs with a half-life of 7.2s, so in order for the $^{25}\text{Al}(p,\gamma)^{26}\text{Si}$ reaction to compete with the β decay, it must proceed on a similar time scale. This current experiment populates resonances in ^{26}Si in order to indirectly determine the $^{25}\text{Al}(p,\gamma)^{26}\text{Si}$ reaction rate.

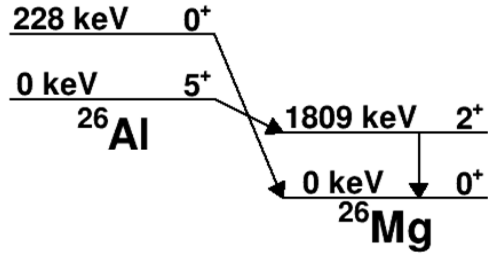


Figure 3.2: ^{26}Al can be produced in the ground state, which β decays to ^{26}Mg with a half-life of 700,000 years, emitting a 1.809 MeV γ ray. Additionally, ^{26}Al can be produced in the isomeric 0^+ state which β decays to the ground state of ^{26}Mg in 6s. The branching of the two pathways that produce these states must be understood in order to understand the observed distribution of ^{26}Al in the galaxy.

3.1.2 Nuclear Physics Effects Influencing the Reaction Rate for $^{25}\text{Al}(p,\gamma)^{26}\text{Si}$

The reaction rate for a nuclear reaction is defined as the number of reactions per time and unit volume. In an astrophysical environment, this rate will depend on the number densities of the reacting particles and on the reaction rate per particle pair. The number densities rely on astrophysical models, while the reaction rate per particle pair can be measured experimentally with a nuclear accelerator. The straightforward way of measuring a reaction rate would be to produce a beam of known energy and intensity, direct it at a target, and count the amount of products that come out in a given time frame. However, at the reaction energies relevant in astrophysical environments (a few hundred keV), the reaction cross sections are very small meaning that very intense beams are needed. In the case of the $^{25}\text{Al}(p,\gamma)$ reaction, sufficiently intense radioactive beams have not yet been produced to make a direct measurement of the reaction rate at astrophysically relevant temperatures possible. To determine this reaction rate, we have to turn to indirect techniques.

The energy distribution of particles in astrophysical environments can be safely described by a Maxwell-Boltzmann distribution. At nova temperatures (0.3 GK), this gives an average energy of about 30 keV for the reactants. This energy is much less than the Coulomb repulsion, so reactions have to occur by tunneling through the Coulomb barrier. Figure 3.3 shows the Maxwell-Boltzmann distribution ($\propto e^{-\frac{E}{kT}}$) plotted with the tunneling probability ($\propto e^{-2\pi\eta}$, where $\eta \propto E^{-1/2}$ is the Sommerfeld parameter). The product of the Maxwell-Boltzmann distribution and the tunneling probability is an estimate for the probability of a reaction to occur. The area around the maximum

of this probability distribution is referred to as the Gamow window. It is the energy region where nuclear reactions are most likely to occur and the resonances that exist inside the Gamow window are likely to contribute the most to the reaction rate. Fig 3.3 shows the location of the known resonances in ^{26}Si inside the Gamow window. As can be seen, there are potentially four resonances that could contribute, although one of the resonances is marked with a question mark because the literature is not in agreement. This will be discussed in detail below.

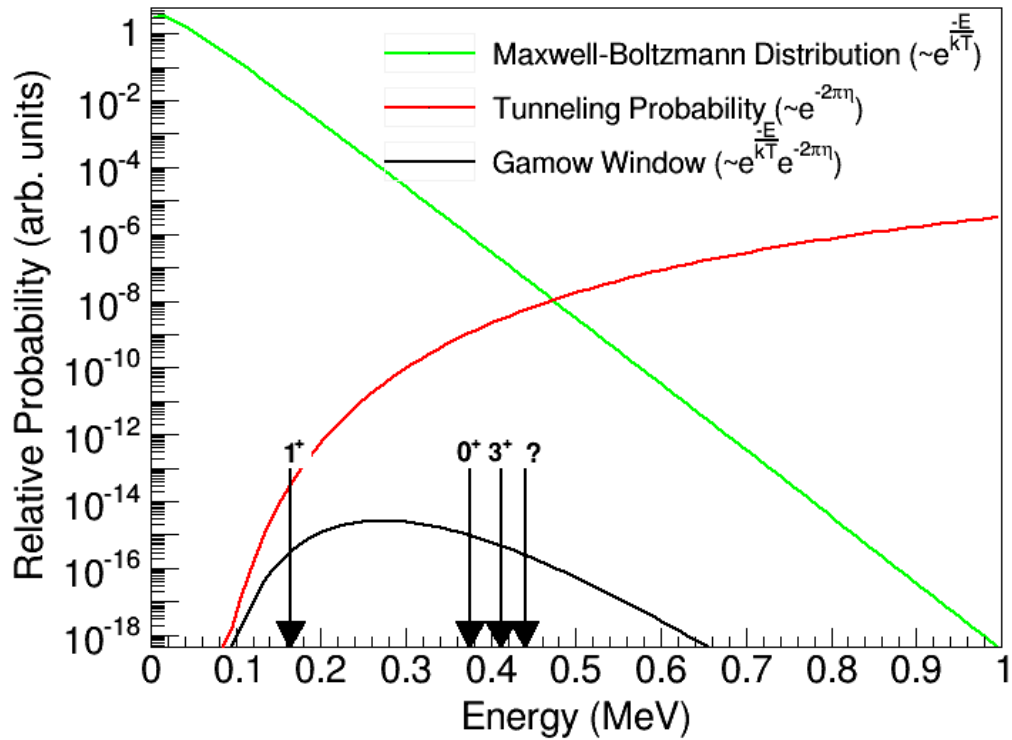


Figure 3.3: The location of the resonances inside the Gamow window. Three resonances seem to be firmly established, while a 4th resonance is less certain.

3.1.3 Previous Works

The states of interest in this work are those that lie above the proton threshold in the Gamow window. From considerations with the mirror nucleus, ^{26}Mg , one expects a 1^+ , a 4^+ , a 3^+ , and a 0^+ state to be located in this energy region. Another 4^+ state is located slightly higher in energy. Shell model calculations performed by Iliadis et al.[39] predict the same four resonances in the Gamow

window, with a 2^+ , 4^+ and a 1^+ at slightly higher excitation energies. The first 4^+ state above the proton threshold has been firmly established at 5.517 MeV[1]. This state is only 4 keV above the proton threshold and never contributes significantly to the reaction rate. This leaves the 1^+ , 3^+ and 0^+ states predicted to lie within the Gamow window and possibly contribute to the rate. However, 4 resonances have been observed in the Gamow window. The rest of this introduction will treat these resonances in detail.

The 1_1^+ Resonance. A state at 5.678 MeV was first observed by a ($^3\text{He},^6\text{He}$) reaction by Caggiano et al.[40]. They assigned this state to be the 1^+ resonance. Since then, multiple experiments have observed and confirmed this 1^+ assignment.

The 0_4^+ Resonance. A resonance at 5.890 MeV has been observed by three recent ($^3\text{He},n\gamma$) experiments[41][42][2]. The most recent measurement reported at Gammasphere by Doherty et al.[2] provided angular correlation measurements that definitively identified this state as a 0^+ .

The 3_3^+ Resonance. The 3^+ resonance has received the most attention because it is expected to contribute the most to the $^{25}\text{Al}(p,\gamma)$ reaction rate at peak nova temperatures. The recent measurements have converged on the 3^+ state being located at about 5.92 MeV. A (p,t) reaction by Bardayan et al.[43] identified a state at 5.914 MeV that was consistent with either a 2^+ or a 3^+ state. A (d,n) transfer reaction performed at FSU that is sensitive to $l=0$ states identified a resonance at 5.914 MeV that must be the 3^+ state[44]. Additionally, a recent β -decay experiment was the first to measure the γ ray branch coming from this state. This experiment by Bennett et al.[12] placed the 3^+ state at 5.929 MeV.

Additional Resonances. The expected 1^+ , 0^+ and 3^+ seem to have been positively identified, but there is also experimental evidence for another state in very close proximity to the 3^+ . A state at 5.916 MeV was first observed by a ($^3\text{He},n$) experiment by Bohne et al. in 1982[45], which assigned it as a 0^+ . This spin parity assignment was confirmed by a (p,t) reaction measured by Bardayan et al. in 2002[46]. Additionally, the (p,t) experiment done in 2002 suggested that a state observed in 1972 also with a (p,t) reaction by Paddock[47] at 5.960 MeV was misplaced. A ($^3\text{He},^6\text{He}$) experiment observed a state at 5.945 MeV and assigned it as a 3^+ [40]. This 3^+ assignment relied partly on the 0^+ assignment for the state at 5.916 MeV. A ($^3\text{He},n$) experiment in 2004 by Parpottas et al.[48] was the first experiment to see both of these states in the same

reaction. This experiment disagreed with the spin and parities that were previously established and assigned the 5.912 MeV state as the 3^+ and the 5.946 MeV state as the 0^+ . Because of these contradictory assignments, Bardayan et al. remeasured the (p,t) reaction with an extended angular coverage[43]. This time they found that the 5.912 MeV state was consistent with either a 2^+ or 3^+ assignment[43], consistent with Parpottas' assignment of a 3^+ [48]. As just discussed, the more recent measurements have all agreed with this 3^+ assignment.

These measurements suggest the existence of a state lying above the 3^+ in excitation energy. However, there is no consensus on what this state is, or if it actually exists at all. The strongest evidence for its existence comes from the experiments that observed both states at 5.92 MeV and at 5.945 MeV. The ($^3\text{He},n$) reaction by Parpottas et al[48] was clearly able to resolve these two states and give definitive J^π assignments of 3^+ and 0^+ respectively. However, the recent ($^3\text{He},n\gamma$) experiments contradict the experiment by Parpottas et al. The recent ($^3\text{He},n$) experiments performed the same reaction as Parpottas and should populate the same states. However, they observe the 0^+ at 5.888 MeV instead of 5.946 MeV. Additionally, Parpottas does not observe a state at 5.888 MeV, although the experiment would have the resolution to do so. One possible conclusion is that Parpottas' energy calibration is systematically off at these energies and that they assigned the wrong J^π to these states. In this case the two peaks from Parpottas could be shifted and the spins flipped, putting the 0^+ at 5.888 MeV and the 3^+ at 5.922 MeV. However, it is unclear why this would be the case.

Additional evidence for a state at 5.95 MeV comes from a recent (p,t) experiment [49] that was able to resolve a state at 5.921 MeV and at 5.944 MeV. They only populated these states weakly and were unable to give definite J^π assignments. However, their observation of the state at 5.921 MeV is in good agreement with the previous (p,t) measurements that also saw a state there. Finally, the ($^3\text{He},^6\text{He}$) reaction[40] observed a state at 5.945 MeV and assigned it as a 3^+ . However, they did not observe the state at 5.92 MeV, so it is possible that the 3^+ observed in this experiment corresponds to the 3^+ at 5.92 MeV.

It seems clear that the 1^+ resonance is at 5.675 MeV, the 0^+ resonance is at 5.890 MeV, and the 3^+ resonance is at 5.92 MeV. It is still not clear what J^π to assign to the resonance at 5.945 MeV. The experiment by Parpottas et al.[48] seems to have some unidentified problem, but two other experiments have identified a state at 5.945 MeV. The goal of the present experiment is to

Table 3.1: List of levels in ^{26}Si in the Gamow window. The 1^+ , 0^+ , and 3^+ are positively identified, while the existence and impact of a 4^{th} resonance is questionable. (see text)

Reaction	1^+		0^+		3^+		?	
	E_x (MeV)	J^π	E_x (MeV)	J^π	E_x (MeV)	J^π	E_x (MeV)	J^π
(p,t)[47]					5.960	?		
(^3He ,n)[45]					5.910	$0^+ + 4^+$		
(p,t)[46]					5.916	0^+		
(^3He , ^6He)[40]	5.678	1^+					5.945	3^+
(^3He ,n)[48]	5.670	1^+			5.912	3^+	5.946	0^+
(p,t)[43]					5.914	$(2^+,3^+)$		
$^{12}\text{C}(^{16}\text{O},2\text{n})[1]$	5.677	1^+						
(d,n)[44]					5.914	$l=0$		
(p,t)[49]					5.921	?	5.944	?
(^3He ,n)[41]	5.677	1^+	5.888	0^+				
^{26}P decay[12]					5.929	3^+		
(^3He ,n)[42]	5.674	1^+	5.890	0^+				
(^3He ,n)[2]	5.676	1^+	5.890	0^+				

repeat the (^3He ,n) reaction to try and resolve both resonances observed by Parpottas et al. with γ ray spectroscopy.

3.2 Experimental Techniques

A 10 MeV of energy, ^3He beam was incident on a 1.1 mg/cm 2 ^{24}Mg target. The ^{24}Mg target was backed by an 11 mg/cm 2 gold foil and a 40 μm tantalum foil. The beam was delivered to the target in short bunches of about 2 ns duration and an 82 ns repetition period, with a current of about 6nA throughout the experiment. The target was surrounded by the FSU Compton-suppressed γ array and a neutron wall was placed 123 cm down-stream of the target, centered on the beam axis.

3.2.1 The FSU Compton-Suppressed γ Array

The target was surrounded by the FSU Compton-suppressed γ -array. The γ array consists of 10 Compton-suppressed, high-purity germanium (HPGe) detectors. Each of the 10 HPGe detectors are surrounded by a bismuth germanate (BGO) shield to reduce the Compton background. Three of the detectors are arranged in a clover configuration and 7 of the detectors are single crystals. Each of the clover detectors is segmented into 4 separate crystals, arranged like a 4-leaf clover, and

shown schematically in Figure 3.4. The HPGe detectors cover laboratory angles of 35° , 90° , and 145° .

Compton Suppression with the γ Array. Unlike GRETINA, the γ array suppresses the Compton background by surrounding the HPGe detectors with a BGO shield. A schematic showing the way in which a clover detector suppresses the Compton background is shown in Figure 3.4, with a few possible γ ray paths shown for illustration. Notice that in a clover detector, Compton scattered γ rays can either scatter into the BGO (Path 3), or they can scatter into an adjacent crystal (Path 2). If the crystals are treated as separate detectors, any event that scatters from one crystal to another will add to the Compton background. However, this can be reduced by adding the energies of the crystal together, referred to as “add-back”. In a clover detector, both paths 1 and 2 will lead to a full collection of γ ray energy, while path 3 will be vetoed in order to reduce the Compton background in the spectrum.

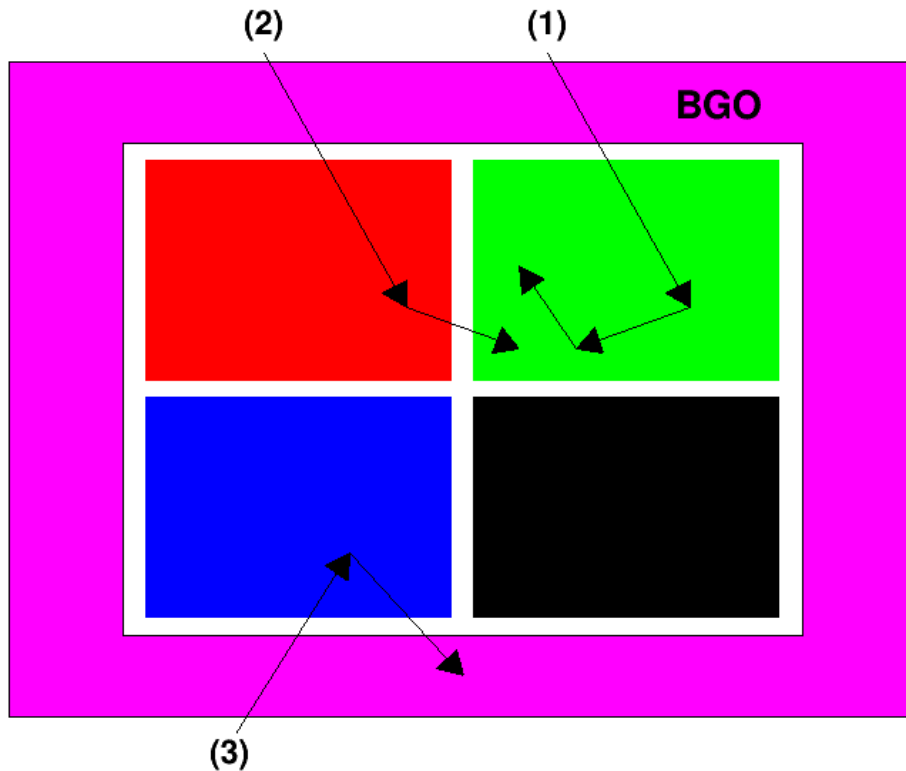


Figure 3.4: A schematic of a Compton-suppressed clover detector. The different paths are discussed in the text.

3.2.2 The Neutron Wall and Electronics

A neutron wall was placed 123 cm down-stream of the target position, centered on the beam axis. The neutron wall consists of 12 plastic scintillators arranged side by side such that an area of 1.5m by 1.7m is covered evenly with detectors. Each bar stands vertically with about 5 cm separating each bar. Each plastic scintillator is connected to 2 photomultiplier tubes at either end of the detector.

The signals from the HPGe array were sent into the digital pulse-processing Pixie-16 data acquisition system, standard at FSU. The signals from the neutron wall had to be processed before being sent into the same acquisition system. The γ ray acquisition system has a sampling rate of 100 MHz, meaning that it samples the incoming signals once every 10ns. For this experiment, the time-of-flight needs to be measured on the order of a couple of ns, so the built in sampling rate is not good enough.

In this set-up, analog electronics are used to accurately measure the tof between the detection of a neutron and the reference signal of the accelerator. A schematic of the processing is shown in Figure 3.5. The signals from the neutron bars were sent first to a constant fraction discriminator (CFD) and then to a time-to-amplitude converter (TAC). Note that all of the signals coming from the top of the neutron bars were sent to one TAC and all of the signals coming from the bottom of the neutron bars to a second TAC. Each TAC takes two signals and converts the time between the arrival of the two signals into a square wave whose height is proportional to the tof. In this experiment, the neutron signal was used as the start of the TAC and the rf of the linac was used as the stop. The output of both TACs was fed directly into the Pixie-16 system.

Additionally, all 24 neutron output signals were fed from the CFD into the Pixie-16 system. This is important because neutrons of the same energy, but traveling at different directions, will reach the neutron wall at different times due to the difference in distance traveled. As noted before, these signals rise too fast for Pixie-16 to be able to process them effectively, but Pixie-16 can register whether a signal occurred or not. These signals allow us to assign the neutron detection to a specific detector system allowing for path length differences and kinematic corrections to be taken into account.

In order for data to be written to disk, both TACs had to fire in coincidence with at least one HPGe detector within a $1\mu\text{s}$ time window. The individual outputs of the neutron wall did not play a part in the triggering mechanism.

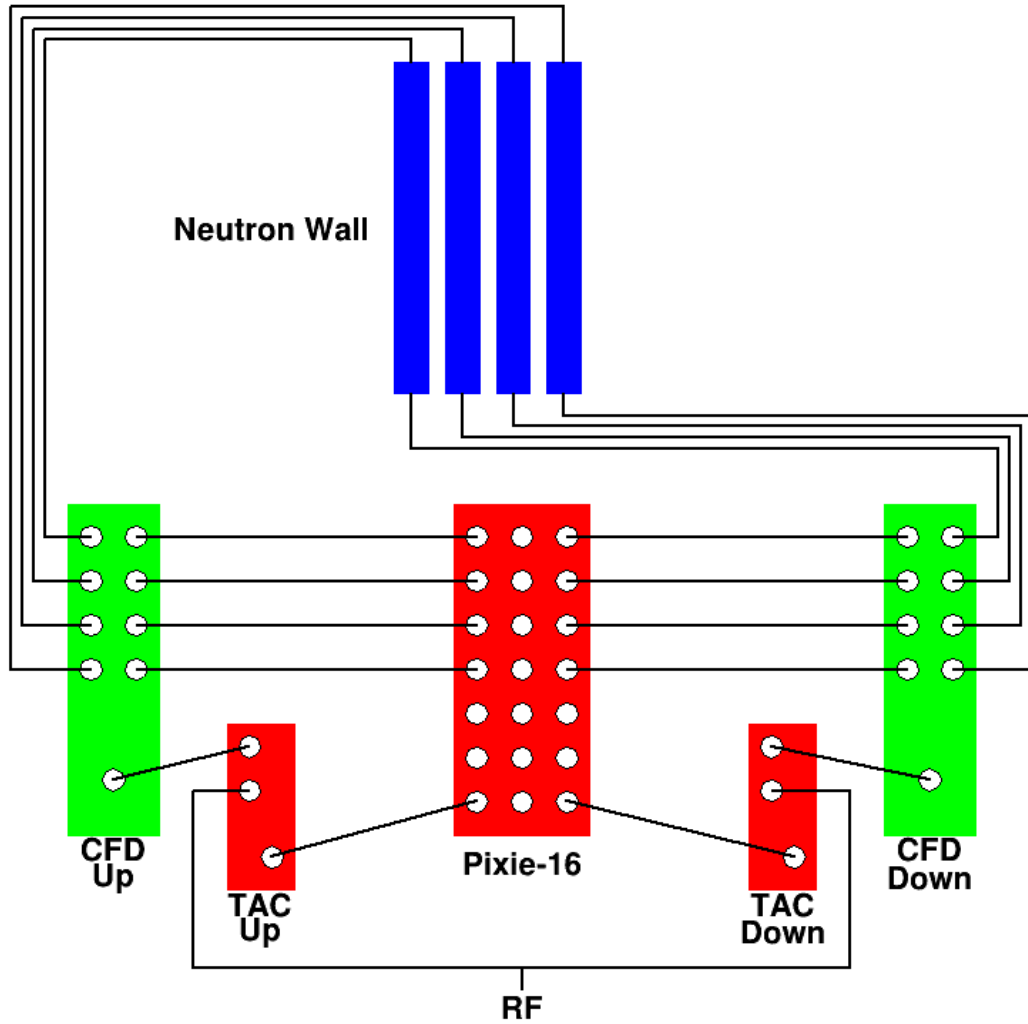


Figure 3.5: A schematic of the electronic set up used in this experiment. The TACs are used to measure the tof between the neutron wall signal and the RF-reference of the linac. All of the 'up' signals go to one TAC and all of the 'down' signals go to a second TAC. The information about which neutron bar fired is recovered by sending all 24 neutron output signals from the CFD into the Pixie-16 system. Note that only 4 of the 12 neutron bars are shown.

3.2.3 Reaction Kinematics

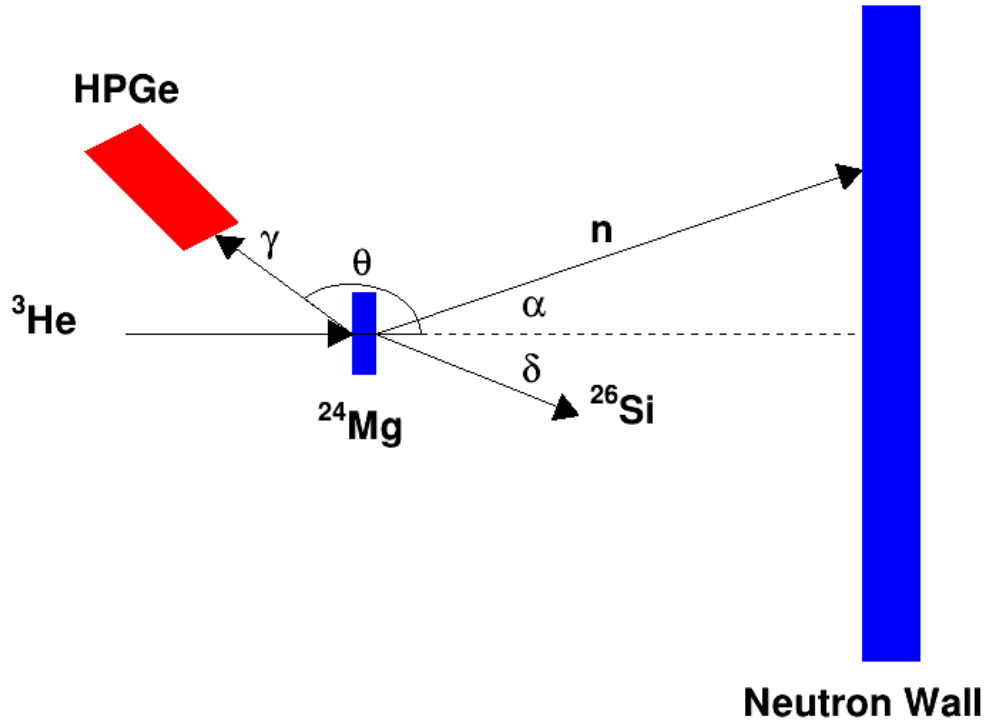


Figure 3.6: Schematic of the reaction and the detectors. The neutron energy and angle, α , are measured such that the energy and angle, δ , of the undetected ^{26}Si can be reconstructed.

This experiment uses the reaction $^3\text{He} + ^{24}\text{Mg} \rightarrow ^{26}\text{Si} + \text{n}$. This reaction is shown schematically in Figure 3.6. The recoiling ^{26}Si remains undetected, but by applying conservation of energy and momentum, we can derive two parameters: 1) Determine the Q-value of the reaction and 2) Determine the momentum of the recoiling ^{26}Si . The Q-value tells us directly which excited state in ^{26}Si was populated while the momentum is used to improve the Doppler correction.

Q-Value Calculation. The Q-value of the reaction is the difference in initial and final masses of the reaction shown in equation 3.1, where the subscripts refer to the mass number of the element in question. The mass of the particle includes both the mass of the particle in the ground state and the mass due to the excitation energy of the particles. In this case, the ^3He and ^{24}Mg are assumed to be in the ground state, while ^{26}Si can be in an excited state.

$$Q = m_3 + m_{24} - (m_{26}^* + m_n) \quad (3.1)$$

The Q-value is determined by applying conservation of energy and momentum to this reaction. The energy of the beam, ${}^3\text{He}$, is known, ${}^{24}\text{Mg}$ is at rest, and the neutron is detected. The conservation of energy and momentum implies that the total energy before and after the reaction, as well as the momentum before and after the reaction, must be conserved. This is shown in equations 3.2 and 3.3.

$$E_3 + E_{24} = E_{26} + E_n \quad (3.2)$$

$$\vec{p}_3 = \vec{p}_{26} + \vec{p}_n \quad (3.3)$$

These equations can be combined by introducing a number of simplifications. The energy is a combination of kinetic and mass energy, $E = T + mc^2$. Noting that the kinetic energy of ${}^{24}\text{Mg}$ is zero and solving for the Q-value, equation 3.2 can be rewritten as equation 3.1.

$$Q = T_{26} + T_n - T_3 \quad (3.4)$$

By solving equation 3.3 for the unknown momentum of ${}^{26}\text{Si}$ and squaring both sides, equation 3.3 can be rewritten as equation 3.5. Additionally, in a classical approximation, the momentum can be written in terms of energy by recalling that $T = \frac{p^2}{2m}$, equation 3.6. Note that equation 3.6 uses the ground state mass for ${}^{26}\text{Si}$. Since ${}^{26}\text{Si}$ is generally in an excited state, this is an approximation.

$$p_{26}^2 = p_3^2 + p_n^2 - 2p_3p_n \cos \alpha \quad (3.5)$$

$$T_{26} = \frac{1}{m_{26}} \left(m_3 T_3 + m_n T_n - 2\sqrt{m_3 m_n T_3 T_n} \cos \alpha \right) \quad (3.6)$$

Equation 3.6 can be substituted into equation 3.1, giving the final result for the Q-value shown in 3.7. This equation depends on the masses of the particles and the beam kinetic energy, which are known, and on the neutron kinetic energy and angle which are measured. The angular dependence implies that neutrons emitted from the same excited state but at different angles will have different

energies and hence different time of flights. In general, applying kinematic corrections to the time-of-flight spectrum can improve the resolution; however, this dependence on the angle is relatively small over the angular coverage in this experiment. Equation 3.7 can be solved for the neutron energy and the dependence of the energy on the angle is shown in Figure 3.7. This experiment covers an angular range of about 30° , so the difference in energy over this range is only about 100 keV. This is less than our resolution, so should not make a huge impact.

$$Q = T_n - T_3 + \frac{1}{m_{26}} \left(m_3 T_3 + m_n T_n - 2\sqrt{m_3 m_n T_3 T_n} \cos \alpha \right) \quad (3.7)$$

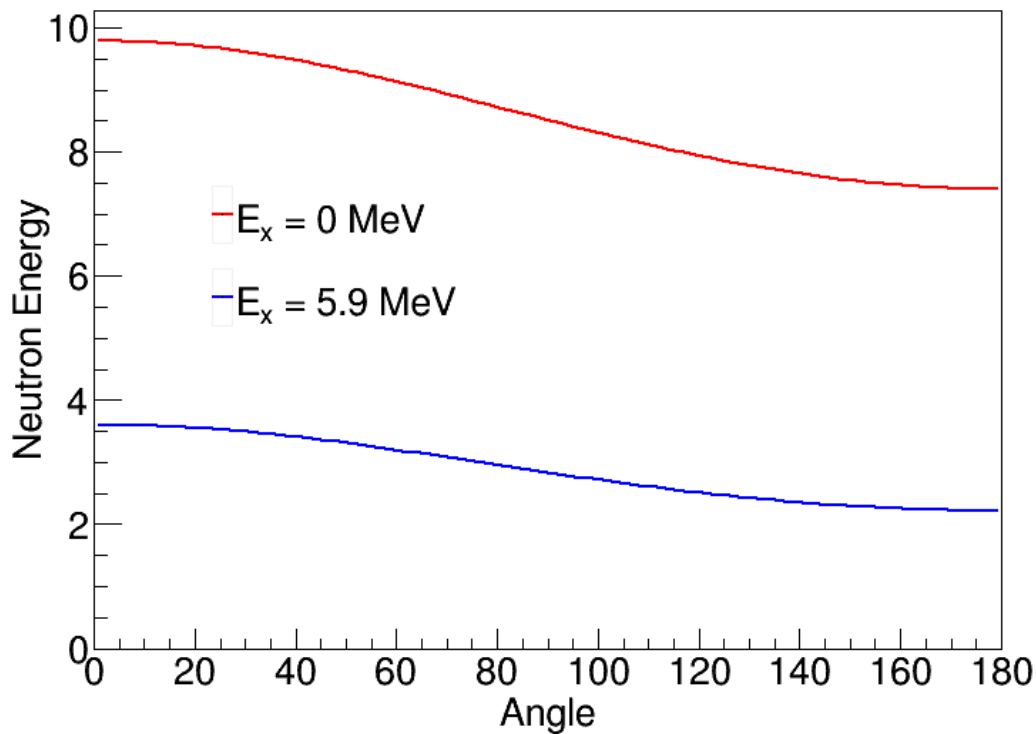


Figure 3.7: Dependence of neutron energy on angle for population of ground state and an excited state. This experiment only covers an angular range of about 30° , so this kinematic correction does not make a large difference.

3.3 Analysis

In this analysis, two complimentary tools are used to study the excitation structure of ^{26}Si . The neutron time-of-flight (tof) information allows us to see directly which level in ^{26}Si was populated, but only to a resolution of about 700keV. High-resolution γ -ray spectroscopy allows us to reconstruct the various levels to a few keV precision. First, we will discuss the determination of the neutron time of flight and Q-value.

3.3.1 Calibration of the Neutron Time of Flight

The goal of this analysis is to determine the energy of the neutrons that are detected, so that the excitation energy of ^{26}Si can be deduced. The tof is measured between the rf of the accelerator and the detection of the neutron in the scintillator. The raw tof spectra are shown in Panel a of Figure 3.8. When each beam packet is incident on the target, the neutron wall detects a spectrum of prompt γ rays followed by neutrons. The two prominent peaks seen in the spectra come from the prompt γ rays and are referred to as the γ -flash. There are two peaks because the beam packets arrive 82ns apart, but the accelerator RF-reference uses a 164 ns period. To the left of each of the large peaks, there are regions of flight times which indicate the arrival of the slower neutrons.

In order to convert the TAC signal into a useful time-of-flight, the following procedure is applied. The TAC spectra can be improved immediately by correcting for the dependence of detector time on the event position within the detector. This is done by averaging the signals taken from the “up” and “down” outputs. This averaged TAC spectrum is shown in Panel b of Figure 3.8. The two peaks that correspond to the γ -flash now appear Gaussian. Although the timing electronics are shared between all up and down signals, the events can be distinguished according to which neutron bar fired. The two peaks from the γ -flash can be used to perform a tof calibration. The distance to the array is known, so the time at which the γ rays reach the detector is also known. From these two points we can perform a calibration individual to each bar. The calibrated average tac is shown in Panel a of Figure 3.9. The averaged tac spectra can be simplified by folding the spectra over. Notice that we have two identical γ ray peaks followed by neutron structures. The second structure comes 82ns after the first, so a new spectrum is created by subtracting 82ns from all data greater than 80ns. This new spectrum is shown in Panel b of Figure 3.9. After all corrections are applied, the prompt γ -peak for a single bar has a fwhm of about 2ns.

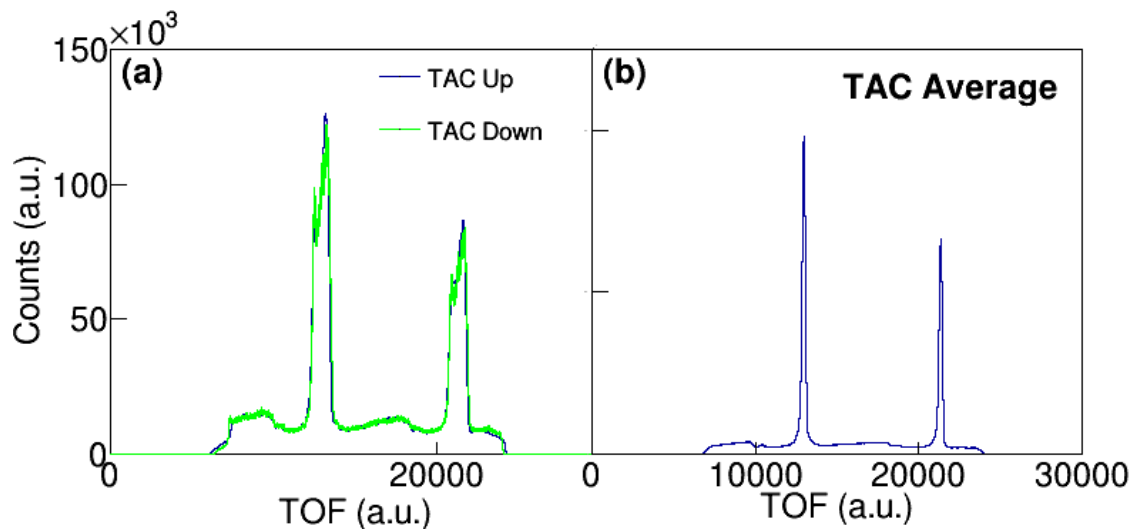


Figure 3.8: Panel a shows the raw tac signals coming from the top of the bars and the bottom of the bars. Panel b shows how averaging the up and the down signals greatly improves the timing resolution. The two prominent peaks seen in the spectra come from the prompt γ rays and are referred to as the γ -flash. To the left of each of the large peaks, there are regions of flight times which indicate the arrival of the neutrons.

This calibrated tof spectrum can be improved in two different ways: 1) By applying path length corrections to the tof spectra and 2) By applying kinematic corrections to the data. These two methods diverge at this point and will be discussed separately.

Path Length Correction to the Time of Flight. The tof just determined is an accurate measure of the time it takes a neutron to travel from the target location to the neutron wall. This tof focused on the arrival of the neutrons is shown in Panel a of Figure 3.10. Note that there are no clear peaks in this spectrum due to kinematic broadening. In other words, neutrons that are released from the same state, hence that have the same energy, will reach different locations on the neutron wall at different times. This can be corrected by calculating the velocity of the neutrons, which is independent of distance traveled. The flight path distance is known for each neutron, so the tof can be converted into a velocity. However, doing so would invert the time spectrum and its binning. To avoid this complication, the velocity is parameterized as a path-corrected tof by dividing the straight line distance to the wall by the velocity. This parameterization is shown in Panel b of Figure 3.10. This new adjusted tof shows clear peaks, corresponding to different populated excited states in ^{26}Si .

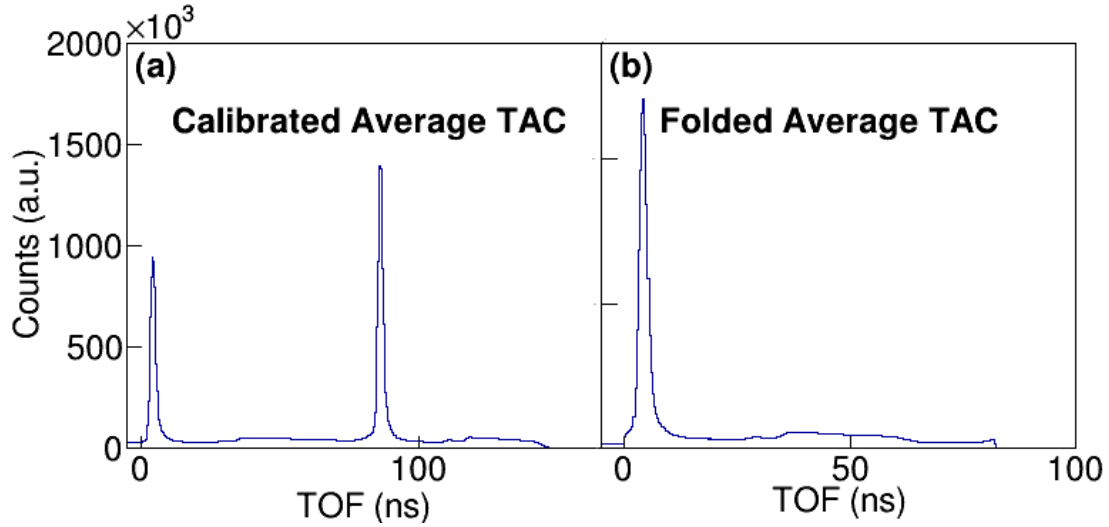


Figure 3.9: The two γ flashes arrive 82ns apart and can be used to calibrate the tof, shown in Panel a. There are two identical structures of γ rays followed by neutrons that can be lined up with one another (Panel b).

Determining the Q-value of the Reaction. The second possible improvement works in parallel to the first. Here, the calibrated tof spectra are used to calculate the Q-value of the reaction. As discussed above, the Q-value spectrum is equivalent to the excitation energy of ^{26}Si . Applying equation 3.7 to the calibrated tof shown in Figure 3.10, the Q-value spectrum can be calculated for this data as shown in Figure 3.11. Notice that in converting from time of flight to Q-value, the time is inverted and squared, creating a compression of the bins. For this reason, a variable bin width was used in Figure 3.11.

To get an idea for how well these two calibrations performed, Figure 3.12 shows the final tof (Panel a) and excitation energy spectrum (Panel b) in coincidence with γ rays coming from the $0_4^+ \rightarrow 2_2^+$ transition at 3104 keV. The final tof spectrum has a fwhm of 3.3 ns and the final excitation energy spectra has a fwhm of 450 keV. The resolution in the excitation energy depends on the neutron energy. Slower neutrons have less fractional uncertainty in the energy, leading to a sharper peak in the reconstructed excitation energy. The fwhm of the 3.3 MeV peak in the excitation energy spectrum, reconstructed from events in coincidence with the $0_2^+ \rightarrow 2_1^+$ γ ray transition, is about 900 keV as opposed to the 450 keV fwhm peak at 5.9 MeV.

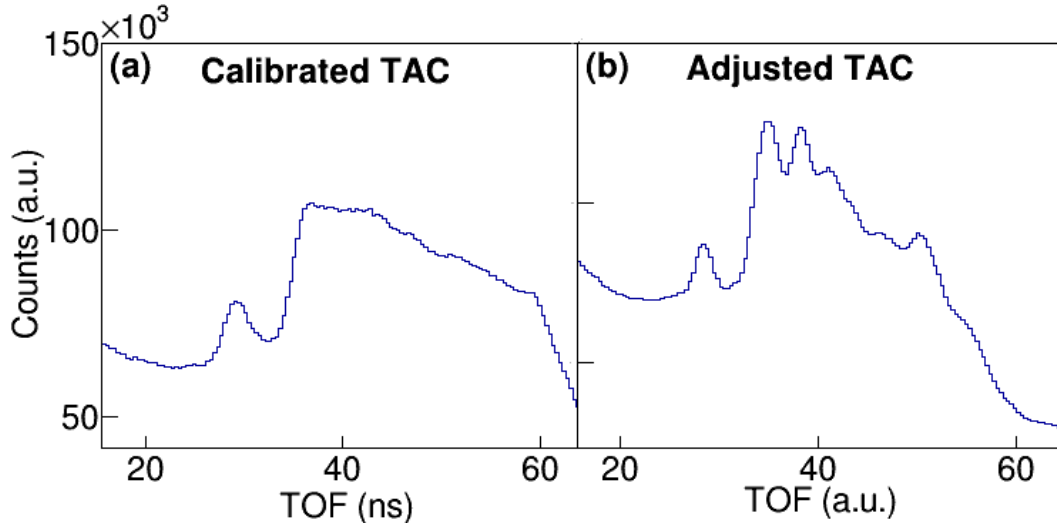


Figure 3.10: The tof spectra zoomed in on the neutrons. Panel a shows the calibrated tof and panel b shows the TOF with path length corrections applied. The path length corrections work by realizing that neutrons of the same energy will have different flight times for different path lengths, but they will have the same velocity. Panel b is essentially the velocity of the neutrons parameterized as a tof.

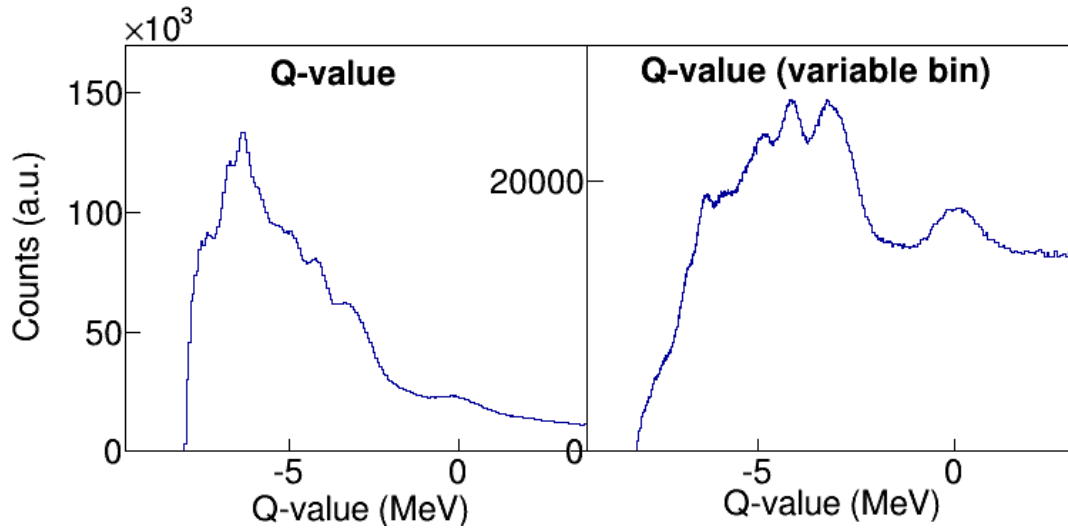


Figure 3.11: The reconstructed Q-value. The data in both panels is the same, but Panel b uses a variable bin width while panel a uses a fixed bin width.

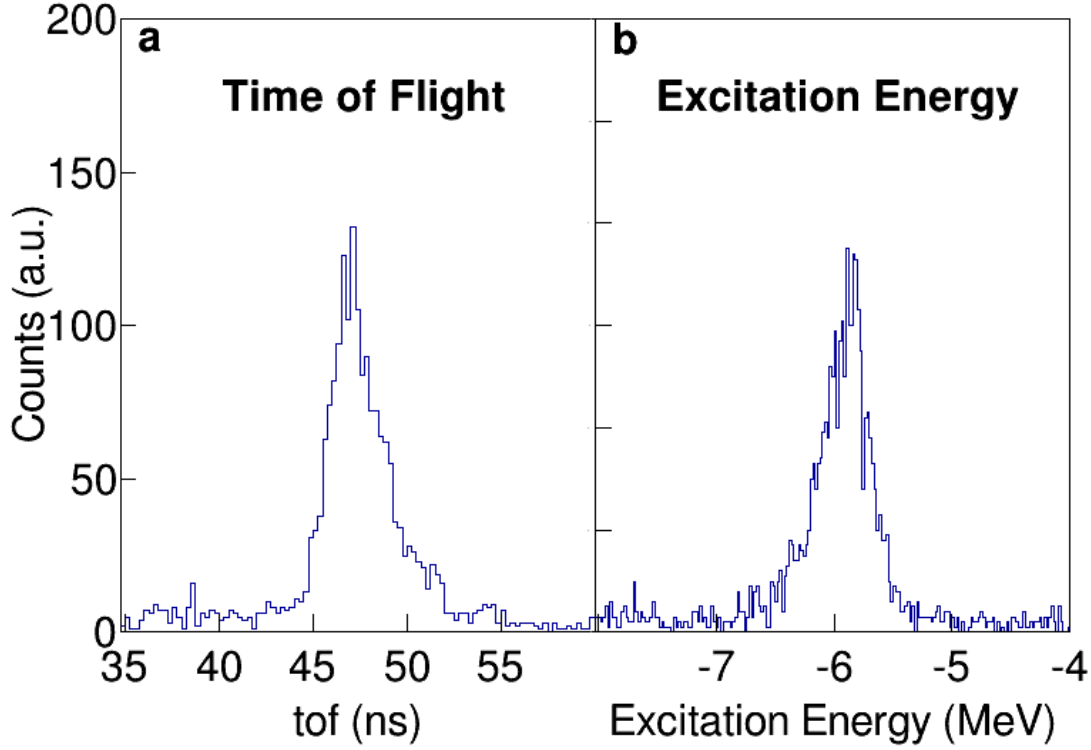


Figure 3.12: The neutron tof spectrum (Panel a) and reconstructed excitation energy (Panel b) in coincidence with γ rays coming from the $0_4^+ \rightarrow 2_2^+$ transition. These peaks have a full width half max of 3.3 ns and 400 keV, respectively.

3.3.2 Energy and Efficiency Calibration of the γ Rays

Each of the 10 clover detectors had an energy calibration obtained from a ^{152}Eu source. The centroids of 6 peaks were found ranging from 121 keV to 1408 keV. A linear function was fit to these data points. Once the energy calibration was applied, a relative efficiency calibration was performed, also obtained from the ^{152}Eu source. The efficiency is parameterized as in equation 3.8. The plot of $\log_{10}(\text{Eff})$ vs. Energy is shown in Figure 3.13. Note that this calibration is a relative calibration and does not give the absolute efficiency of the array. Also note, that the efficiency actually decreases below 100 keV, a feature not shown in the fit.

$$\log_{10}(\text{Eff}) = A + B\log_{10}(E) + C\log_{10}(E)^2 + \frac{D}{E^2} \quad (3.8)$$

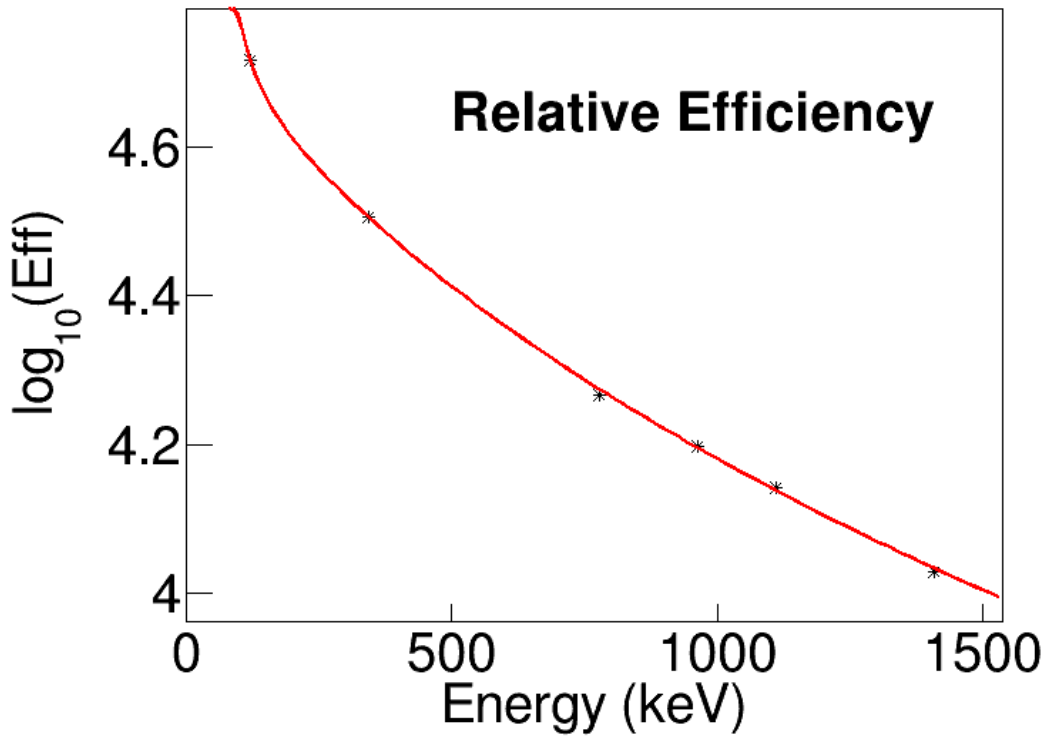


Figure 3.13: The relative efficiency of the γ array as a function of energy. Note that this efficiency calibration is done relative to the area of the 121 keV peak in ^{152}Eu .

3.3.3 Doppler Shift of γ Rays

The need to correct for the Doppler shift of γ rays was discussed in the previous chapter with respect to GRETINA. Here we will discuss some of the specifics to this experiment. The ^{24}Mg target is backed by a gold foil such that all of the recoiling ^{26}Si will stop before leaving the target and backing. This means that once created, the ^{26}Si will immediately start slowing down. It comes to a complete stop in less than a ps, so any states that live longer than a few hundred fs will not need to be Doppler corrected. The lifetimes of the states of most interest to this work, namely those above the proton threshold, are not known precisely, but are expected to decay on the order of fs. For these quickly decaying states, a Doppler correction is necessary. In this case the recoiling nuclei are not traveling at relativistic velocities, so the non-relativistic approximation for the Doppler shift is used as shown in equation 3.9

$$E_{lab} = (1 + \beta \cos(\theta)) E_{com} \quad (3.9)$$

Two different Doppler corrections were applied. The first assumes that the recoiling nucleus is traveling along the beam direction and that the velocity is fixed. The velocity of the recoiling nucleus was found by determining which velocity would line up the γ rays detected at 35° , 90° , and 145° . If the Doppler correction is performed assuming that all of the ^{26}Si recoil is moving along the beam direction, then the γ rays detected at detectors located at 90° will be unaffected by this correction. All three of the clover detectors are located at 90° , but the Doppler correction can be improved on by treating the individual crystals separately. The 4 crystals are identified by a symbolic color: red, green, blue, and black. The red and green crystals sit at slightly backward angles and the blue and black crystals sit at slightly forward angles. Figure 3.14 shows a section of the γ ray spectra for the red and blue crystals of clover 2. Panel (a) compares the red and blue crystals assuming they are at 90° , hence no Doppler correction applied. The behaviors of these peaks illustrate the effect discussed above. The 1540 keV peak comes from a state with a known lifetime of 1.5ps, so it decays at rest. The 1400 keV state comes from a higher lying state with a much shorter lifetime and so the Doppler correction becomes necessary. Notice that the peak at about 1540 keV is lined up perfectly, while there is a noticeable shift between the red and the blue crystals at 1400 keV. If the Doppler correction is done such that the red crystal is at 96° and the blue crystal is at 84° , then the γ ray at 1400 keV lines up and the peak at 1540 keV is shifted, as shown in Panel b of Figure 3.14.

Determining Recoil Direction for Doppler Correction. This first Doppler correction works very well, but a modest improvement can be made by incorporating the information about the kinematics. The direction and velocity of the ^{26}Si recoil, reconstructed event by event, can be used to Doppler correct the detected γ rays. In order to improve the Doppler correction, the angle between the recoiling ^{26}Si and the detector that detects the γ ray must be determined. Since this reaction involves two outgoing particles, momentum conservation requires that the reaction occurs in a 2D plane. Figure 3.6 defines all of the relevant angles within this plane. The orientation of this plane is arbitrary as far as the kinematics are concerned, but is important in determining the angle with respect to the γ ray detector. This orientation is determined by measuring the laboratory phi angle of the detected neutron. The ^{26}Si phi angle is then 180° opposite the neutron phi angle.

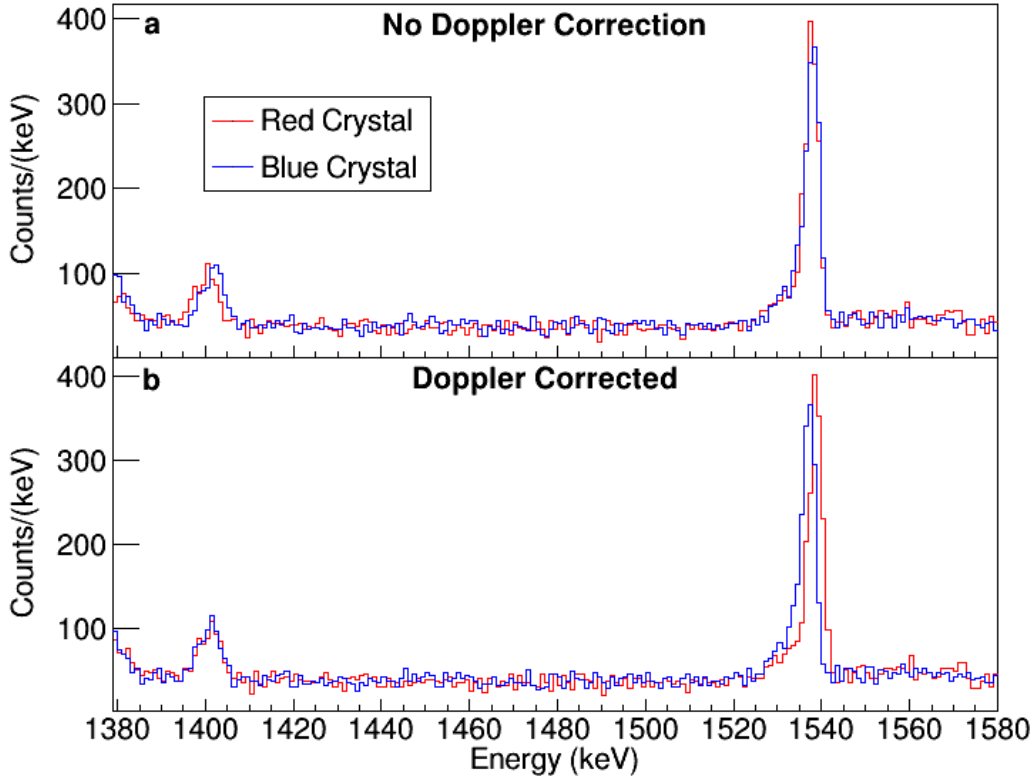


Figure 3.14: Determination of angle for crystals within a clover detector with respect to the beam axis. Panel a assumes that the red and blue crystals are located at 90° . Panel b assumes that the red crystal is at 96° and the blue crystal is at 84° . This correction is important in maximizing the resolution for very fast transitions such as the 1400 keV γ ray shown in the spectra. However, the Doppler correction hurts the resolution for states that decay after the ^{26}Si recoil has come to a complete stop, such as for the 1538 keV γ ray.

The angle between the recoiling nucleus and the beam direction, δ , can be determined using the same conservation of energy and momentum equations discussed in Section 3.2.2. By solving equation 3.3 for the neutron energy and squaring both sides we get an equation for the neutron momentum in terms of δ as shown in equation 3.10.

$$p_n^2 = p_3^2 + p_{26}^2 - 2p_3p_{26} \cos \delta \quad (3.10)$$

Equation 3.10 can be rearranged to solve for the angle, δ , and the kinetic energy can be substituted in for momentum. Additionally, we can substitute for the kinetic energy of ^{26}Si using

equation 3.4. The final equation for the angle is shown in equation 3.11.

$$\cos \delta = \frac{E_3(m_3 + m_{26}) - E_n(m_n + m_{26}) + m_{26}Q}{2\sqrt{m_3 E_3 m_{26} (E_3 - E_n + Q)}} \quad (3.11)$$

If the position of the γ ray detector is given by the usual spherical coordinates (θ, ϕ) and the direction of the recoiling ^{26}Si is given by the coordinates (θ', ϕ') , then the angle between the recoil and the detector is given by equation 3.12.

$$\cos(\text{angle}) = \sin \theta \sin \theta' \cos(\phi - \phi') + \cos \theta \cos \theta' \quad (3.12)$$

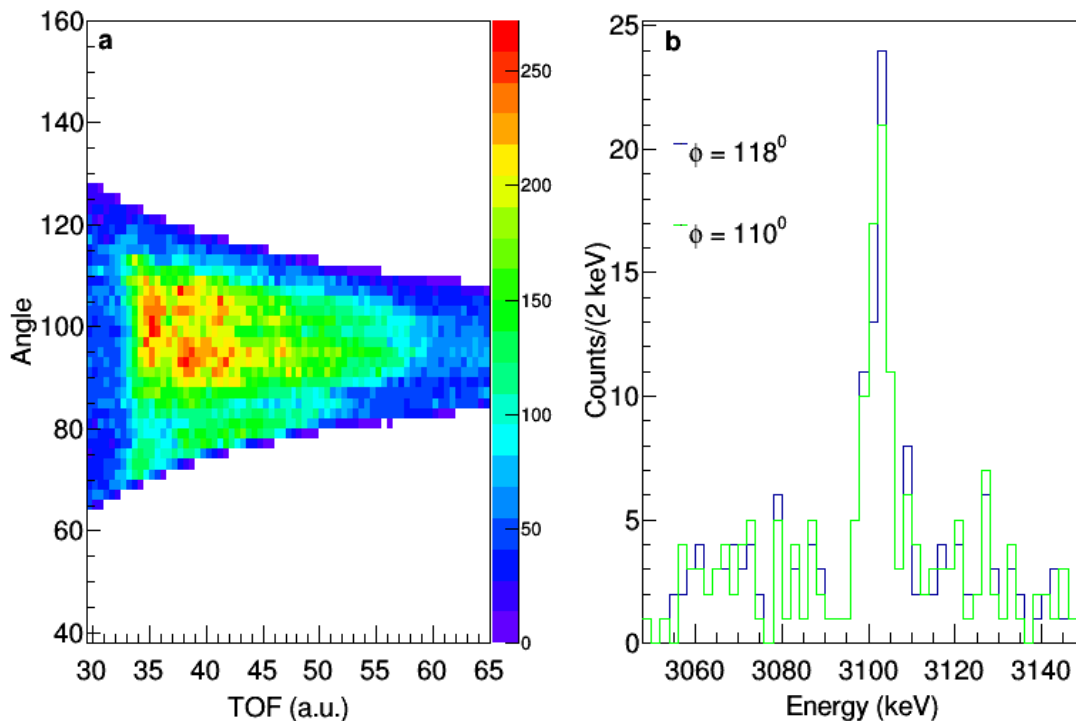


Figure 3.15: Reconstructed angle between recoiling ^{26}Si and detector as a function of neutron time of flight (Panel a). The phi angle was not measured for each HPGe, so Panel b shows the small effect that changing the assumed phi for a given crystal by a small amount has on the γ ray spectra.

Panel (a) of Figure 3.15 shows the distribution of angles between the recoiling nucleus and the clover 2 “green” crystal. If just the beam direction was used for Doppler correction, the angle for

these events would be a fixed 96° . Incorporating the kinematics shows that the recoiling nucleus can be 10° or more off axis. A complication here is that the laboratory θ and ϕ positions of the HPGe detectors are needed. The θ angles are known precisely, but the ϕ angles are only known approximately since they were not recorded during the actual experiment. To determine ϕ for each detector, the angle was allowed to vary in the expected range and the ϕ that gave the best resolution was adopted for that particular detector. Panel b of Figure 3.15 shows the effect of changing ϕ for a single crystal in one of the clovers. The spectrum with an adopted ϕ of 118° has slightly better resolution than the spectrum with an assumed ϕ of 110° . The ϕ that gave the best resolution was the ϕ that was adopted for a particular detector. The effect of this Doppler correction is small, and so the uncertainty in ϕ is fairly large. Figure 3.16 shows the γ ray spectrum with no Doppler correction, with a fixed Doppler correction, and with an event by event Doppler correction. The spectrum that include the Doppler correction shows a better resolution than the spectrum that does not, and the spectrum that includes the event by event Doppler reconstruction is slightly better than the fixed Doppler correction.

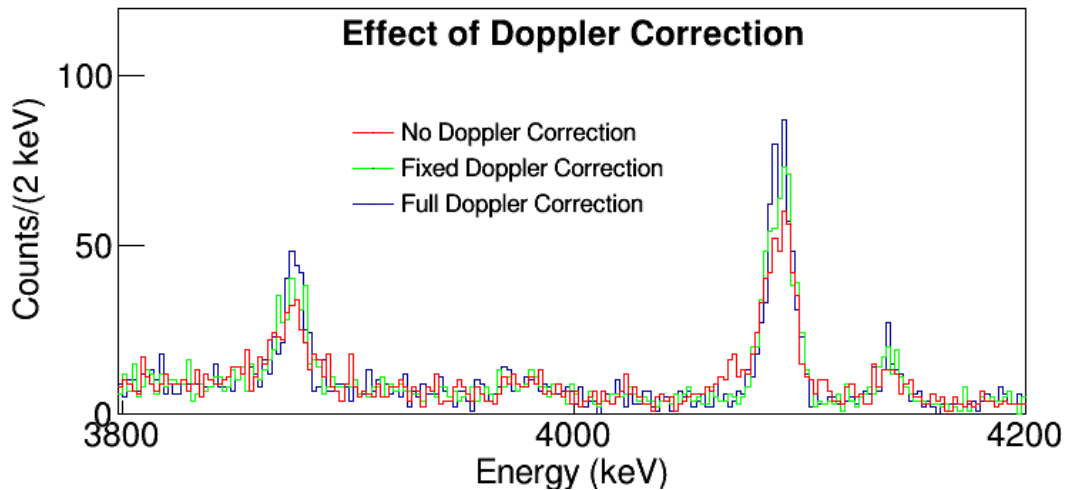


Figure 3.16: The effect of the Doppler correction shown for the γ -array at FSU. The fixed Doppler correction assumes that the recoiling particle is moving along the beam direction with a constant velocity. The full Doppler correction uses the reconstructed recoil direction and velocity.

3.4 Results

The neutron tof and ^{26}Si Q-value spectra can be seen in Figure 3.17. The peaks observed in the tof spectrum are labeled to indicate which state in ^{26}Si was populated. In the Q-value spectrum, the populated energy level can be read directly off of the x-axis. As can be seen in these spectra, the resolution is not good enough to separate different energy levels cleanly. For this, the γ ray spectra, with their superior resolution, must be used.

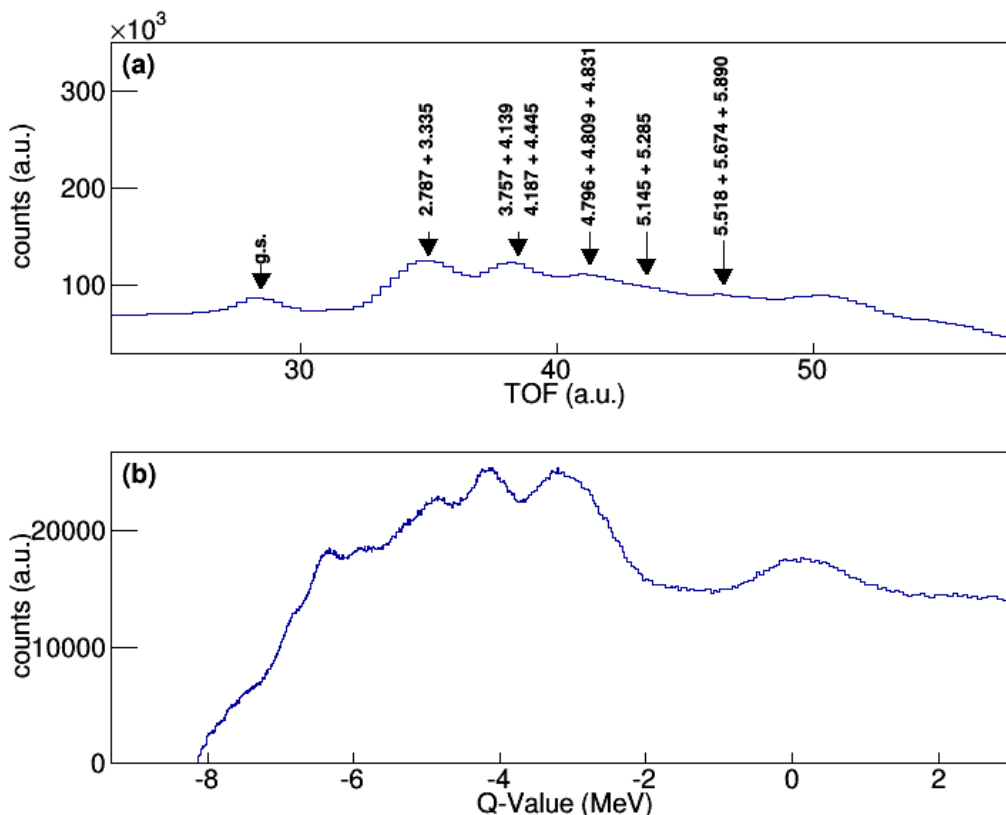


Figure 3.17: The corrected tof (Panel a) and the reconstructed Q-value (Panel b).

The power of combining neutron and γ ray spectroscopy is demonstrated in Figure 3.18. This figure shows a 2D histogram that plots the Q-Value on the y-axis and the γ ray energy on the x-axis. One can read off the excitation energy on the vertical axis and see which γ rays are in coincidence with it. For instance, if one looks at -5.9 MeV on the vertical axis, two strong γ ray peaks are seen strongly in coincidence with this peak. The Q-Value does not have the resolution

to uniquely identify a state, but this can be achieved with the γ ray spectra. Additionally, the Q-value spectrum does not have the resolution to cleanly separate a 5.9 MeV state from a 5.6 MeV state, but if one compares the transitions labeled from the 0_4^+ to the transitions from the 1_1^+ , one can clearly see a shift in energy that indicates that these γ rays do not de-excite the same state.

3.4.1 Establishing the Level Scheme

Figure 3.19 shows the full level scheme for ^{26}Si extracted in this work. The previously observed transitions are shown in black and the new transitions observed in this work are shown in blue. The previous reported transitions that were not seen in this work are shown in red. All transitions are tabulated in Table 3.2. No new levels were discovered in this work, although a number of new transitions were observed.

Figure 3.20 shows the γ ray spectrum in coincidence with neutrons corresponding to de-excitation of states above the proton threshold. All of the largest transitions are labeled in the spectrum. Arrows indicate a single-escape peak from a given state. The two new γ transitions observed are shown in this Figure, labeled in blue. Notice that there is no peak at 1740 keV. This energy corresponds to an expected transition between the 3_3^+ and the 3_2^+ state, reported recently by Bennett et al[12].

Figure 3.21 shows γ rays in coincidence with neutrons corresponding to the de-excitation of states around 4800 keV. In this spectrum, 5 new γ peaks are labeled. Two of these γ transitions depopulate the 4_2^+ state at 4796 keV and 3 of them depopulate the 2_4^+ state at 4809 keV. Figure 3.22 shows two new transitions to the ground state from the 2_5^+ state and from the 1_1^+ state.

3.5 Discussion

This experiment was able to achieve a higher sensitivity than previous experiments, including a ($^3\text{He},n$) reaction done at Gammasphere in 2015[2]. Table 3.2 compares the γ rays seen in this work to those reported in two earlier experiments. Gammasphere has much better angular coverage for γ ray detection than FSU, but this current experiment demonstrates the power of combining neutron spectroscopy with γ ray spectroscopy.

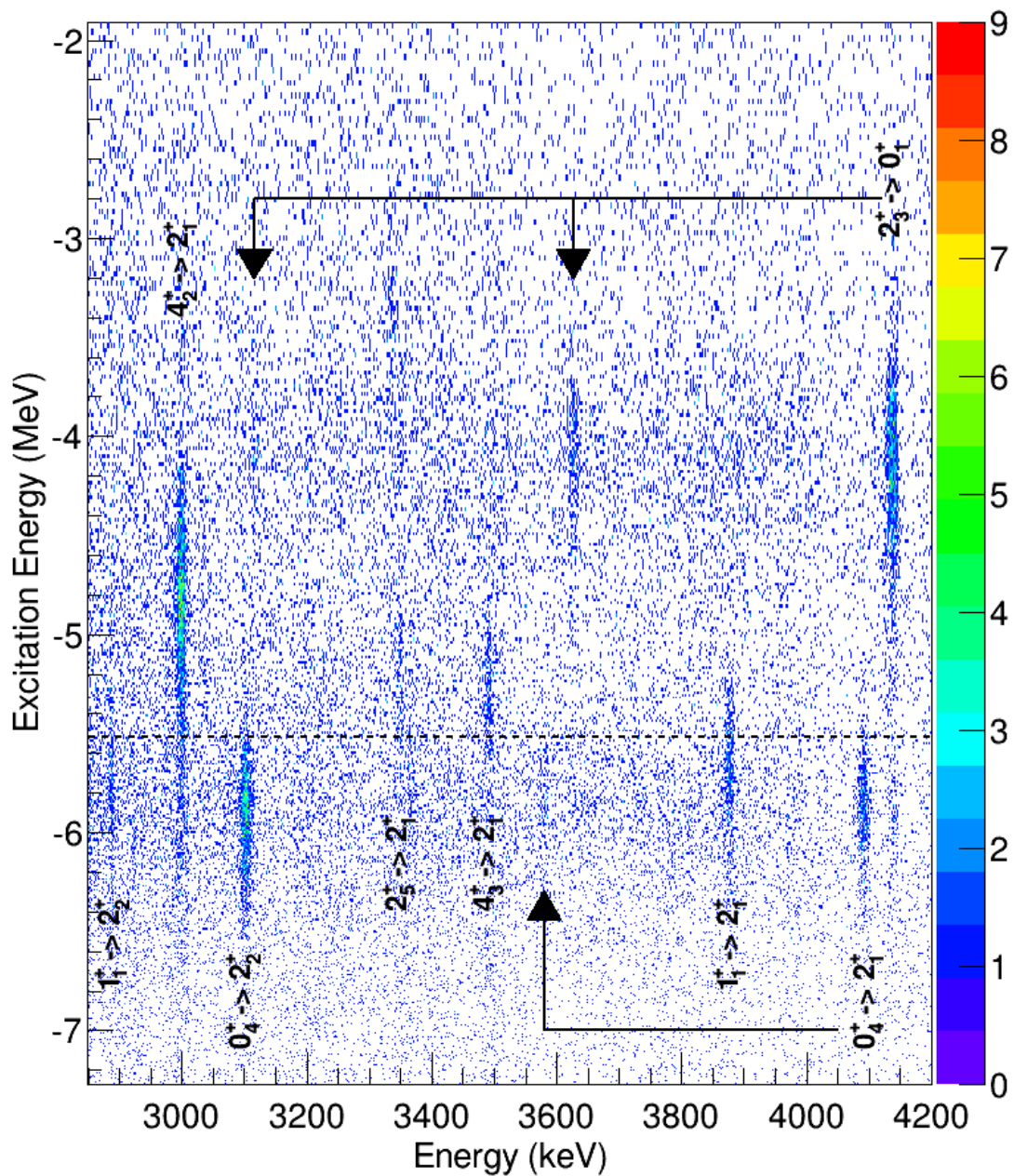


Figure 3.18: The excitation energy plotted against the γ ray energy. The dashed line indicates the proton threshold. The excitation energy provides direct information about which level was occupied in ^{26}Si , while the γ ray energy allows for an indirect but precise determination of the level energy.

Table 3.2: List of observed γ rays. Ref [1] comes from a fusion evaporation experiment and Ref [2] comes from a recent (3He,n). Both experiments were performed using Gammasphere.

E_x [keV]	E_γ [keV]	Branch[%]	[1]	[2]	J^π
1797.0(1)	1797.0(1)	100	1797.2(1)	1797.2(1)	2_1^+
2786.2(1)	989.2(1)	56	988.8(1)	989.1(1)	2_2^+
	2786.2(1)	44	2787.5(3)	2786.6(2)	
3334.6(2)	1537.6(1)	100	1539.1(5)	1539.1(2)	0_2^+
3757.0(3)	970.3(1)	23	970.4(1)	970.6(1)	3_1^+
	1960.2(1)	77	1960.4(2)	1959.8(2)	
4138.1(6)	1352.2(1)	7	1355(2)	1351.9(12)	2_3^+
	2341.3(1)	75	2341.9(6)	2341.8(2)	
	4137.3(2)	18	4141(3)	—	
4187.3(2)	1401.1(1)	63	1400.7(2)	1400.4(2)	3_2^+
	2390.3(1)	37	2391.4(5)	2390.0(3)	
4445.1(2)	—	100	1657(2)	1658.3(14)	4_1^+
	2648.1(1)	100	2648.8(3)	2648.9(2)	
4796.0(2)	609.3(2)	2	—	—	4_2^+
	1040.0(4)	2	—	—	
	2999.0(1)	96	3001.0(4)	2999.1(3)	
4810.1(2)	622.6(1)	3	—	—	2_4^+
	671.6(3)	1	—	—	
	1053.4(3)	1	—	—	
	2023.9(1)	95	2024.2(5)	2025.4(3)	
4830.0(2)	2043.8(1)	100	2044.9(9)	2045.6(3)	0_3^+
5145.2(8)	2359.3(1)	79	2360.2(8)	2360.8(2)	2_5^+
	3348.9(6)	9	3351(2)	3350.3(8)	
	5143.0(10)	12	—	—	
5287.8(5)	842.9(1)	37	842.1(3)	842.5(1)	4_3^+
	1101.3(2)	2	—	—	
	1530.7(1)	40	1531.1(5)	1531.1(6)	
	2501.0(8)	4	2503(2)	2501.9(10)	
	3490.7(3)	17	—	3492.0(2)	
5517.1(5)	1071.7(1)	20	1071.8(4)	1071.4(2)	4_4^+
	1329.4(1)	42	1329.4(3)	1329.4(3)	
	1761.3(4)	27	1764.4(8)	1764.2(4)	
	2730.2(7)	10	2733(3)	2736.3(10)	
5673.2(5)	2887.0(4)	19	—	2888.9(9)	1_1^+
	3876.3(2)	57	3879.4(17)	3878.8(3)	
	5673.0(10)	24	—	—	
5888.4(5)	215.0(2)	1	—	—	0_4^+
	1077.9(8)	1	—	—	
	1750.5(1)	16	—	1751.9(10)	
	3102.4(1)	51	—	3103.0(4)	
	4091.1(2)	31	—	4092.1(4)	

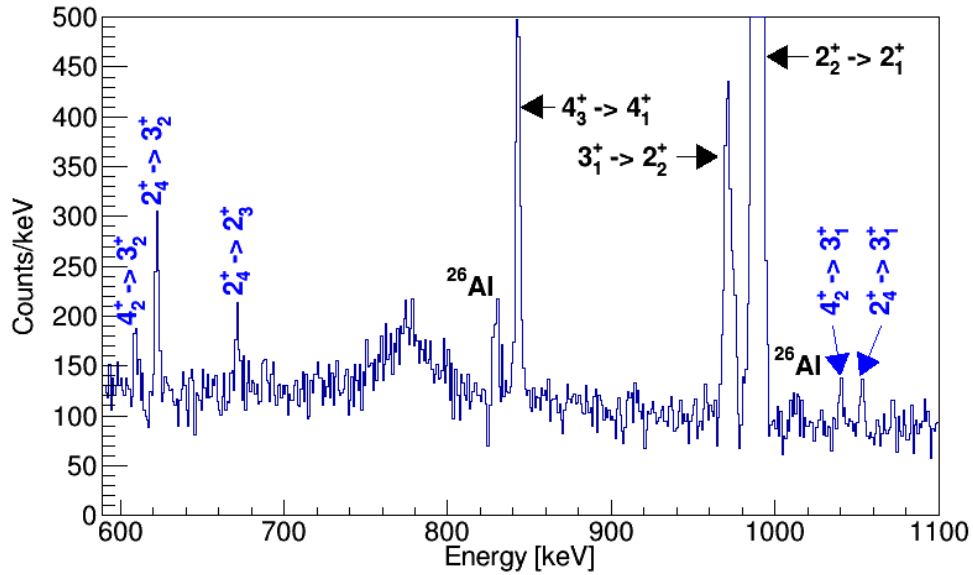


Figure 3.21: γ rays in coincidence with neutrons depopulating states of around 4.8 MeV. Five new transitions are identified in this figure, shown in blue.

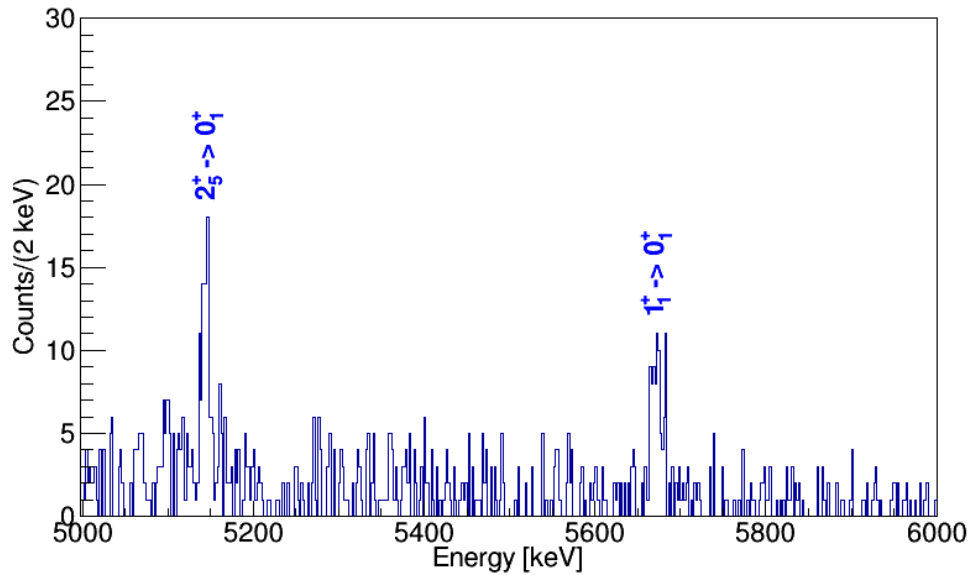


Figure 3.22: γ rays in coincidence with neutrons depopulating states above 5 MeV. Two previously unobserved ground state transitions were observed depopulating the 2_5^+ and the 1_1^+ levels.

The stated goal of this experiment was to establish resonances in ^{26}Si such that the $^{25}\text{Al}(p,\gamma)$

reaction rate could be determined indirectly. This experiment confirmed the location of the 1^+ and 0^+ resonances. However, it is not sensitive to the 3^+ resonance for reasons which will be discussed below. Additionally, this experiment did not observe a resonance at 5.945 MeV. Since this γ -ray experiment is the most sensitive experiment to date, this non-observation of a resonance of 5.95 MeV is an important data point which suggests that this state may not exist.

Two previously observed transitions were not seen in this work. One, depopulating the 4_1^+ level was not seen due to contamination from ^{28}Si . This contaminate is formed in a reaction with ^{27}Al and emits neutrons, meaning that the neutron selectivity of this experiment is not enough to eliminate it. The other transition not observed is in the area of most relevance to the reaction rate of $^{25}\text{Al}(p,\gamma)$. The γ ray depopulating the 3^+ state at 5928 keV observed in a previous experiment could not be seen here. The observation of this γ ray was known to be very difficult, since this state decays by γ -emission only about 1.5% of the time.

To determine whether the current experiment could establish a meaningful upper limit on the γ decay branch, we have to use information from Parpottas et al.[48] and Bennett et al.[12]. Parpottas et al.[48] performed a $(^3\text{He},n)$ reaction at 7.9 MeV and at 10 MeV. At 7.9 MeV, Parpottas et al. was able to resolve states at 5.912 MeV and at 5.945 MeV while at 10 MeV, they were not able to resolve these two states. We assume that these two states correspond to the 5.890 MeV state observed here and the 5.928 MeV state observed in Bennett et al[12]. In the $(^3\text{He},n)$ reaction, the lower energy state had a cross section about 5 times larger than the higher energy state[48]. We also have to assume that this ratio of cross sections is about the same at 10 MeV.

From Parpottas et al.[48], we expect the 3_3^+ to be populated about 20% as much as the 0_4^+ . This 3_3^+ primarily decays through proton emission, so from Bennett et al.[12], we expect only 1.4% of the populated 3_3^+ states to γ -decay. Also according to Bennett et al[12], 71% of the γ -decays should proceed through the $3_3^+ \rightarrow 3_2^+$ branch. Taking these numbers together, we expect that the total intensity of the $3_3^+ \rightarrow 3_2^+$ transition to be 0.2% of the total 0_4^+ intensity. If all of these numbers are correct, we would expect to observe 13 counts in this $3_3^+ \rightarrow 3_2^+$ branch. The background level is at about 40 counts around this energy, so we would need to reduce the background in order to be able to see this transition. Therefore, in future experiments of this kind, it is most important to reduce the background levels in the spectrum.

Table 3.3: Parameters used in determining the $^{25}\text{Al}(p,\gamma)^{26}\text{Si}$ reaction rate.

$E_x[\text{keV}]$	$E_r[\text{keV}]$	J^π	Γ_p (meV)	Γ_γ (meV)
5673.2	159.4	1^+	4.6×10^{-6}	$\gg \Gamma_p$
5888.4	374.6	0^+	25	5.6
5928.7	414.9	3^+	2.9×10^3	40

3.5.1 Determining Reaction Rate

To make an indirect measurement of the $^{25}\text{Al}(p,\gamma)$ reaction, we must know which resonances exist in ^{26}Si inside the Gamow window. These resonances will provide the strongest contribution to the reaction rate. The reaction rate per particle pair can be calculated as a sum over the resonances [50],

$$N_A \langle \sigma \nu \rangle = N_A \left(\frac{2\pi}{\mu k T} \right)^{\frac{3}{2}} \hbar^2 \sum_r (\omega\gamma)_r e^{-\frac{E_r}{kT}}, \quad (3.13)$$

where N_A is Avogadro's number, μ is the reduced mass, k is the Boltzmann constant, T is the temperature, \hbar is the reduced Planck constant, E_r is the resonance energy, and $(\omega\gamma)_r$ is the resonance strength, defined as [50]

$$(\omega\gamma)_r = \frac{2J_r + 1}{(2J_p + 1)(2J_{Al} + 1)} \left(\frac{\Gamma_p \Gamma_\gamma}{\Gamma} \right)_r, \quad (3.14)$$

where J_r is the spin of the resonance, $J_p = 1/2$ and $J_{Al} = 5/2$ are the spins of the reactants, Γ_p and Γ_γ are the proton and γ ray partial widths, and $\Gamma = \Gamma_p + \Gamma_\gamma$ is the total width.

Depending on how the current literature is interpreted, there are either 3 or 4 important resonances in the Gamow window that contribute to the reaction rate. This calculation will assume that the reported state at 5.950 MeV [48] has been misidentified and does not exist. The non-observation of this state in the current experiment provides additional evidence that this state does not exist. To evaluate this reaction rate, we need to know the energy and spin of each resonance, as well as the γ ray and proton partial widths, Γ_γ and Γ_p . The adopted values for these parameters are shown in Table 3.3.

First, using the most recent mass evaluation table [51], the proton threshold is extracted to be 5513.8 keV. The resonance energy is the excess excitation energy of the state above the proton

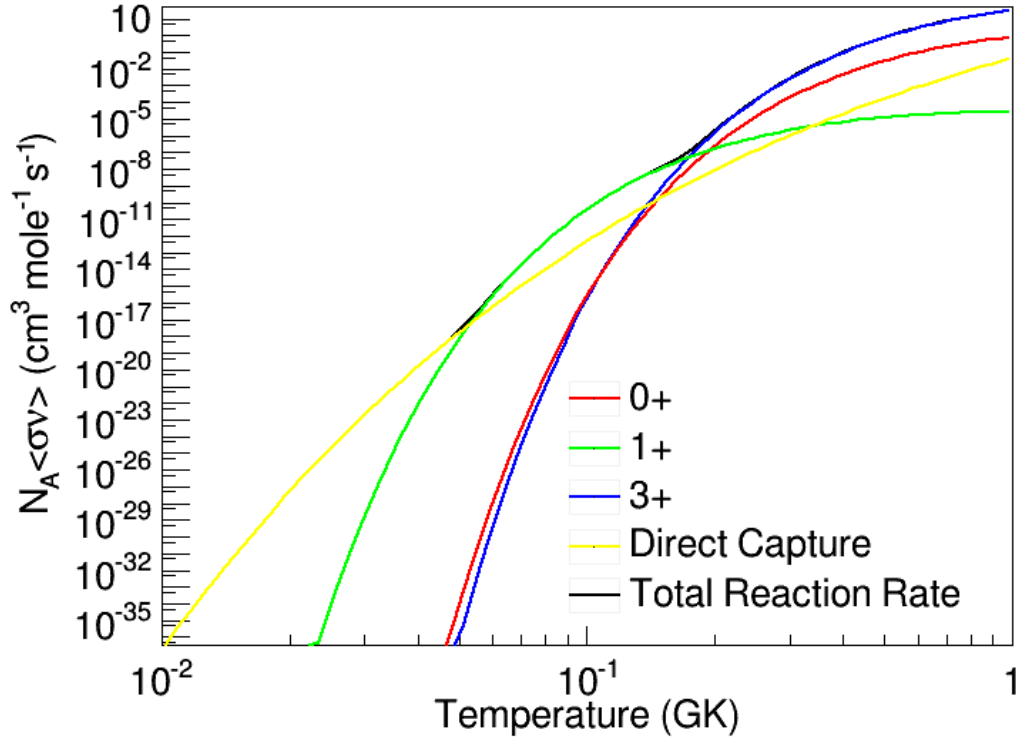


Figure 3.23: The contribution to the total reaction rate from the individual resonances in the Gamow Window.

threshold. For the 1_1^+ and the 0_4^+ resonances, the excitation energies are taken from this work. For the 3_3^+ , the excitation energy is taken from Bennett et al. [12].

For the γ -ray and proton partial widths, there is little experimental data. For the 1_1^+ state and the 0_4^+ state, the partial widths are determined through a combination of comparisons with the mirror nuclei, ^{26}Mg , and shell model calculations. In this work, we adopt the partial widths reported by Wrede[52] for these two states. The only difference here is that Γ_γ depends on the energy of the γ ray to the 5th power, so we scale the γ -ray partial width by its new resonance energy. The partial widths for the 3_3^+ have been measured experimentally. These partial widths are taken from Bennett et al[12]. The proton partial width was measured by Peplowski et al.[44]. Bennett et al.[12] was able to measure the intensity of a γ ray de-exciting this level from the β -decay of ^{26}P . They used the proton intensity measured from this same reaction by Thomas et al.[53] to determine the ratio of partial widths. Finally, they used the proton partial width measured by

Peplowski et al.[44] to determine the γ -ray partial width.

The contribution of these resonances to the total reaction rate is shown in Figure 3.23. The 1^+ resonance dominates the reaction at temperatures between 0.05GK and 0.18 GK and the 3^+ resonance dominates at larger temperatures. The non-resonant, direct capture, reaction rate dominates at the lowest temperatures. The 0^+ resonance never contributes more than about 10% to the total rate.

3.5.2 Impact of Uncertainties on $^{25}\text{Al}(p,\gamma)$ Reaction Rate

The previous calculation assumed that the 0_4^+ resonance exists at 5.90 MeV as seen in this work. The spin and parity for this state was measured by a recent Gammasphere experiment and definitively identified this as a 0^+ state[2]. However, a state at 5.95 MeV has been observed by multiple experiments [48][49] and has also been identified as a possible 0^+ state. The impact of moving the 0_4^+ state from 5.95 MeV to 5.89 MeV is large. Figure 3.24 shows the contribution of the 0_4^+ to the total reaction rate assuming it is located at either energy and with the γ width scaled accordingly. Assuming the resonance is at 5.95 MeV, the resonance never contributes more than 1% to the reaction rate. Moving the resonance to 5.89 MeV, the resonance now contributes as much as 10% at nova temperatures. This calculation is in agreement with one recently done by Chipps[54].

The 3_3^+ resonance contributes the most to the reaction rate at nova temperatures. This state now has experimental constraints on all of the variables that enter into 3.13. The largest uncertainty in this resonance comes from the parameter Γ_γ . Bennett et al.[12] reported $\Gamma_\gamma = 40 \pm 11(\text{stat})_{-18}^{+19}(\text{lit})$. Figure 3.25 shows the total calculated reaction rate for three different values of Γ_γ . The uncertainty at peak nova temperatures of 0.3 GK is now about a factor of 3.

3.5.3 Impact on Stellar Abundance of ^{26}Al

To fully assess the impact of this reaction rate on the stellar abundance of ^{26}Al , a detailed nova model would have to be performed. However, we can estimate how much of an impact this reaction has on the abundance by comparing the half-life of proton capture to the half-life of β -decay of ^{25}Al . In order for the $^{25}\text{Al}(p,\gamma)$ reaction to bypass the β -decay, the half-life for the capture must be on the same order as the β -decay half life, which is 7.2s. The half life of proton capture can be

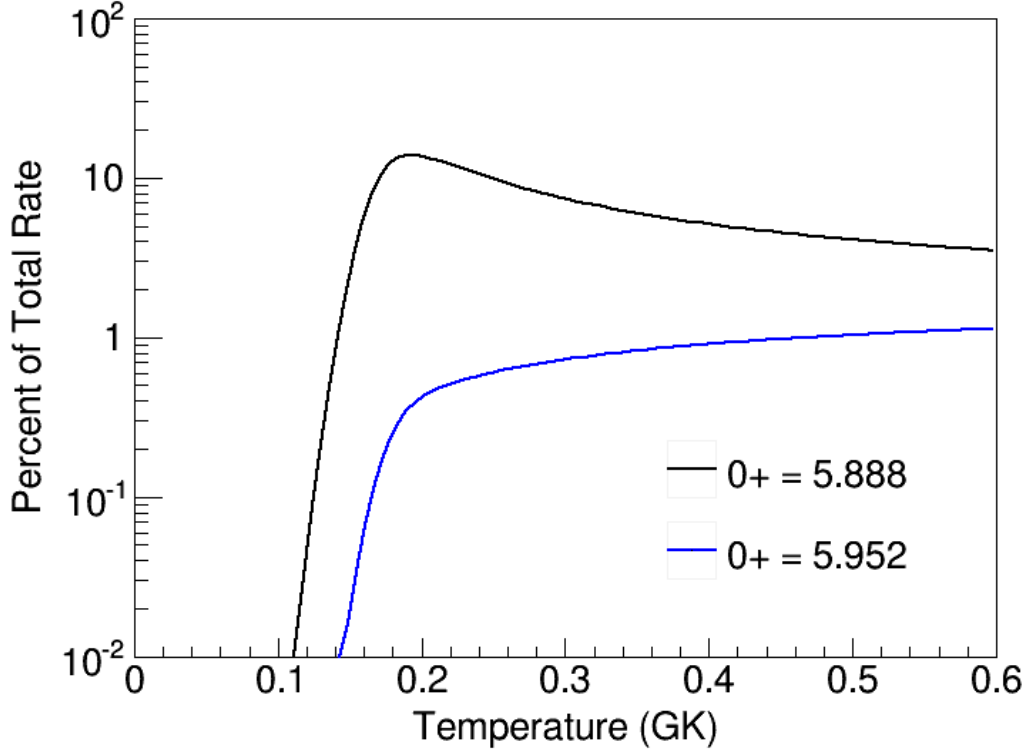


Figure 3.24: The percent that the 0^+ rate contributes to the total reaction rate. Using the newer value of 5.888 MeV increases the contribution of the 0^+ state at nova temperatures.

calculated from the reaction rate using equation 3.15 [50]. The density, ρ , and mass fraction, X_H , have to be assumed. In the following calculation, $\rho = 10^3 \text{ g/cm}^3$ and $X_H = 0.4$.

$$\tau = \left(\rho \frac{X_H}{M_H} N_A \langle \sigma \nu \rangle \right)^{-1} \quad (3.15)$$

The half-life for proton capture competes with the β decay half life at $T = 0.3 \text{ GK}$. At 0.3 GK the reaction rate is calculated to be $0.0025 \text{ cm}^3 \text{ mol}^{-1} \text{ s}^{-1}$. With the parameters above, this gives a half-life of 0.7s, much faster than the β decay half-life. With the uncertainties due to the partial width shown in Figure 3.25, the half-life for proton capture could vary between 0.5s and 1.25s. At 0.2 GK , on the other hand, the half-life for proton capture is on the order of 1000 s.

Nuclear physics uncertainties still exist in this reaction rate. Particularly, if a 4^{th} resonance exists in the Gamow window, it could change the current estimates for the reaction rate. Addi-

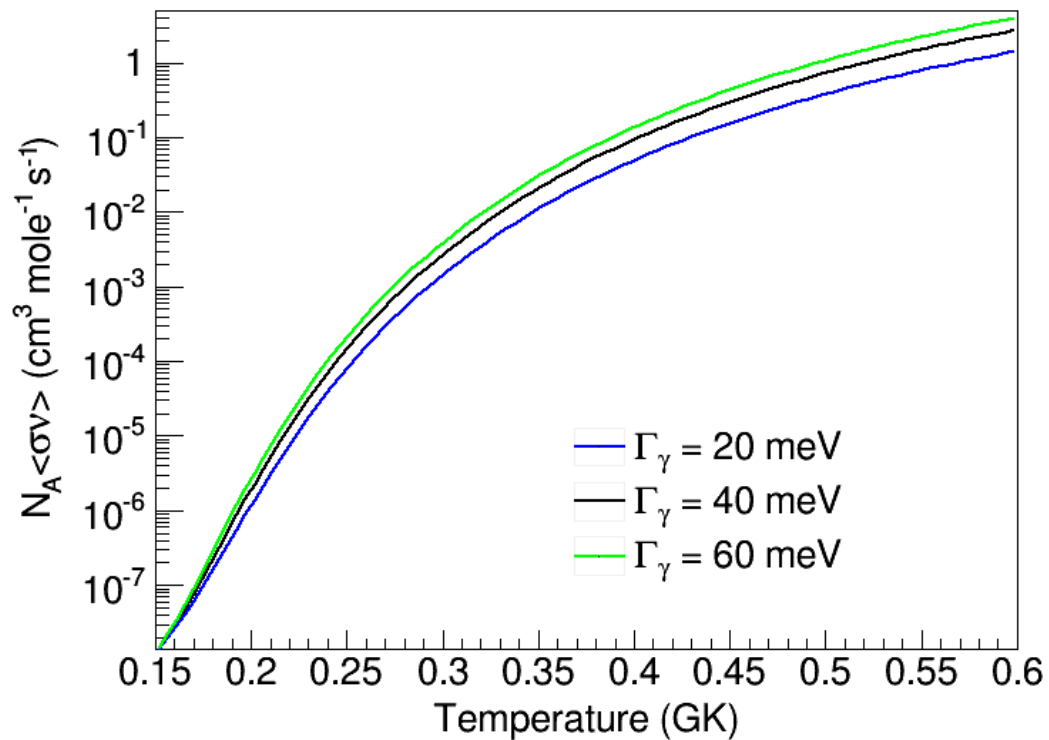


Figure 3.25: Impact of uncertainty in Γ_γ of the 3^+ state on the total reaction rate. The uncertainties in Γ_γ are taken from the recent publication by Bennett et al[12].

tionally, the γ -decay branch of the 3^+ resonance has been observed once, so a second observation of this branch is needed to confirm the measurement.

APPENDIX A

TOF CORRECTION FOR THE S800 SPECTROMETER

The S800 Spectrometer was described in the text. Here, we will discuss an additional calibration procedure that was used to clean up the particle identification. As discussed previously, the ^{44}S was identified by correlating the energy loss of a particle in the ion chamber with the time of flight (tof) of the particle with respect to the rf of the cyclotron. The energy loss separates the particles based on charge and the tof separates particles according to their mass. The tof measurement had some difficulties which will be discussed here.

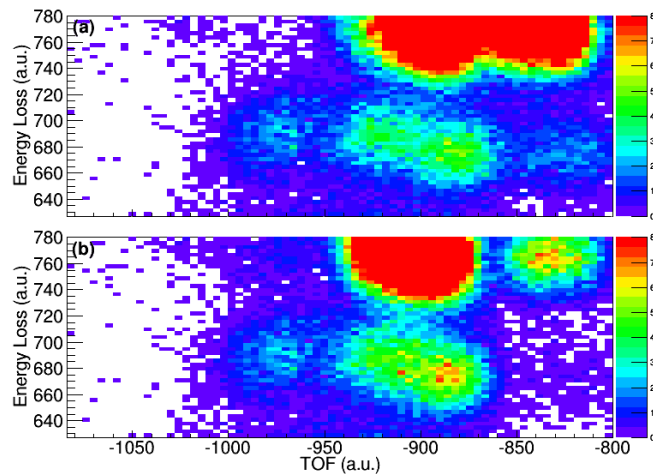


Figure A.1: The particle identification shown before (Panel a) and after (Panel b) a timing correction was done.

Figure A.1 shows the PID zoomed in on the Sulfur isotopes. In Panel a, one can see a blob to the right of the Sulfur isotopes that should not exist. By gating on this blob, one can see that these residues are largely ^{42}S . In fact, there is a second, slightly shifted PID that places some of the ^{44}S with the ^{43}S and some of the ^{43}S with the ^{42}S . This shift is caused by a problem with one of the scintillators at the back of the focal plane.

Normally, there are three scintillators that give timing information with a photomultiplier tube at either end. Ideally, the average time of one of these scintillators would be used as a reference for the tof. However, in this experiment, only one output of one of the scintillators was working. Panel a of Figure A.2 shows the time measured by this scintillator plotted against the energy measured by the scintillator. One would expect to see the time vary smoothly with the energy, but there is a clear discontinuity. It is this discontinuity that leads to the PID shift in Figure A.1. To fix the shift, a piecewise function was fit to the discontinuous part of the spectra and the data was forced to follow a roughly continuous line as shown in Panel b of Figure A.2. The PID using this corrected tof is shown in Panel b of Figure A.1. As can be seen, most of the shifted blob has been moved to the proper location. By looking only at the PID with the bad timing signal, we determined that about 15% of the ^{44}S in this experiment was shifted due to this incorrect timing signal.

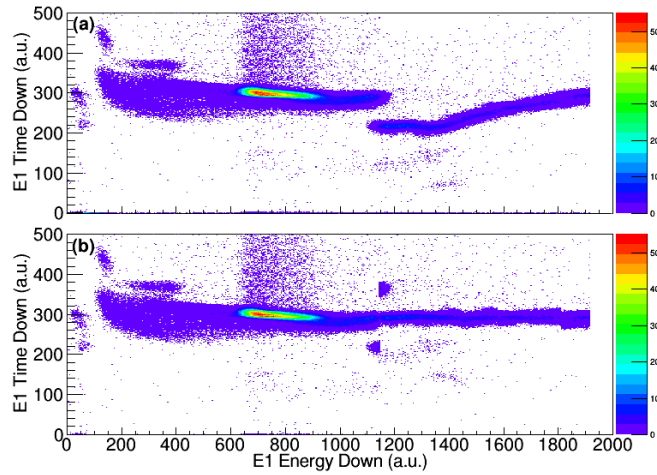


Figure A.2: The timing of the plastic scintillator as a function of its energy before (Panel a) and after (Panel b) the timing was corrected for.

BIBLIOGRAPHY

- [1] D. Seweryniak, P. Woods, M. Carpenter, T. Davinson, R. Janssens, D. Jenkins, T. Lauritsen, C. Lister, J. Shergur, S. Sinha, and A. Woehr, “Level structure of ^{26}Si and its implications for the astrophysical reaction rate of $^{25}\text{Al}(p,\gamma)^{26}\text{Si}$,” *Phys. Rev. C*, vol. 75, p. 062801(R), 2007.
- [2] D. Doherty, P. Woods, D. Seweryniak, M. Albers, A. Ayangeakaa, M. Carpenter, C. Chiara, H. David, J. Harker, R. Janssens, A. Kankainen, C. Lederer, and S. Zhu, “Structure of resonances in the gamow burning window for the $^{25}\text{Al}(p,\gamma)^{26}\text{Si}$ reaction in novae,” *Phys. Rev. C*, vol. 92, p. 035808, 2015.
- [3] O. Sorlin and M. Porquet, “Evolution of the $N = 28$ shell closure: a test bench for nuclear forces,” *Phys.Scr.*, vol. T152, p. 014003, 2013.
- [4] D. Santiago-Gonzalez, I. Wiedenhover, V. Abramkina, M. L. Avila, T. Baugher, D. Bazin, B. A. Brown, P. D. Cottle, A. Gade, T. Glasmacher, K. W. Kemper, S. McDaniel, A. Rojas, A. Ratkiewicz, R. Meharchand, E. C. Simpson, J. A. Tostevin, A. Volya, and D. Weisshaar, “Triple configuration coexistence in ^{44}S ,” *Phys.Rev. C*, vol. 83, p. 061305, 2011.
- [5] J. Yurkon, D. Bazin, W. Benenson, D. Morrissey, B. Sherrill, D. Swan, and R. Swanson, “Focal plane detector for the S800 high-resolution spectrometer,” *Nucl. Instrum. Methods Phys. Res. Sect. A*, vol. 422, p. 291, 1999.
- [6] G. F. Knoll, *Radiation Detection and Measurement*. New York: John Wiley & Sons, Inc., 3 ed., 2000.
- [7] P. Adrich, D. Enderich, D. Miller, V. Moeller, R. Norris, K. Starosta, C. Vaman, P. Voss, and A. Dewald, “A simulation tool for recoil distance method lifetime measurements at NSCL,” *Nuclear Instruments and Methods in Physics Research Section A: Accelerators, Spectrometers, Detectors and Associated Equipment*, vol. 598, no. 2, pp. 454 – 464, 2009.
- [8] D. Sangiango-Gonzalez, *Experimental Investigations on the Nuclear Structure of the neutron-rich nuclides ^{44}S and ^{20}O* . PhD thesis, Florida State University, 2012.
- [9] A. Bohr and B. Mottelson, *Nuclear Structure*, vol. 2. Singapore: World Scientific Publishing, 1998.
- [10] R. Diehl, H. Halloin, K. Kretschmer, G. Lichti, V. Schonfelder, A. Strong, A. von Kienlin, W. Wang, P. Jean, J. Knodlseder, J. P. Roques, G. Weidenspointner, S. Schanne, D. Hartmann, C. Winkler, and C. Wunderer, “Radioactive ^{26}Al and massive stars in the Galaxy,” *Nature (London)*, vol. 439, p. 45, 2006.

- [11] J. Jose, M. Hernanz, and A. Coc, “New results on ^{26}Al production in classical novae,” *Astrophysics J. Lett.*, vol. 479, p. L55, 1997.
- [12] M. Bennett, C. Wrede, K. Chipps, J. Jose, S. Liddick, M. Santia, A. Bowe, A. Chen, N. Cooper, D. Irvine, E. McNeice, F. Montes, F. Naqvi, R. Ortez, S. Pain, J. Pereira, C. Prokop, J. Quaglia, S. Quinn, S. Schwartz, S. Shanab, A. Simon, A. Spyrou, and E. Thiagalingam, “Classical-nova contribution to the Milky Way’s ^{26}Al abundance: Exit channel of the key $^{25}\text{Al}(p,\gamma)^{26}\text{Si}$ resonance,” *Phys. Rev. Lett.*, vol. 111, p. 232503, 2013.
- [13] M. Goeppert-Mayer, “On closed shells in nuclei.ii,” *Phys.Rev.*, vol. 75, p. 1969, 1949.
- [14] O. Haxel, J. H. D. Jensen, and H. E. Suess, “On the magic numbers in nuclear structure,” *Phys.Rev.*, vol. 75, p. 1766, 1949.
- [15] D. Geesaman, V. Cirigilano, A. Deshpande, F. Fahey, J. Hardy, K. Heeger, D. Hobart, S. Lapi, J. Nagle, F. Nunes, E. Ormand, J. Piekarewicz, P. Rossi, J. Schukraft, K. Scholberg, M. Shepherd, R. Venugopalan, M. Wiescher, and J. Wilkerson, “Reaching for the horizon: The 2015 long range plan for nuclear science,” 2015.
- [16] J. Parker IV, I. Wiedenhover, P. Cottle, J. Baker, D. McPherson, M. Riley, D. Santiago-Gonzalez, A. Volya, V. Bader, T. Baugher, D. Bazin, A. Gade, T. Ginter, H. Iwasaki, C. Loelius, C. Morse, F. Recchia, D. Smalley, S. Stroberg, K. Whitmore, D. Weisshaar, A. Lemasson, H. Crawford, A. Macchiavelli, and K. Wimmer, “Isomeric character of the lowest observed 4^+ state in ^{44}S ,” *Phys.Rev. Lett.*, vol. 118, p. 052501, 2017.
- [17] F. Hoyle, D. Dunbar, W. Wenzel, and W. Whaling, “A state in ^{12}C predicted from astrophysical evidence,” *Phys. Rev.*, vol. 92, p. 1095, 1953.
- [18] T. Glasmacher, B. A. Brown, M. J. Chromik, P. D. Cottle, M. Fauerbach, R. W. Ibbotson, K. W. Kemper, D. J. Morrissey, H. Scheit, D. W. Sklenicka, and M. Steiner, “Collectivity in ^{44}S ,” *Phys.Lett.*, vol. 395B, p. 163, 1997.
- [19] S. Grevy, F. Negoita, I. Stefan, N. L. Achouri, J. C. Angelique, B. Bastin, R. Borcea, A. Buta, J. M. Daugas, F. De Oliveira, O. Giarmana, C. Jollet, B. Laurent, M. Lazar, E. Lienard, F. Marechal, J. Mrazek, D. Pantelica, Y. Penionzhkevich, S. Pietri, O. Sorlin, M. Stanoiu, C. Stodel, and M. G. St-Laurent, “Observation of the 0_2^+ state in ^{44}S ,” *Eur.Phys.J. A*, vol. 25, pp. Supplement 1, 111, 2005.
- [20] C. Force, S. Grevy, L. Gaudefroy, O. Sorlin, L. Caceres, F. Rotaru, J. Mrazek, N. L. Achouri, J. C. Angelique, F. Azaiez, B. Bastin, R. Borcea, A. Buta, J. M. Daugas, Z. Dlouhy, Z. Dombradi, F. De Oliveira, F. Negoita, Y. Penionzhkevich, M. G. Saint-Laurent, D. Sohler, M. Stanoiu, I. Stefan, C. Stodel, and F. Nowacki, “Prolate-spherical shape coexistence at $N=28$ in ^{44}S ,” *Phys.Rev.Lett.*, vol. 105, p. 102501, 2010.

- [21] D. Bazin, J. Caggiano, B. Sherrill, J. Yurkon, and A. Zeller, “The S800 Spectrograph,” *Nucl. Instrum. Methods Phys. Res. B*, vol. 204, p. 629, 2003.
- [22] G. Schmid, M. Deleplanque, I. Lee, F. Stephens, K. Vetter, R. Clark, R. Diamond, P. Fallon, A. Macchiavelli, and R. MacLeod, “A γ ray tracking algorithm for the GRETA spectrometer,” *Nucl. Instrum. Methods Phys. Res. A*, vol. 430, p. 69, 1999.
- [23] D. Weisshaar, D. Bazin, P. Bender, C. Campbell, F. Recchia, V. Bader, T. Baugher, J. Belarge, M. Carpenter, H. Crawford, M. Cromaz, B. Elman, P. Fallon, A. Forney, A. Gade, J. Harker, N. Kobayashi, C. Langer, T. Lauritsen, I. Lee, A. Lemasson, B. Longfellow, E. Lunderberg, A. Macchiavelli, K. Miki, S. Momiyama, S. Noji, D. Radford, M. Scott, J. Sethi, S. Stroberg, C. Sullivan, R. Titus, A. Wiens, S. Williams, K. Wimmer, and S. Zhu, “The performance of the γ -ray tracking array GREINA for γ -ray spectroscopy with fast beams of rare isotopes,” *Nucl. Instrum. Methods Phys. Res. A*, vol. 847, p. 187, 2016.
- [24] H. Iwasaki, A. Dewald, T. Braunroth, C. Fransen, D. Smalley, A. Lemasson, C. Morse, K. Whitmore, and C. Loelius, “The TRIPLE PLunger for EXotic beams TRIPLEX for excited-state lifetime measurement studies on rare isotopes,” *Nuclear Instruments and Methods in Physics Research Section A: Accelerators, Spectrometers, Detectors and Associated Equipment*, vol. 806, pp. 123 – 131, 2016.
- [25] L. A. Riley, P. Adrich, N. Ahsan, T. R. Baugher, D. Bazin, B. A. Brown, J. M. Cook, P. D. Cottle, C. A. Diget, A. Gade, T. Glasmacher, K. E. Hosier, K. W. Kemper, A. Ratkiewicz, K. P. Siwek, J. A. Tostevin, A. Volya, and D. Weisshaar, “ γ -ray spectroscopy of one-proton knockout from ^{45}Cl ,” *Phys.Rev. C*, vol. 86, p. 047301, 2012.
- [26] L. Caceres, D. Sohler, S. Grevy, O. Sorlin, Z. Dombradi, B. Bastin, N. L. Achouri, J. C. Angelique, F. Azaiez, D. Baiborodin, R. Borcea, C. Bourgeois, A. Buta, A. Burger, R. Chapman, J. C. Dalouzy, Z. Dlouhy, A. Drouard, Z. Elekes, S. Franchoo, L. Gaudefroy, S. Iacob, B. Laurent, M. Lazar, X. Liang, E. Lienard, J. Mrazek, L. Nalpas, F. Negoita, F. Nowacki, N. A. Orr, Y. Penionzhkevich, Z. Podolyak, F. Pougheon, A. Poves, P. Roussel-Chomaz, M. G. Saint-Laurent, M. Stanoiu, and I. Stefan, “In-beam spectroscopic studies of the ^{44}S nucleus,” *Phys.Rev. C*, vol. 85, p. 024311, 2012.
- [27] P. R. Bevington and D. K. Robinson, *Data Reduction and Error Analysis for the Physical Sciences*. New York: McGraw Hill, 3 ed., 2003.
- [28] P. Ring and P. Schuck, *The Nuclear Many-Body Problem*. Berlin: Springer-Verlag, 1 ed., 2004.
- [29] H. Scheit, T. Glasmacher, B. A. Brown, J. A. Brown, P. D. Cottle, P. G. Hansen, R. Harkewicz, M. Hellstrom, R. W. Ibbotson, J. K. Jewell, K. W. Kemper, D. J. Morrissey, M. Steiner, P. Thierolf, and M. Thoennessen, “New region of deformation: The neutron-rich sulfur isotopes,” *Phys.Rev.Lett.*, vol. 77, p. 3967, 1996.

- [30] F. Nowacki and A. Poves, “New effective interaction for $0\hbar\omega$ shell-model calculations in the sd-pf valence space,” *Phys.Rev. C*, vol. 79, p. 014310, 2009.
- [31] Y. Utsuno, T. Otsuka, B. A. Brown, M. Honma, T. Mizusaki, and N. Shimizu, “Shape transitions in exotic Si and S isotopes and tensor-force-driven jahn-teller effect,” *Phys.Rev. C*, vol. 86, p. 051301(R), 2012.
- [32] R. F. Casten, *Nuclear Structure from a Simple Perspective*. New York: Oxford University Press, 2 ed., 2005.
- [33] Y. Utsuno, N. Shimizu, T. Otsuka, T. Yoshida, and Y. Tsunoda, “Nature of isomerism in exotic sulfur isotopes,” *Phys.Rev.Lett.*, vol. 114, p. 032501, 2015.
- [34] J. L. Egido, M. Borrajo, and T. Rodriguez, “Collective and single-particle motion in beyond mean field approaches,” *Phys.Rev. Lett.*, vol. 116, p. 052502, 2016.
- [35] R. Chevrier and L. Gaudefroy, “Shell model structure of ^{43}S and ^{44}S re-examined,” *Phys.Rev. C*, vol. 89, p. 051301, 2014.
- [36] T. R. Rodriguez and J. L. Egido, “Configuration mixing description of the nucleus ^{44}S ,” *Phys.Rev. C*, vol. 84, p. 051307, 2011.
- [37] W. Mahoney, J. Ling, W. Wheaton, and A. Jacobson, “HEAO 3 discovery of ^{26}Al in the interstellar medium,” *The Astrophysical Journal*, vol. 286, p. 578, 1984.
- [38] R. Diehl, C. Dupraz, K. Bennett, H. Bloemen, W. Hermsen, J. Knodlseder, G. Lichti, D. Morris, J. Ryan, V. Schonfelder, H. Steinle, A. Strong, B. Swanenburg, M. Varendorff, and C. Winkler, “COMPTEL observations of Galactic ^{26}Al emission,” *Astron. Astrophys.*, vol. 298, p. 445, 1995.
- [39] C. Iliadis, L. Buchmann, P. Endt, H. Herndl, and M. Wiescher, “New stellar reaction rates for $^{25}\text{Mg}(p,\gamma)^{26}\text{Al}$ and $^{25}\text{Al}(p,\gamma)^{26}\text{Si}$,” *Phys. Rev. C.*, vol. 53, p. 475, 1996.
- [40] J. Caggiano, W. Bradfield-Smith, R. Lewis, P. Parker, D. Visser, J. Greene, K. Rehm, D. Bardayan, and A. Champagne, “Identification of new states in ^{26}Si using the $^{29}\text{Si}(^3\text{He}, ^6\text{He})^{26}\text{Si}$ reaction and consequences for the $^{25}\text{Al}(p,\gamma)^{26}\text{Si}$ reaction rate in explosive hydrogen burning environments,” *Phys. Rev. C*, vol. 65, p. 055801, 2002.
- [41] N. de Sereville, M. Assie, I. Bahrini, D. Beaumel, M. Chabot, M. Ferraton, S. Fortier, S. Franchoo, S. Giron, F. Hammache, M. Lebois, F. Marechal, A. Matta, B. Mouginot, C. Petrache, P. Roussel, J. Scarpacci, I. Stefan, D. Verney, A. Coc, I. Deloncle, J. Duprat, C. Hammadache, J. Kiener, A. Lefebvre-Schuhl, F. de Oliveira, F. de Grancey, J. Thomas, M. Fallot, L. Giot, L. Lamia, R. Pizzonne, and S. Romano, “Spectroscopic study of ^{26}Si for application to nova gamma-ray emission,” *PoS*, vol. NIC XI, p. 212, 2011.

- [42] T. Komatsubara, S. Kubono, T. Hayakawa, T. Shizuma, A. Ozawa, Y. Ito, Y. Ishibashi, T. Moriguchi, H. Yamaguchi, D. Kahl, S. Hayakawa, D. N. Binh, A. Chen, J. Chen, K. Setoodehnia, and T. Kajino, “Excited states above the proton threshold in ^{26}Si ,” *The European Physical Journal A*, vol. 50, p. 136, 2014.
- [43] D. Bardayan, J. Howard, J. Blackmon, C. Brune, K. Chae, W. Hix, M. Johnson, K. Jones, R. Kozub, J. Liang, E. Lingerfelt, R. Livesay, S. Pain, J. Scott, and M. Smith, “Astrophysically important ^{26}Si states studied with the $^{28}\text{Si}(p,t)^{26}\text{Si}$ reaction. ii. spin of the 5.914-mev ^{26}Si level and galactic ^{26}Al production,” *Phys. Rev. C*, vol. 74, p. 045804, 2012.
- [44] P. Peplowski, L. Baby, I. Wiedenhover, S. Dekat, E. Diffenderfer, D. Gay, O. Grubor-Urošević, P. Hofflich, R. Kaye, N. Keeley, A. Rojas, and A. Volya, “Lowest $l=0$ proton resonance in ^{26}Si and implications for nucleosynthesis of ^{26}Al ,” *Phys. Rev. C*, vol. 79, p. 032801(R), 2009.
- [45] W. Bohne, K. Buchs, H. Fuchs, K. Grabisch, D. Hilscher, U. Jahnki, H. Kluge, T. Masterson, and H. Morgenstern, “Study of the reactions $^{24,26}\text{Mg}(^3\text{He},n)^{26,28}\text{Si}$ and $^{28}\text{Si}(^3\text{He},n)^{30}\text{S}$,” *Nuclear Physics A*, vol. 378, p. 525, 1982.
- [46] D. Bardayan, J. Blackmon, A. Champagne, A. Dummer, T. Davinson, U. Greife, D. Hill, C. Iliadis, B. Johnson, R. Kozub, C. Lee, M. Smith, and P. Woods, “Astrophysically important ^{26}Si states studied with the $^{28}\text{Si}(p,t)^{26}\text{Si}$ reaction,” *Phys. Rev. C*, vol. 65, p. 032801, 2002.
- [47] R. Paddock, “(p,t) reaction on even-even $n=z$ nuclei in the $2s1d$ shell,” *Phys. Rev. C*, vol. 5, no. 2, p. 485, 1972.
- [48] Y. Parpottas, S. Grimes, S. Al-Quraishi, C. Brune, T. Massey, J. Oldendick, A. Salas, and R. Wheeler, “Astrophysically important ^{26}Si states studied with the $(^3\text{He},n)$ reaction and the $^{25}\text{Al}(p,\gamma)^{26}\text{Si}$ reaction rates in explosive hydrogen burning environments,” *Phys. Rev. C*, vol. 70, p. 065805, 2004.
- [49] A. Matic, A. van den Berg, M. Harakeh, H. Wortche, G. Berg, M. Couder, J. Gorres, P. LeBlanc, S. O’Brien, M. Wiescher, K. Fujita, K. Hatanaka, Y. Sakemi, Y. Shimizu, Y. Tameshige, A. Tamii, M. Yosoi, T. Adachi, Y. Fujita, Y. Shimbara, H. Fujita, T. Wakasa, B. Brown, and H. Schatz, “High-precision (p,t) reaction to determine $^{25}\text{Al}(p,\gamma)^{26}\text{Si}$ reaction rates,” *Phys. Rev. C*, vol. 82, p. 025807, 2010.
- [50] C. Iliadis, *Nuclear Physics of Stars*. Weinheim: Wiley-VCH, 2007.
- [51] M. Wang, G. Audi, A. Wapstra, F. Kondev, M. MacCormick, X. Xu, and B. Pfeiffer, “The AME2012 atomic mass evaluation,” *Chinese Physics C*, vol. 36, no. 12, p. 1603, 2012.
- [52] C. Wrede, “Thermonuclear $^{25}\text{Al}(p,\gamma)^{26}\text{Si}$ reaction rate in classical novae and galactic ^{26}Al ,” *Phys. Rev. C*, vol. 79, p. 035803, 2009.

- [53] J. Thomas, L. Achouri, J. Aysto, R. Beraud, B. Blank, G. Canchel, S. Czajkowski, P. Dendoover, A. Ensalle, J. Giovanazzo, N. Guillet, J. Honkanen, A. Jokinen, A. Laird, M. Lewitowicz, C. Longour, F. Oliveira Santos, K. Perajarvi, and M. Stanoiu, “Beta-decay properties of ^{25}Si and ^{26}P ,” *The European Physical Journal A*, vol. 21, p. 419, 2004.
- [54] K. Chipps, “Resonances above the proton threshold in ^{26}Si ,” *Phys. Rev. C*, vol. 93, p. 035801, 2016.

BIOGRAPHICAL SKETCH

John Johnston Parker IV was born on July 4, 1989 in Birmingham, Al where he spent his first 18 years. He received a Bachelor of Science degree in physics from the University of North Carolina at Chapel Hill in 2011. Immediately after, he enrolled in the physics graduate program at Florida State University, where he received his masters in 2012 and his PhD in 2017 under the supervision of Dr. Ingo Wiedenhöver.